

AD-A262 783

PI-TR-92-2248 (I)



2

2

**ANALYSIS OF DYNAMICAL PLASMA
INTERACTIONS WITH HIGH-VOLTAGE
SPACECRAFT**

M. J. Mandell
T. Luu
J. Lilley
G. Jongeward
I. Katz

Maxwell Laboratories, Inc.
S-Cubed Division
P. O. Box 1620
La Jolla, California 92038-1620



June 1992

Final Report - Volume I
31 December 1988 through 31 December 1991

Approved for public release; distribution unlimited



**PHILLIPS LABORATORY
AIR FORCE MATERIEL COMMAND
HANSCOM AIR FORCE BASE, MA 01731-5000**

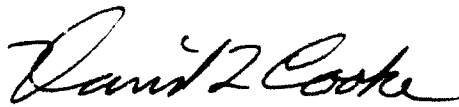
93-04956



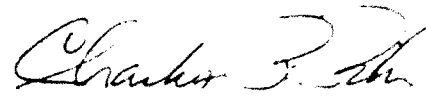
18307

88 2 0 070

" This technical report has been reviewed and is approved for publication "



DAVID L. COOKE
Contract Manager



CHARLES P. PIKE
Branch Chief

This report has been reviewed by the ESD Public Affairs Office (PA) and is releasable to the National Technical Information Service (NTIS).

Qualified requestors may obtain additional copies from the Defense Technical Information Center. All others should apply to the National Technical Information Service.

If your address has changed, or if you wish to be removed from the mailing list, or if the addressee is no longer employed by your organization, please notify PL/TSI, Hanscom AFB, MA 01731-5000. This will assist us in maintaining a current mailing list.

Do not return copies of this report unless contractual obligations or notices on a specific document requires that it be returned.

REPORT DOCUMENTATION PAGE			Form Approved OMB No. 0704-0188	
<small>Public reporting burden for this collection of information is estimated to average 1 hour per response, including the time for reviewing instructions, searching existing data sources, gathering and maintaining the data needed, and completing and reviewing the collection of information. Send comments regarding this burden estimate or any other aspect of this collection of information, including suggestions for reducing this burden, to Washington Headquarters Service, Directorate for Information Operations and Reports, 1215 Jefferson Davis Highway, Suite 1204, Arlington, VA 22202-4302, and to the Office of Management and Budget, Paperwork Project (0704-0188), Washington, DC 20503.</small>				
1. AGENCY USE ONLY (Leave blank)		2. REPORT DATE June 1992	3. REPORT TYPE AND DATES COVERED Final (31 Dec 1988 - 31 Dec 1991)	
4. TITLE AND SUBTITLE Analysis of Dynamical Plasma Interactions With High Voltage Spacecraft			5. FUNDING NUMBERS PE 62101F PR 7601 TA 30 WU AE Contract F19628-89 C 0032	
6. AUTHOR(S) M. J. Mandell J Lilley T. Liu G Jongeward I. Katz				
7. PERFORMING ORGANIZATION NAME(S) AND ADDRESS(ES) Maxwell Laboratories, Inc. S-Cubed Division P. O. Box 1620 La Jolla, CA 92038-1620			8. PERFORMING ORGANIZATION REPORT NUMBER	
9. SPONSORING/MONITORING AGENCY NAME(S) AND ADDRESS(ES) Phillips Laboratory Hanscom Air Force Base, MA 01731-5000 Contract Manager: David Cooke/WSSI			10. SPONSORING/MONITORING AGENCY REPORT NUMBER PL TR-92-2248 (1)	
11. SUPPLEMENTARY NOTES				
12a. DISTRIBUTION/AVAILABILITY STATEMENT Approved for public release; distribution unlimited			12b. DISTRIBUTION CODE	
13. ABSTRACT (Maximum 200 words) <p>This volume describes numerous plasma interaction problems done in support of DynaPAC code development, and in support of the SPEAR-II and SPEAR-3 programs. Two dimensional calculations show that oscillations of a beam emitted into an underdense plasma can cause overcharging of a beam emitting rocket, as was observed on MAIMIK. The effects of the sheath instability caused by orbital motion of a positive body are studied, showing that substantial potential oscillations occur, and that the electron current to the probe is enhanced.</p> <p>The plasma response to a sudden application of negative voltage to a probe is studied. It takes a long time to establish an equilibrium sheath, and early time ion currents can be enhanced by an order of magnitude. We calculate currents to the SPEAR-II high voltage probe, explaining the observed difference in probe reading between vacuum and plasma conditions.</p> <p>A one dimensional model estimates the neutral density required for breakdown of a negative sheath, as proposed for SPEAR-3. We show calculations of the SPEAR-3 rocket floating potentials, collected currents, and current distribution to the particle detectors. Finally, DynaPAC calculations for the sheath structure around the TSS-1 subsatellite are presented.</p>				
14. SUBJECT TERMS Spacecraft Plasma Interactions Space Power			15. NUMBER OF PAGES 184 16. PRICE CODE	
17. SECURITY CLASSIFICATION OF REPORT Unclassified		18. SECURITY CLASSIFICATION OF THIS PAGE Unclassified		19. SECURITY CLASSIFICATION OF ABSTRACT Unclassified
			20. LIMITATION OF ABSTRACT SAR	

TABLE OF CONTENTS

<u>Section</u>	<u>Page</u>
Preface	v
1. Introduction	1
2. Dynamics of Spacecraft Charging by Electron Beams	4
3. Positive Orbital Probe Calculation	26
4. Transient Sheath Dynamics	37
5. Application to SPEAR-II	48
6. Calculation of Currents to SPEAR-II	54
7. SPEAR-II Products Report	64
8. Simple Calculations for the Breakdown of a Negative Sheath	121
9. SPEAR-3 Sheath Structure and Plasma Currents	126
10. SPEAR-3 Calculations for Particle Detector Placement.....	142
11. Three Dimensional Magnetic Sheath Calculations.....	171

Accession For	
NTIS GRA&I	<input checked="" type="checkbox"/>
DTIC TAB	<input type="checkbox"/>
Unannounced	<input type="checkbox"/>
Justification	
By _____	
Distribution/	
Availability Codes	
Dist	Avail and/or Special
A-1	

PREFACE

This is Volume 1 of a two volume final report for the contract "Analysis of Dynamical Plasma Interactions with High Voltage Spacecraft." The period of technical performance was 31 December 1988 through 31 December 1991. The objectives of this contract were to study dynamical plasma interactions with high voltage spacecraft, to construct a three-dimensional computer code, DynaPAC, as a workbench for such studies, and to support the SPEAR program. Volume 1 is a compilation of work done to model high voltage plasma interactions, with application to the SPEAR-II chamber tests and to the design of SPEAR-3. Volume 2 contains documentation for the DynaPAC code, as well as for the two-dimensional Gilbert code.

1. INTRODUCTION

This volume contains excerpts of work done in three general areas:

- (1) Dynamic plasma problems done in two dimensions using the Gilbert code. (Chapters 2-3.)
- (2) Work performed in support of the SPEAR-II program. (Chapters 4-7.)
- (3) Work performed in support of the SPEAR-3 program. (Chapters 8-10.)
The SPEAR-3 work is continuing under contract F19628-91-C-0187,
entitled "Space System-Environment Interactions Investigation."

In addition to numerous technical meetings directly related to this contract or to the SPEAR program, presentations were made under this contract at the following professional conferences:

Spacecraft Charging Technology Conference, Monterey, CA, 30 October through 2 November, 1989. "Dynamics of Spacecraft Charging by Electron Beams." M. J. Mandell and I. Katz. (Conference proceedings available.)

High Voltage Workshop, Port Hueneme, CA, 19-21 March, 1991. "Transient Plasma Current to a High Voltage Probe." M. J. Mandell, T. T. Luu, G. A. Jongeward and I. Katz.

Physics Computing '91, 10-14 June, San Jose, CA. "DynaPAC - A 3-D Finite Element Plasma Analysis Code." M. J. Mandell, T. T. Luu, and J. R. Lilley

SOAR '91, NASA/JSC, Houston, TX, 9-11 July 1991. "Spacecraft-Plasma Interaction Codes: NASCAP/GEO, NASCAP/LEO, POLAR, DynaPAC, and EPSAT." M. J. Mandell, G. A. Jongeward, and D. L. Cooke. (Conference proceedings available.)

Chapters 2 and 3 of this report present two-dimensional calculations of generic plasma interaction situations in which dynamic effects strongly influence measurable results. The work in Chapter 2 was motivated by observations by the MAIMIK rocket of spacecraft potentials far in excess of the energy of an emitted electron beam. This work shows that the oscillations of a beam emitted into an underdense plasma can cause this overcharging. Chapter 3 is an attempt to calculate, for fairly modest parameters, the effects of the sheath instability caused by orbital motion of a positive body. It shows that substantial potential oscillations occur, and that the electron current to the probe is enhanced.

Chapters 4-7 present work performed in support of SPEAR-II. Chapter 4 deals with the generic problem of plasma response to a sudden application of negative voltage to a probe. The calculation was done first with Gilbert, then duplicated with DynaPAC. It showed that it takes a long time to establish an equilibrium sheath, and that during this time ion currents to the probe can be enhanced by as much as an order of magnitude. Chapter 5 shows the application of these ideas to the sheath of the SPEAR-II high voltage probe, explaining the observed difference in probe reading between vacuum and plasma conditions. Actual DynaPAC calculations (performed post-test during the fall of 1990) of the actual plasma currents to the SPEAR-II high voltage components appear in Chapter 6. (It is worth noting that these calculations proceeded at a rate of one one-microsecond timestep per day on a Sun Microsystems SPARCStation I. Subsequently, DynaPAC recoding led to at least a factor of three speed increase, and transfer to an SGI Iris Indigo to another factor of three. Were we to repeat the calculation, we should be able to do several timesteps per day.) The SPEAR-II calculations are tied together and summarized in S-Cubed's contribution (partially supported by other contracts) to the SPEAR-II Products Report, which is included as Chapter 7.

Finally, Chapters 8-10 show some early work on the SPEAR-3 modeling. Chapter 8 describes a one-dimensional model, since incorporated into the EPSAT code, which provided early estimates for the neutral density required for breakdown of a negative sheath. Chapters 9 and 10 describe early work on the rocket floating potentials, collected currents, and current distribution to the particle detectors. With the benefit of this work, we were able to improve our computational models and update our geometrical models to obtain excellent results under the new contract.

2. DYNAMICS OF SPACECRAFT CHARGING BY ELECTRON BEAMS

This work was presented at the Spacecraft Charging Technology Conference, Monterey, CA, 30 October through 2 November, 1989. It was published in the conference proceedings. It also appeared in the Interim Report (30 September 1990) for this contract.

Dynamics of Spacecraft Charging by Electron Beams

M. J. Mandell and I. Katz

S-CUBED Division of Maxwell Laboratories, La Jolla, California

When a spacecraft or rocket emits an electron beam into an underdense plasma, it can charge to potentials in excess of the beam energy. We show calculations in which 8 keV beams are emitted along and across the earth's magnetic field, with parameters appropriate to the MAIMIK rocket. As was observed on MAIMIK, the spacecraft charged to potentials in excess of the beam potential due to energization of beam electrons by beam-generated electrostatic oscillations. This is in contrast to the low levels of charging often seen in denser environments, where higher plasma currents, coupled with ionization of neutrals, hold spacecraft potentials below a few hundred volts.

The beam structure and the spacecraft potential oscillate at a frequency corresponding to the mean lifetime of the beam electrons. These oscillations energize the beam electrons, and also pump energy into the ambient plasma, which exhibits lower frequency oscillations. The peak spacecraft potential is over 1 kV in excess of the beam energy. For the cross-field case, the oscillation frequency is proportional to the beam current for sufficiently intense beams.

Following beam turn-off, there is an immediate return of unscattered beam electrons and a longer term dissipation of scattered beam electrons. Analytic estimates are presented for the decay and overshoot of the spacecraft potential.

INTRODUCTION

A number of electron beam experiments have measured results that apparently violate conservation of energy. The SEPAC experiment (Reasoner *et al.*, 1984) measured a spectrum of returning electrons extending to energies well above that of the emitted beam, and the MAIMIK rocket (Maehlum *et al.*, 1988; Denig, Maehlum and Svenes, this conference) was charged by an 8 keV electron beam to potentials as high as 14 keV. Katz *et al.* (1986) performed a planar calculation that showed that oscillations of the beam electrons led to the spectral broadening seen in the SEPAC experiment. In this paper, we show 2-dimensional calculations, with parameters appropriate to MAIMIK, illustrating that space charge oscillations associated with the electron beam lead to rocket potentials in excess of the beam energy.

The electron beam on MAIMIK was directed nearly across the earth's magnetic field. The geometry of an intense beam directed across a magnetic field is shown in Figure 1a. If the spacecraft is near the beam energy, the beam electrons will be slowest at their farthest excursion from the spacecraft and will form a space charge maximum. This space charge maximum breaks the azimuthal symmetry of the problem, so that electrons may be scattered from their original gyro-orbits and leave the vicinity of the spacecraft. Unfortunately, this is a truly 3-dimensional situation and, therefore, very difficult to model.

Two beam configurations that can be modeled in 2-dimensional axisymmetric geometry are shown in Figures 1b and 1c. Figure 1b shows a beam directed along the magnetic field. An intense virtual cathode is formed. Most of the beam electrons move outward

from the virtual cathode and are attracted back to the spacecraft, which they impact from behind. A few of the beam electrons continue along the magnetic field line and escape the vicinity of the spacecraft. Figure 1c illustrates an "equatorial" beam, in which electrons are directed across the magnetic field from the entire spacecraft circumference. A ring of maximum space charge appears around the spacecraft. Because the space charge maximum is a full ring rather than a localized region, we expect it to be less intense than would be the case for a physical beam of the same current. Also, the space charge maximum is less effective at scattering because it does not break azimuthal symmetry.

The calculations described here were performed using an S-CUBED-developed, finite-element, electrostatic particle-in-cell code named Gilbert. Gilbert is a flexible, multi-purpose code with many special features. For these calculations, the space around the spacecraft was gridded with biquadratic elements of variable resolution to a distance of ten meters. Each element represents a volume of space corresponding to its area revolved in a full circle about the symmetry axis. For the "equatorial" beam, the calculation took advantage of mirror symmetry about the equatorial plane. The computational grids for the two cases are shown in Figure 2.

PHYSICAL PARAMETERS

Table 1 shows the physical parameters used in the calculation. The parameters listed in the "current collection" category are calculated for a spherical spacecraft at the beam potential of 8,000 volts.

Table 1. Problem Parameters

<u>Geometrical Parameters</u>	
Inner (spacecraft) Radius	0.3 m
Outer Radius	10.0 m
Magnetic Field	0.4 gauss
<u>Beam Parameters</u>	
Beam Current	0.16 amperes
Beam Energy	8000 eV
<u>Plasma Parameters</u>	
Electron/Ion Density	$3 \times 10^9 \text{ m}^{-3}$
Electron Temperature	1 eV
Ion Mass	16 amu
λ_D	13.6 cm
ω_{pe}	$3.1 \times 10^6 \text{ sec}^{-1}$
ω_{ce}	$7.0 \times 10^6 \text{ sec}^{-1}$
J_{th}	$8.0 \times 10^{-5} \text{ A-m}^{-2}$
<u>Current Collection</u>	
Langmuir-Blodgett Radius	10 m
Parker-Murphy Radius	1.54 m
Parker-Murphy Current	0.0025 amperes
Probe Charge	$2.7 \times 10^{-7} \text{ coulombs}$

The plasma surrounding the spacecraft is "underdense", in the sense that the Parker Murphy bound (Parker and Murphy, 1967) on the plasma return current is only a few percent of the beam current. Also, the electron plasma frequency is below the electron cyclotron frequency and, as we shall see, well below the oscillation frequency of the beam.

The radius of the computational space is taken equal to the radius of a space-charge-limited spherical sheath in this plasma, which is far larger than the Parker-Murphy radius for current collections. The effect of the plasma external to this radius is represented by a zero potential condition on this boundary. In retrospect, this approximation appears adequate to represent the beam dynamics, the ion dynamics, and the collection of ambient electrons but omits long-range transient effects on the ambient electron density.

CALCULATION FOR BEAM ALONG FIELD

The calculation begins with the grid of Figure 2a filled with electron and ion macroparticles (Figure 3a). The beam is projected along the magnetic field (Figure 3b) and initially exits the computational space. The negative beam charge and the positive charge left behind on the spacecraft produce a dipole potential (Figure 3c) that expels ambient electrons from the beam region (Figure 3d).

The spacecraft reaches beam potential about 2.5 microseconds after beam turn-on (Figure 4a), and the potential exhibits persistent oscillations (at 2×10^6 Hz) for the duration of the calculation (Figure 4b). During this time, the spacecraft remains always above the beam potential and has a peak potential of about 9,100 volts.

The beam conformation oscillates along with the spacecraft potential. Figure 5a shows the beam conformation when the spacecraft potential is fairly high. The bulk of the beam electrons are far from the spacecraft, having been emitted when the potential was low. Figure 5b shows beam conformation at a fairly low potential. In this case, the bulk of the beam electrons are close to the spacecraft, having been emitted at high potential. However, a pulse of energized electrons can be seen escaping along the field line.

Figures 6a and 6b show the electrostatic potential structure about the spacecraft. The sheath is elongated along the magnetic field due to quasi-trapping of ambient electrons that cannot be collected. The contours are distorted along the axis by the beam electron space charge (Figure 6a). At times, a negative potential well forms in the cross-field region (Figure 6b).

Figure 7a shows the amount of beam electron charge in the computational space, and Figure 7b shows the time dependence of the dipole moment of the beam electrons, defined as

$$\text{Dipole Moment} = \int \rho z d^3r$$

where ρ is the charge density of beam electrons. Since the dipole moment is oscillating at 2 MHz, we expect to see strong electromagnetic radiation at this frequency.

Figures 8abc show spectral analysis of some of the oscillating quantities. The potential (Figure 8a) shows a sharp peak at 2 MHz, with well-defined second and third harmonics. The beam dipole moment (Figure 8b) shows a sharp peak at 2 MHz, as well as a broad peak at the ambient electron plasma frequency (0.5 MHz). The dipole moment of the

ambient electrons (Figure 8c) shows little evidence of the 2 MHz oscillations but has a strong, broad peak near the ambient plasma frequency.

The beam charge (Figure 7a) varies from 0.04 to 0.08 μCoul . Dividing this by the beam current of 0.16 amperes shows that beam particle lifetimes fall mainly in the range 0.25 - 0.5 μsec . Noting also that the upstrokes in Figure 7a (strong return current) are steeper than the downstrokes (steadily emitted current) leads to the following interpretation. Most of the beam electrons return to the spacecraft in a short burst. Electrons emitted during the return burst see relatively weak retarding fields, travel far from the spacecraft, and have lifetimes of approximately a full oscillation period. Electrons emitted while the potential is rising see stronger retarding fields, travel smaller excursions, and return to the spacecraft at the same time as the long-lived electrons, producing the return current bunching. This bunching is similar to that seen by Katz *et al.* (1986).

Figure 9 shows the ion positions at the conclusion of the calculation (20 μsec). The ions have cleared a region of about two meters around the spacecraft. Thus the run time of this calculation is too short to approach the formation of an equilibrium "sheath".

CALCULATION FOR BEAM ACROSS FIELD

A similar calculation was performed for an equatorial beam directed across the magnetic field in the grid of Figure 2b. (Note that in this calculation we have taken advantage of mirror symmetry about the $z = 0$ plane. Values for current and charge will be quoted at double the computed values, so that they are characteristic of a complete sphere.)

The beam electrons at the conclusion of the calculation are shown in Figure 10. The figure shows a main stream of electrons emitted from the spacecraft, slowed by the electric field and turned by the magnetic field, then returning to the spacecraft. In addition, there is a column of beam electrons extending in the magnetic field direction. The mechanism for populating this column is that a beam electron in its initial orbit gains enough momentum along the magnetic field to miss the spacecraft on its first return passage, and while passing near the spacecraft receives a substantial impulse along the field. Electrons leave the column by either impacting the spacecraft or escaping the grid.

Figures 11ab show the time history of the spacecraft potential. Four different current values were used. From Figure 11b we see that, while doubling the current led to some increase in the mean potential and its oscillation amplitude, the main effect is to double the frequency.

Figures 12ab show the potential contours about the spacecraft at two different times. As in the previous case, the sheath is elongated along the field line, and a negative potential well is sometimes seen in the cross-field region.

Figure 13 shows the ambient electron macroparticles. The ambient electron population was maintained by generating the plasma thermal current at the spherical problem boundary out to a radius of eight meters. A low density region is seen to extend along the field line from the spacecraft; electrons in this region are allowed by the theory of Parker and Murphy (1967) to be collected by the spacecraft. A high-density cloud of electrons is seen in the cross-field region, as these electrons cannot be collected by the spacecraft and have low probability of escaping the grid. This ambient electron charge density structure is the cause of the elongated potential contours shown in Figures 12ab and 6ab.

$$dV/dt = (I_0/C) (V/V_0)^{1/2}$$

where I_0 is the Parker-Murphy current at potential V_0 (- 0.0025 amperes at 8,000 volts) and C is the spacecraft capacitance (3.4×10^{-11} farads). The solution is

$$t_2 - t_1 = -2.4 \times 10^{-6} (V_2^{1/2} - V_1^{1/2})$$

which gives a discharge time of about 200 μ sec. Since the thermal ion speed is only a few thousand $\text{m}\cdot\text{sec}^{-1}$, it will take about a millisecond for the ions to repopulate a sheath a few meters in radius. Assuming a thermal electron distribution, the spacecraft will charge negatively during this time according to

$$dV/dt = 4\pi a^2 J_{th} e^{V/\theta} / C$$

whose solution is

$$V/\theta = -\ln(1 + t/\tau)$$

$$\tau = C \theta / (4\pi a^2 J_{th})$$

For our parameters, τ is about 0.4 μ sec, and we expect an overshoot to about -8 volts. However, if the electron distribution has an elevated thermal tail, as is likely due to turbulence associated with the nonuniform, nonequilibrium ion distribution, the negative overshoot will be much greater.

CONCLUSIONS

Electron beams emitted from spacecraft in the ionosphere exhibit complex behavior. We have analyzed here the case of a beam emitted into an underdense plasma, with parameters appropriate to the MAIMIK rocket. The beam was emitted both along the magnetic field and across the field in an "equatorial" fashion.

The beam-emitting system exhibits oscillations at a few megahertz. These oscillations are associated with bunched return of the beam electrons and cause electron energization so that the spacecraft can achieve potentials in excess of the beam energy. At least for the field-aligned beam case, these oscillations are dipolar in character and should be observable as electromagnetic radiation. For sufficiently intense beams, the oscillation frequency is proportional to the beam current.

The dynamics of the ambient plasma is largely independent of the beam dynamics. The ambient electrons show a broad peak at their own plasma frequency and form an elongated sheath.

Even in this very underdense plasma, the relaxation of spacecraft potential following beam turn-off is rapid compared with the time for ions to thermally fill in the sheath. If the nonuniform plasma that exists during this time causes electron heating, a substantial negative overshoot of the spacecraft potential can occur.

Acknowledgement. This work was supported by the Geophysics Laboratory, Hanscom Air Force Base, Massachusetts, under contract F19628-89-C-0032.

Table 2 shows the range of beam charge, range of beam electron lifetime, and oscillation period for the different values of emission current. As with the field-aligned beam, the oscillation period is near the maximum beam particle lifetime. Except for the lowest current value, the beam charge increases only slightly when the current is doubled. This is because the maximum beam charge is approaching the charge on the sphere. When the current is doubled, a modest increase in mean spacecraft potential is sufficient to reduce the particle excursion distance and cut the beam particle lifetime by half. This point is further illustrated by Figure 14, which plots the quantity

$$\int \rho r d^3r$$

The average and oscillation amplitude of this quantity varies slowly as the sheath is being formed, but shows no abrupt changes as the current is altered, leading to the conclusion that the system rapidly adjusts so that the beam charge times its excursion distance is independent of current.

Table 2. Beam Charge, Lifetime, and Oscillation Period for Equatorial Beam

Current (Amperes)	Charge (μcoul)	Lifetime (μsec)	Period (μsec)
0.16	0.07 - 0.1	0.44 - 0.62	0.62
0.32	0.12 - 0.2	0.38 - 0.62	0.47
0.64	0.13 - 0.21	0.20 - 0.33	0.28
1.28	0.14 - 0.25	0.11 - 0.19	0.18

BEAM TURN-OFF

Several papers at this conference discussed beam turn-off, showing that the spacecraft potential tends to overshoot and achieve a negative value. This led us to investigate the behavior of the equatorial beam system after turn-off of the 0.160 ampere beam.

Figure 15 shows the behavior of the spacecraft potential and the beam charge following beam turn-off. Most of the beam charge is promptly collected, dropping the spacecraft potential to 7,200 volts. Approximately 0.03 μcoul of charge remains in the field-aligned column of scattered beam electrons, which decays with a time constant of 2.1 μsec . About three-quarters of this depopulation rate results from electrons escaping the grid, and about one-quarter from electrons recaptured by the spacecraft. (When the spacecraft is at elevated potential, the escape rate must balance the Parker-Murphy collected current, leading to a 12 μsec time constant for escape.)

If the spacecraft discharges by collecting the Parker-Murphy current, its potential will follow the equation

REFERENCES

- Denig, W. F., B. N. Maehlum, and K. Svenes, A review of the MAIMIK rocket experiment, (this conference, 1989).
- Katz, I., G. A. Jongeward, D. E. Parks, D. L. Reasoner and C. K. Purvis, Energy broadening due to space-charge oscillations in high current electron beams, *Geophy. Res. Lett.*, **13**, 64, 1986.
- Maehlum, B. N., J. Troim, N. C. Maynard, W. F. Denig, M. Friedrich, and K. M. Torkar, Studies of the electrical charging of the tethered electron accelerator mother-daughter rocket MAIMIK, *Geophy. Res. Lett.*, **15**, 725, 1988.
- Parker, L. W., and B. L. Murphy, Potential buildup on electron-emitting ionospheric satellites, *J. Geophys. Res.*, **72**, 1631, 1967.
- Reasoner, D. L., J. L. Burch, and T. Obayashi, Analysis of electron spectra produced by SEPAC electron beams on Spacelab-1 - evidence for strong beam plasma interactions, *EOS Trans. Am. Geophys. Union*, **65**, 1042, 1984.

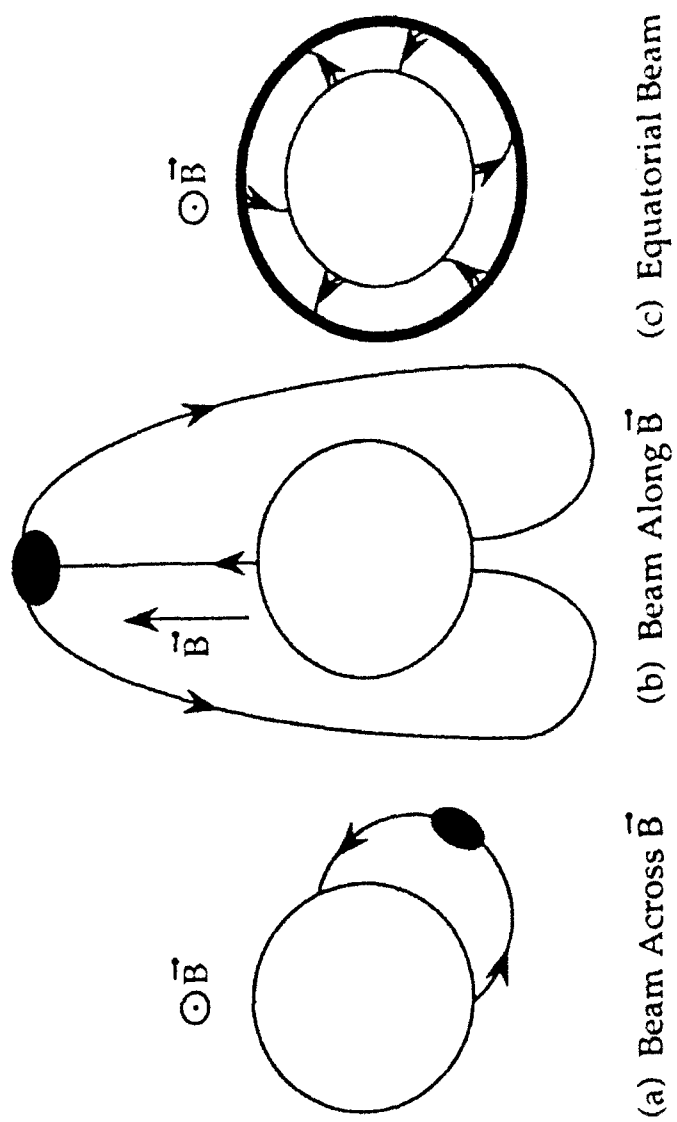


Fig. 1. Three beam configurations from a spherical spacecraft: (a) physical beam across magnetic field; (b) physical beam along magnetic field; (c) "equatorial" beam across magnetic field.

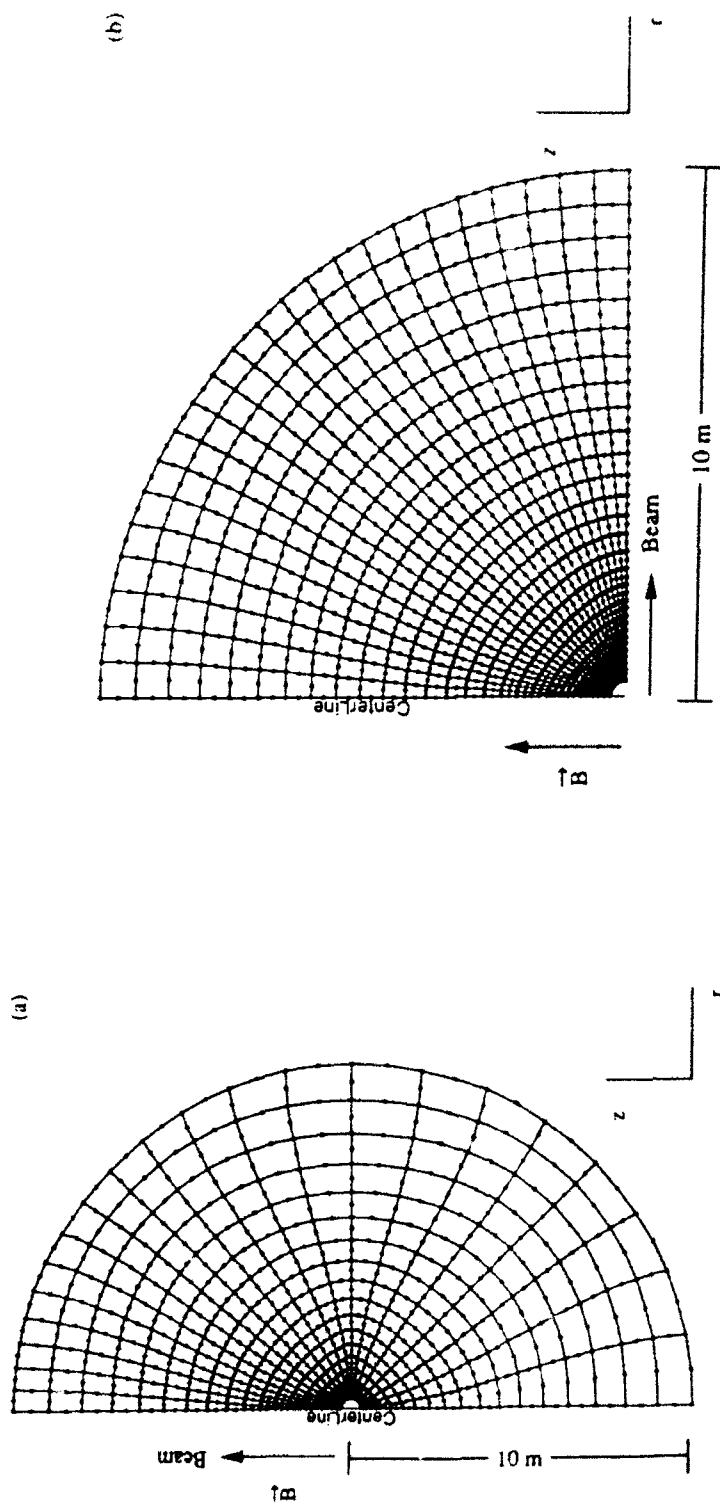


Fig. 2. Axisymmetric grids of biquadratic elements used in these calculations: (a) grid used for calculation of beam along magnetic field (fig. 1a); (b) grid used for calculation of "equatorial" beam (fig. 1b) using mirror plane.

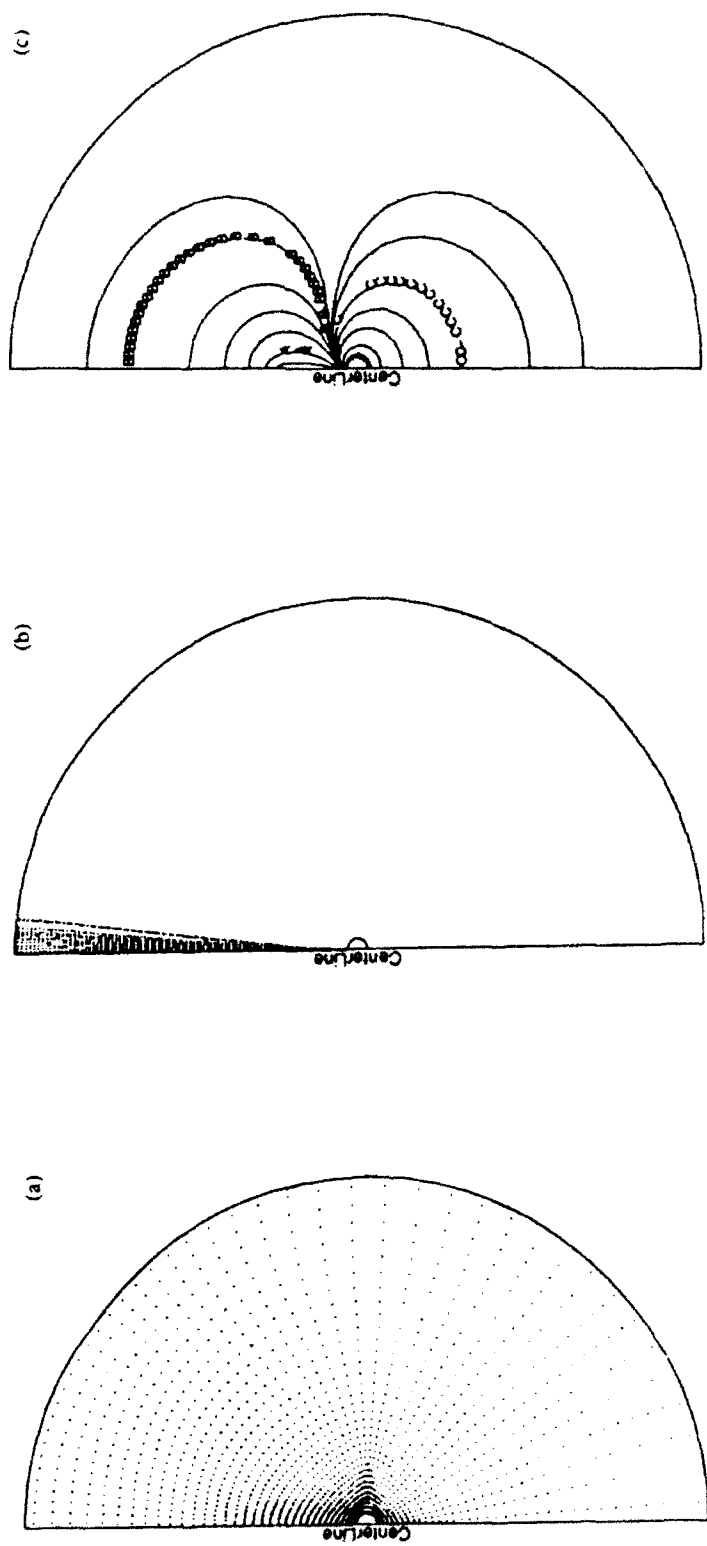


Figure 3. (a) Initial electron or ion macroparticles in grid of fig. 2a; (b) beam electron macroparticles at 0.2 μsec ; (c) dipolar potential at 0.04 μsec , with contours marked A, B, and C at -50, -2, and +5 volts.

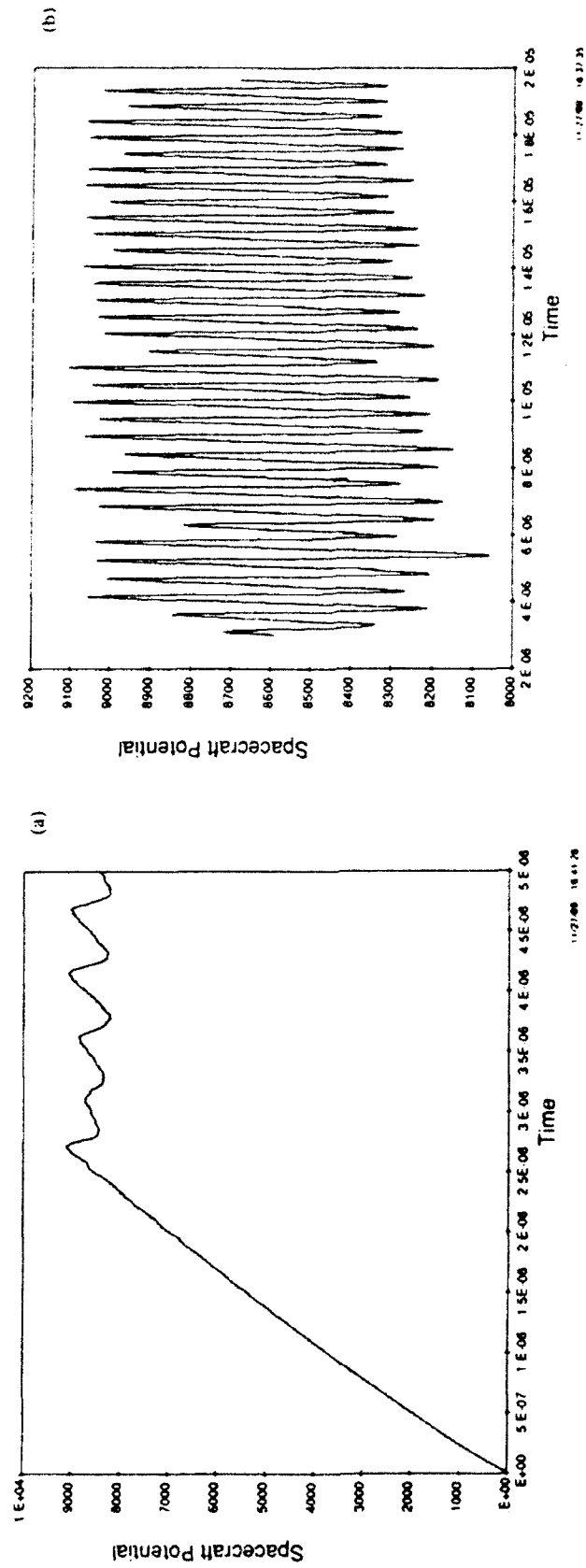


Fig. 4. Time dependence of spacecraft potential for field-aligned beam: (a) initial transient; (b) persistent oscillations.

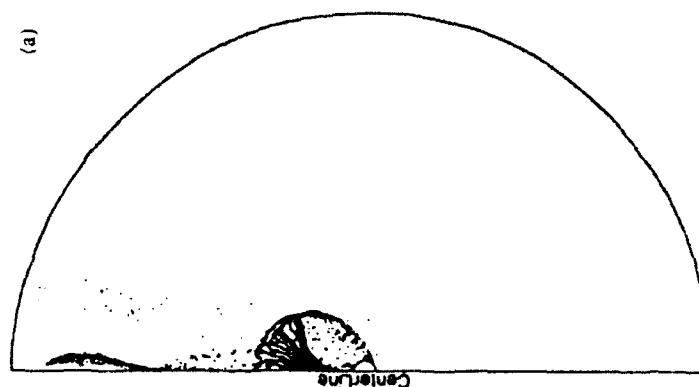
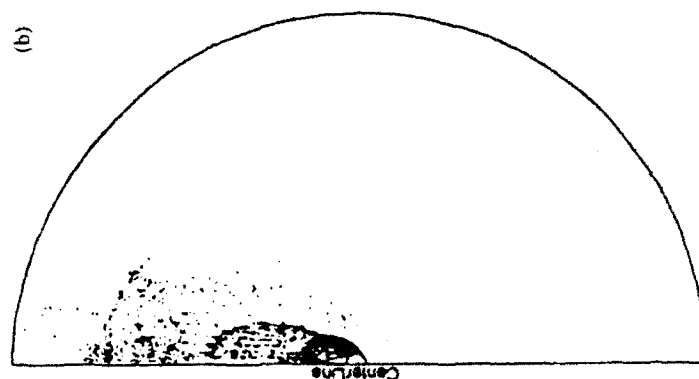


Fig. 5. Beam conformation (a) at high potential; (b) at low potential.

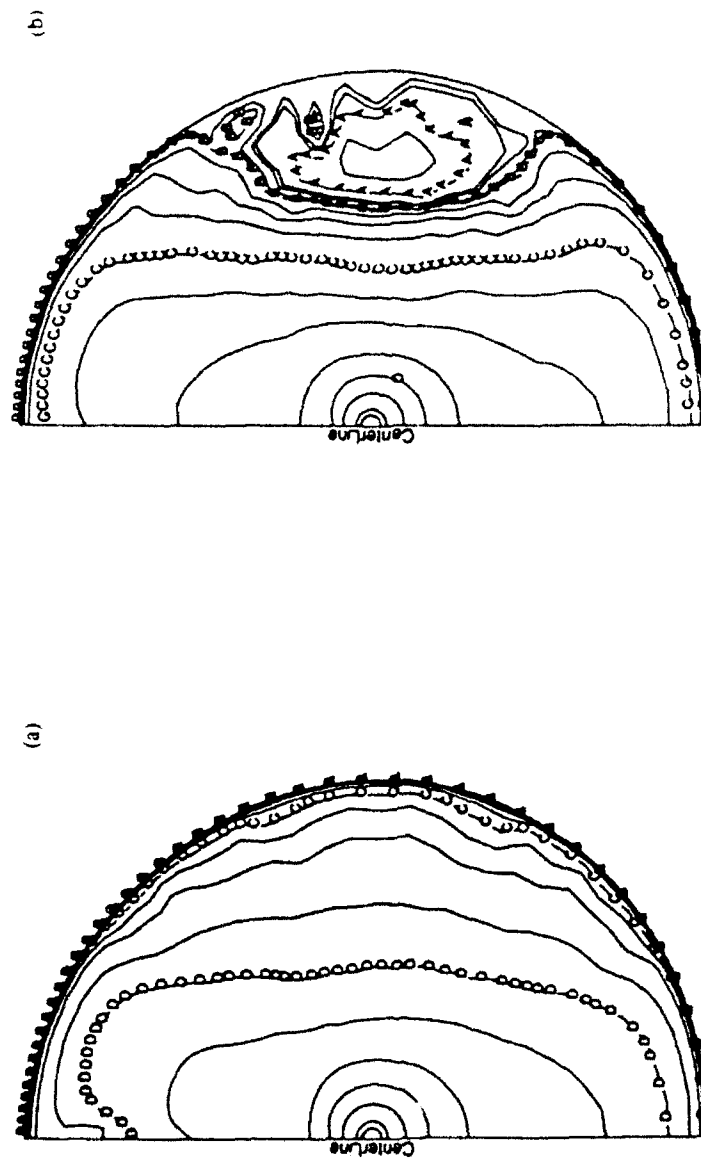


Fig. 6. Electrostatic potential structure (logarithmically spaced contours) about the spacecraft (a) without and (b) with negative potential well in the cross-field region.

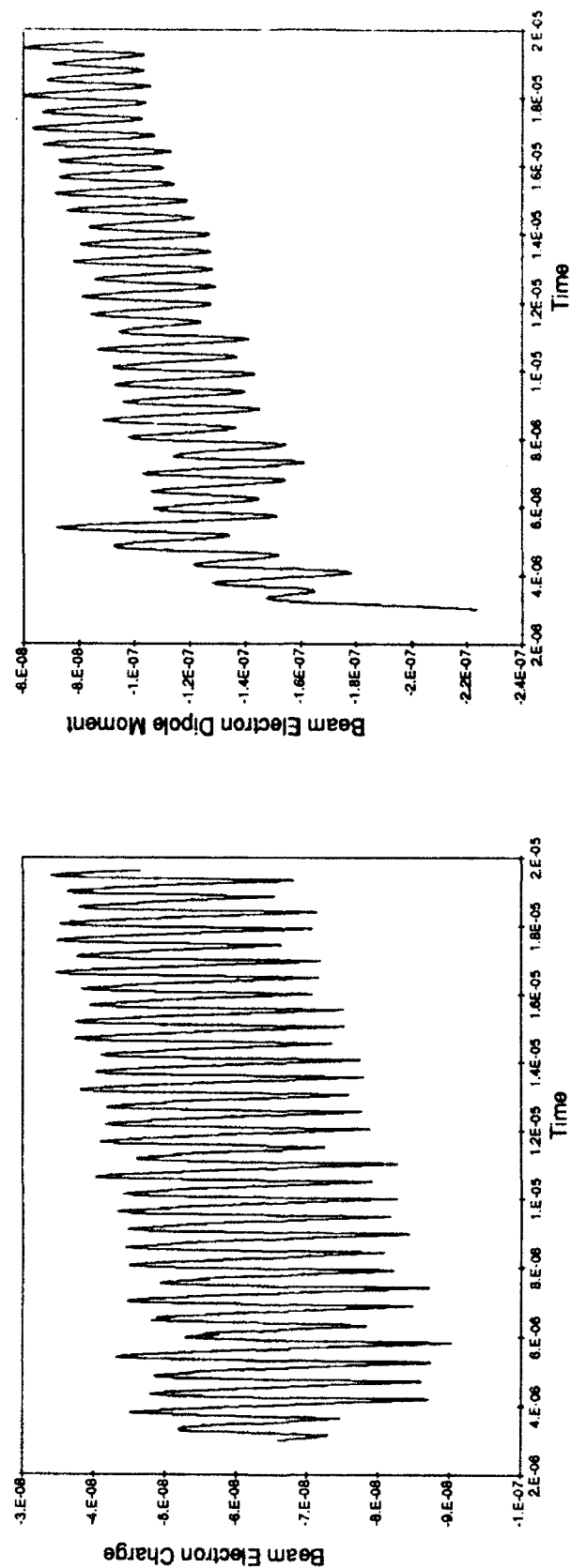


Fig. 7. Time dependence of (a) beam electron charge; and (b) beam electron dipole moment.

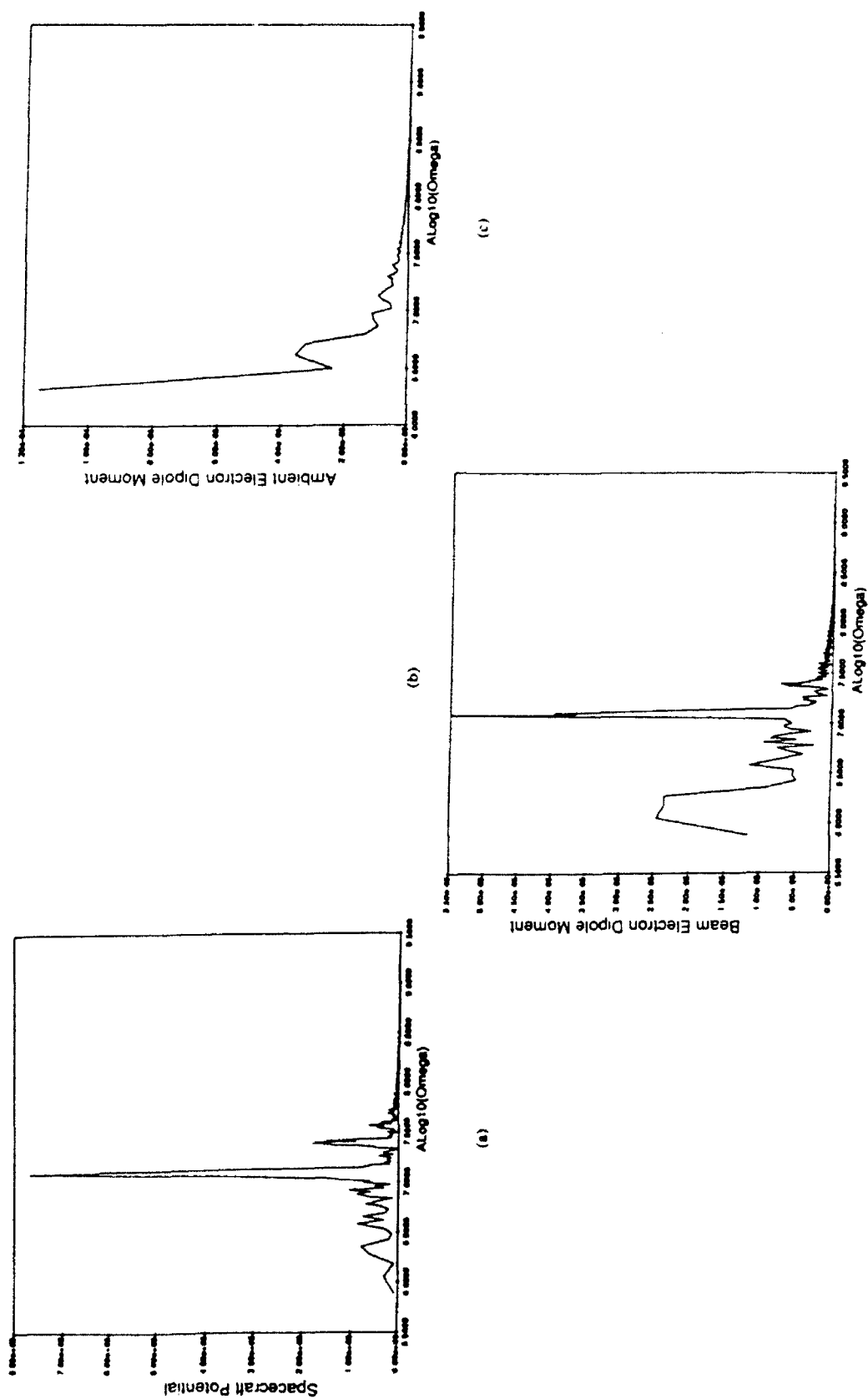


Fig. 8. Spectral analysis of (a) spacecraft potential; (b) beam electron dipole moment; (c) ambient electron dipole moment.

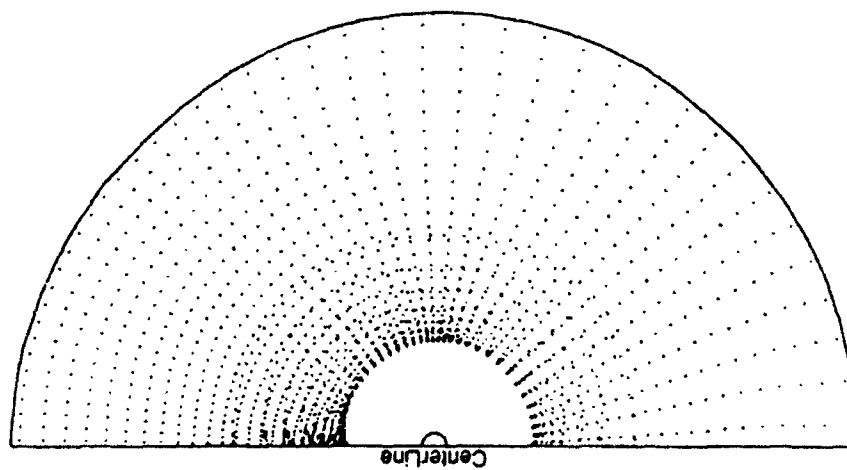


Fig. 9. Ion positions after 20 μ sec.

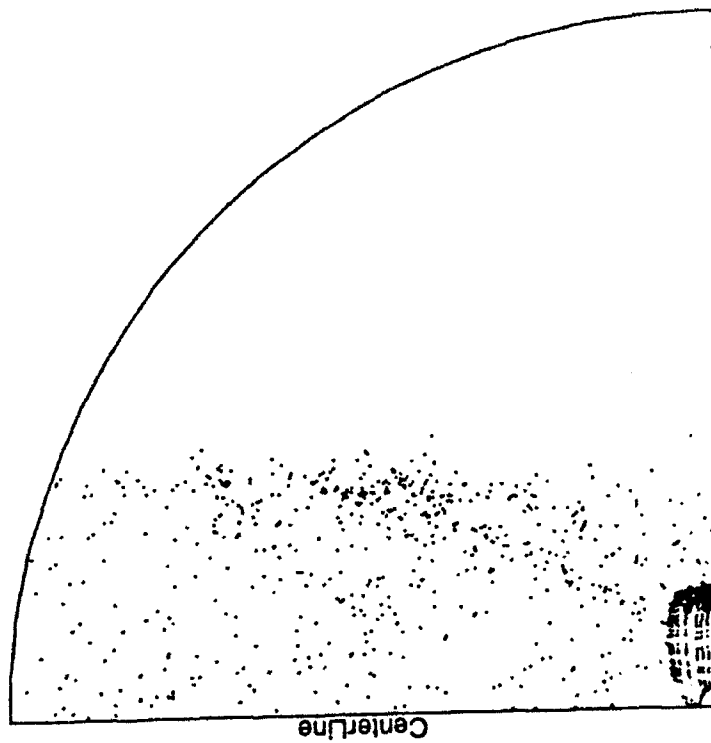


Fig. 10. Beam electrons at conclusion of equatorial beam calculation, showing circulating beam of unscattered electrons, and field aligned column of scattered electrons.

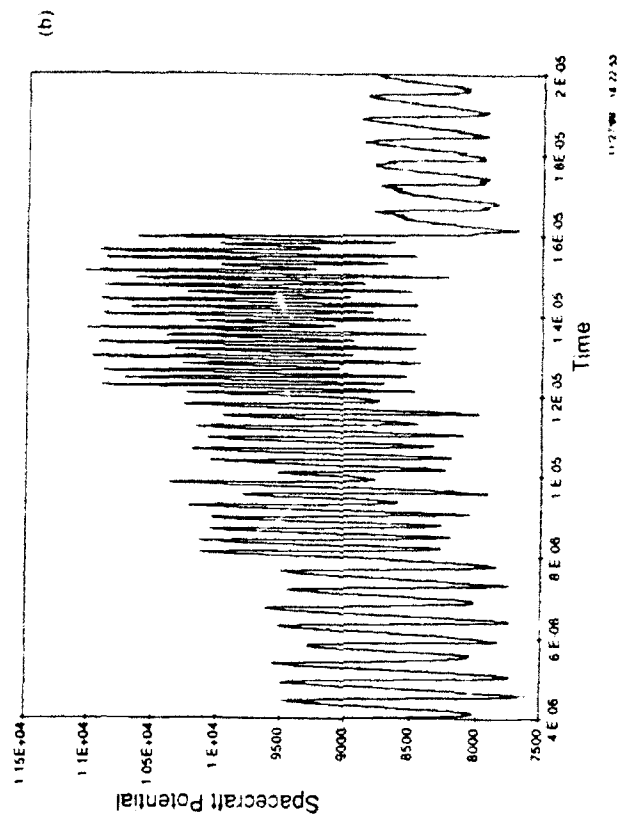
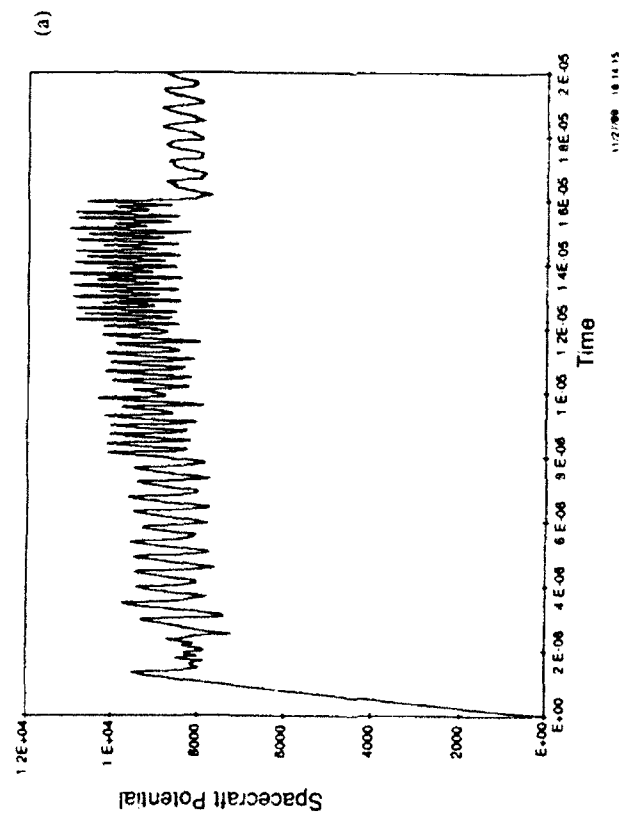


Fig. 11. Time dependence of spacecraft potential for equatorial beam: (a) initial transient; (b) persistent, current-dependent oscillations.

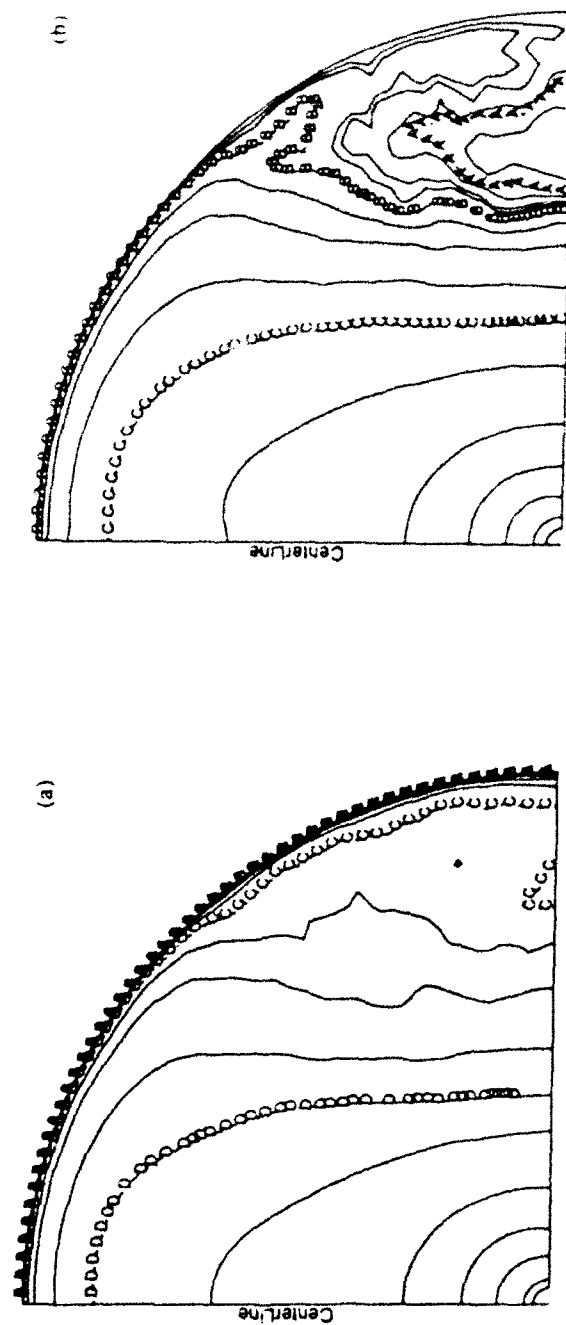


Fig. 12. Electrostatic potential structure (logarithmically spaced contours) about the spacecraft (a) without and (b) with negative potential well in the cross-field region.

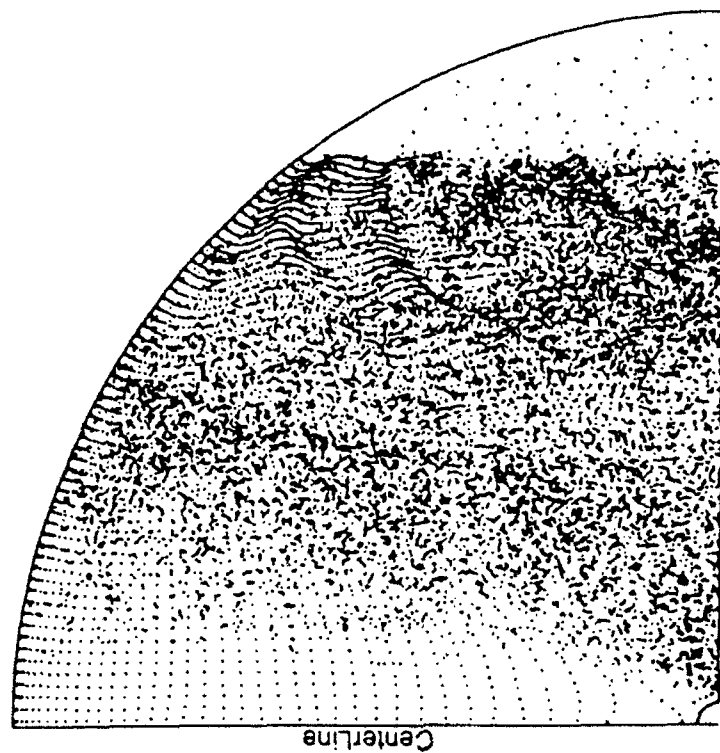


Fig. 13. Ambient electron macroparticles, showing low axial density and high cross-field density.

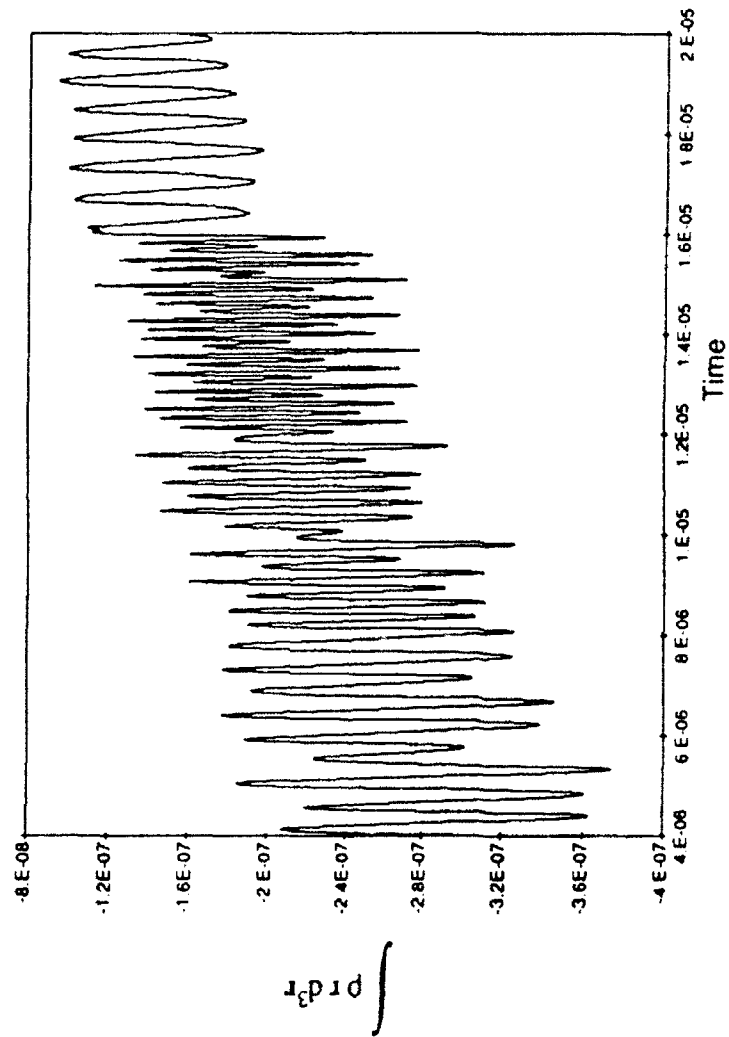


Fig. 14. The quantity $\int \rho r d^3r$ for the beam electrons, showing the lack of dependence on string current changes.

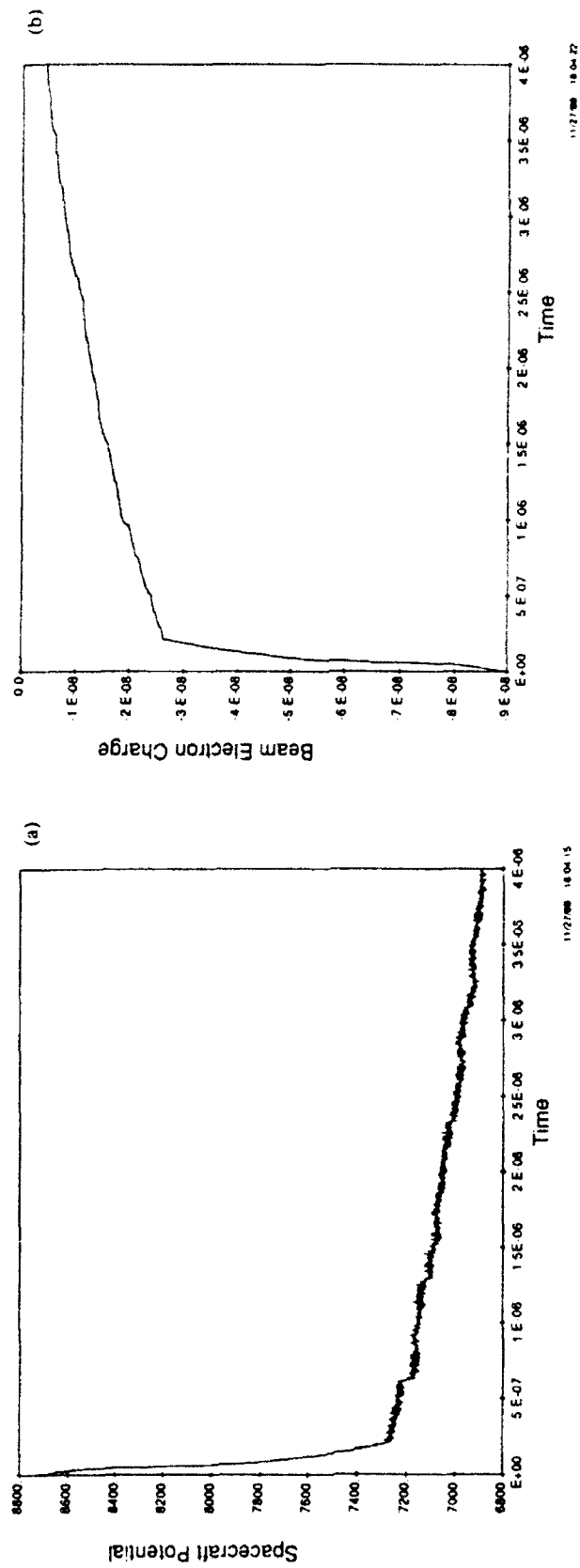


Fig. 15. Behavior following beam turn-off: (a) spacecraft potential; (b) beam electron charge.

3. POSITIVE ORBITAL PROBE CALCULATION

This work appeared in the Quarterly Report for 1 January through 31 March 1991.

3. POSITIVE ORBITAL PROBE CALCULATION

3.1 RATIONALE

We are accustomed to performing "sheath" calculations of currents to spacecraft. The "sheath" is defined as the region (or boundary of the region) from which the repelled species is excluded. A common and apparently benign case for which this entire concept makes no sense is an orbiting ionospheric probe biased at, say, +10 volts. The repelled species (O^+ ions) will penetrate the potential structure to the 5-volt level. In order to understand the physics of this situation, we attempted to use Gilbert to perform a full-PIC simulation of this situation.

3.2 CALCULATION DESCRIPTION

Calculation parameters were chosen so that (1) the problem is realistic; (2) the zone size would not exceed a few Debye lengths; (3) the range of electron energies would be fairly tolerable; and (4) time-stepping on the electron timescale would eventually lead to correct ion motion. The calculation parameters (along with several derived quantities) are shown in Table 3.1.

Table 3.1 Parameters for the positive orbital probe calculation.

Probe Radius	0.1 m	
Probe Potential	10 V	
S/C Velocity	7500 m/sec	
Ram Energy (O^+)	5 eV	
Magnetic Field	None	
Plasma Density	10^{11} m^{-3}	
ω_{pe}	1.78×10^7	
$\log_{10} \omega_{pe}$	7.25	
Electron Temperature	0.1 eV	1 eV
Debye Length	$7.44 \times 10^{-3} \text{ m}$	$2.35 \times 10^{-2} \text{ m}$
Elec. Th. Curr.	$8.46 \times 10^{-4} \text{ A/m}^2$	$2.68 \times 10^{-3} \text{ A/m}^2$
L.-B. Radius	0.26 m	0.22 m
L.-B. Current	0.72 mA	1.63 mA

We have included derived parameters for 1 eV as well as 0.1 eV electron temperature because it can be argued that the boundary conditions had the effect of raising the effective electron temperature. However, the calculated electron current to the probe was 3.84 mA, which is more than double the probe current in a stationary 1 eV plasma.

Figure 3.1 shows the axisymmetric computational grid for the problem. Conductor 1 represents the probe. Conductor 2 (0.5 m upstream of probe center) emits electrons and ram ions. Conductor 3 (0.5 m radially from probe center) and conductor 4 (0.3 m downstream from probe center) emit electrons only. The potential at conductors 2, 3, and 4 are held fixed at 0 volts, while conductor 1 is held fixed at +10 volts.

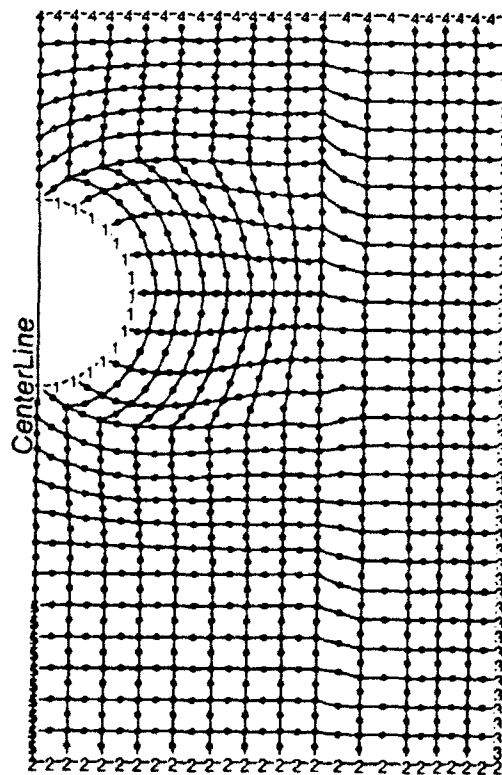


Figure 3.1 Axisymmetric Computational grid for positive potential orbital probe. Grid is 50 cm in radius and 80 cm in height.

Even though boundaries 2 and 3 are well beyond the Langmuir-Blodgett sheath distance, it was necessary to emit more than the plasma thermal current to avoid a sharp potential rise at the boundary. The emission used followed the relation

$$J = 2.33 \times 10^{-6} V^{3/2}/d^2 + 2.12 \times 10^5 n e V^{1/2}$$

where n is the ambient ion density and V is the potential at the zone boundary at distance d . This equation comes from treating a constant ion density as a perturbation to the Child-Langmuir problem.

The calculation proceeded by first running long enough for the ions to fill the grid and establish an apparent steady state, then resetting the clock and continuing to run and take data.

3.3 CALCULATION RESULTS

Figure 3.2 shows a snapshot of the ion positions toward the end of the calculation. The stagnation line is well-defined from about 30 to 90 degrees. Below 30 degrees, a high amplitude of electrostatic noise blurs the stagnation line. Because (as we shall see) the stagnation line is a potential maximum, it is blurred beyond 90 degrees because ion trajectories cannot stably follow the potential maximum.

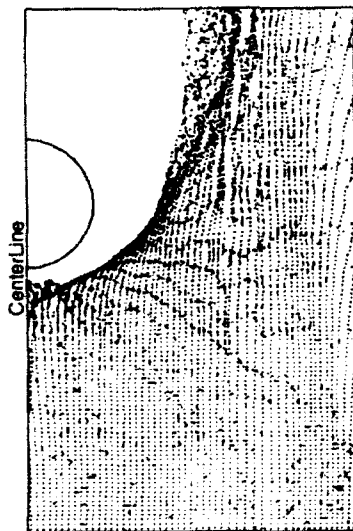


Figure 3.2 Ion macroparticle positions for positive orbital probe.

Figures 3.3 (a and b) show potential contours at two slightly different times. The potential maximum along the stagnation line (which shows up clearly in Gouraud-shaded potential plots) is seen as an extension of the +1 volt contour toward an island of +1 volt potential at the upper right. Part of the stagnation line is held below +1 volt due to the influence of the electron-rich wake region. Figures 3.4 (a and b) plot potentials along radial lines at $z = 0.0$ and $z = 0.2$ (relative to the probe center), showing more clearly the potential maximum at the stagnation line, occurring at $r = 0.21$ and $r = 0.31$ respectively.

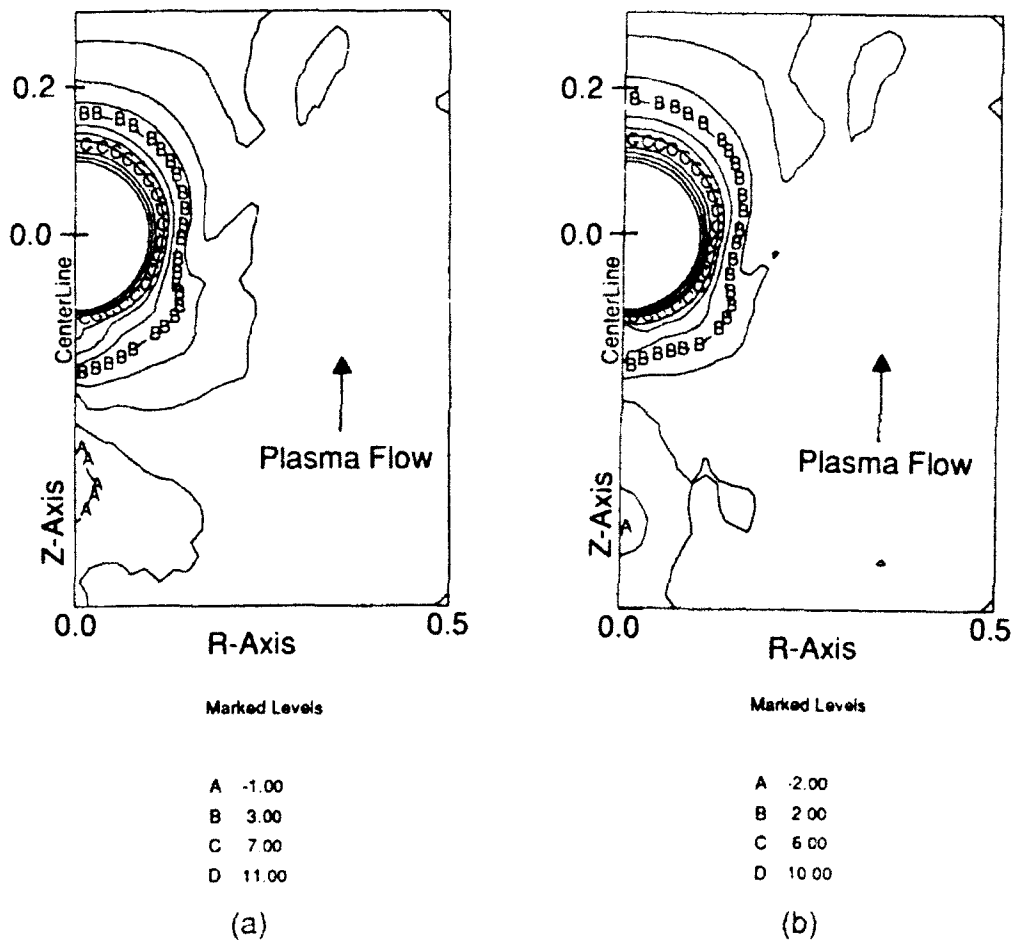
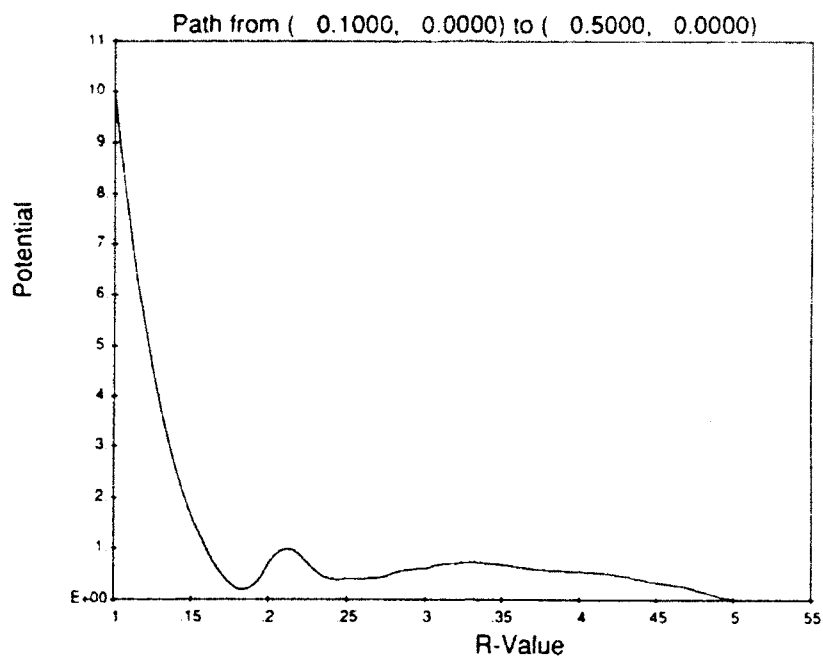
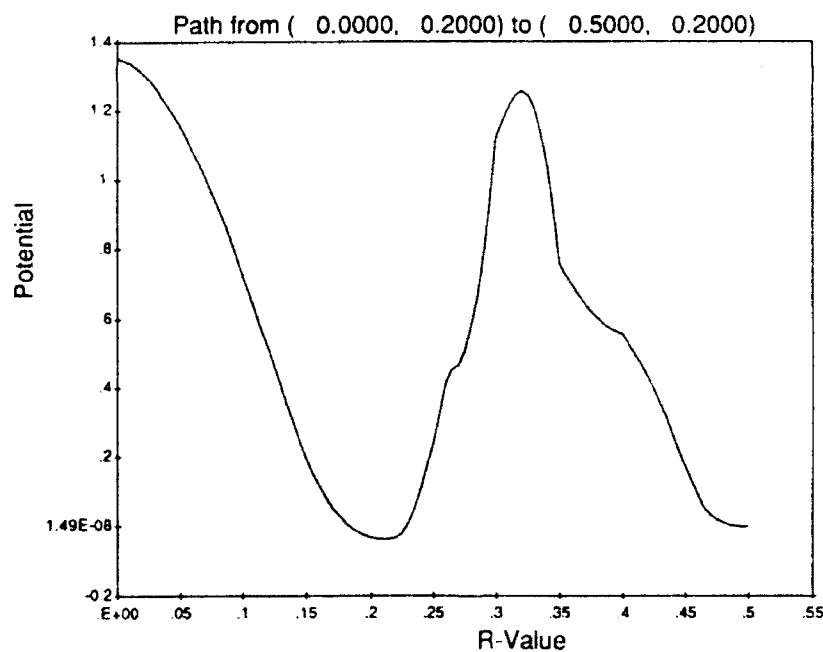


Figure 3.3 Potential contours around positive orbital probe for two slightly different times. Spacecraft velocity is downward, or, alternatively, plasma flow is upward.



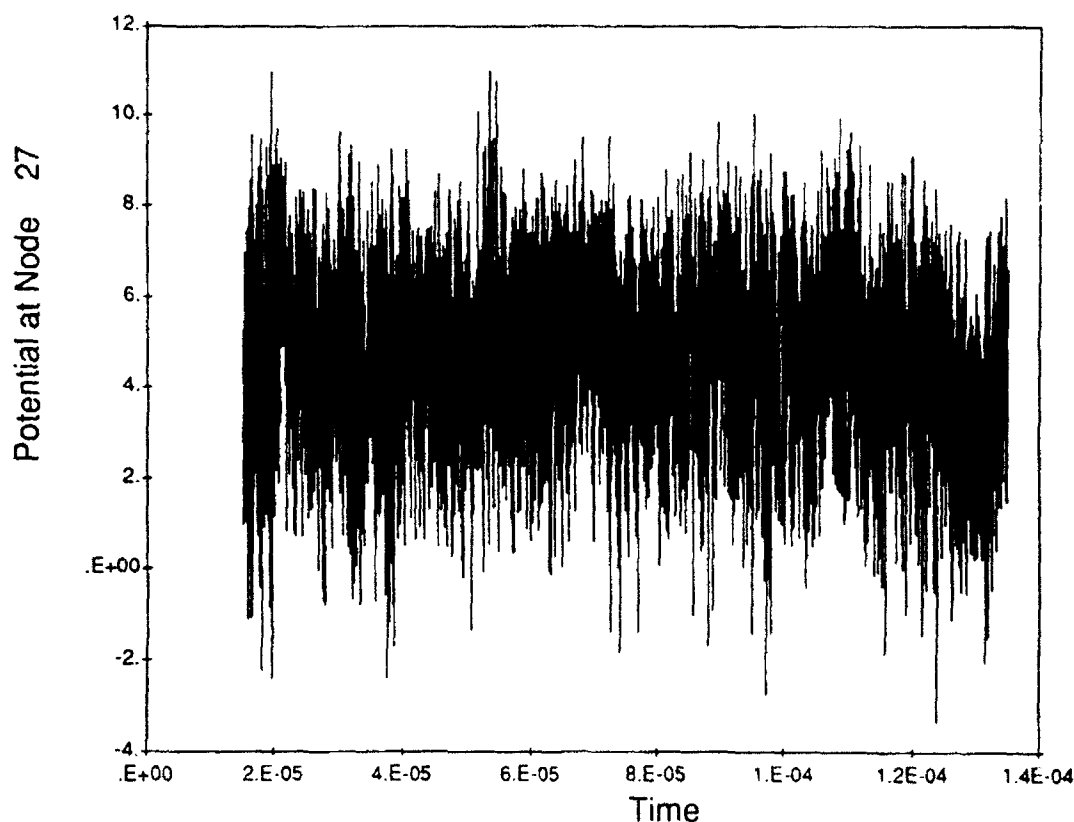
(a)



(b)

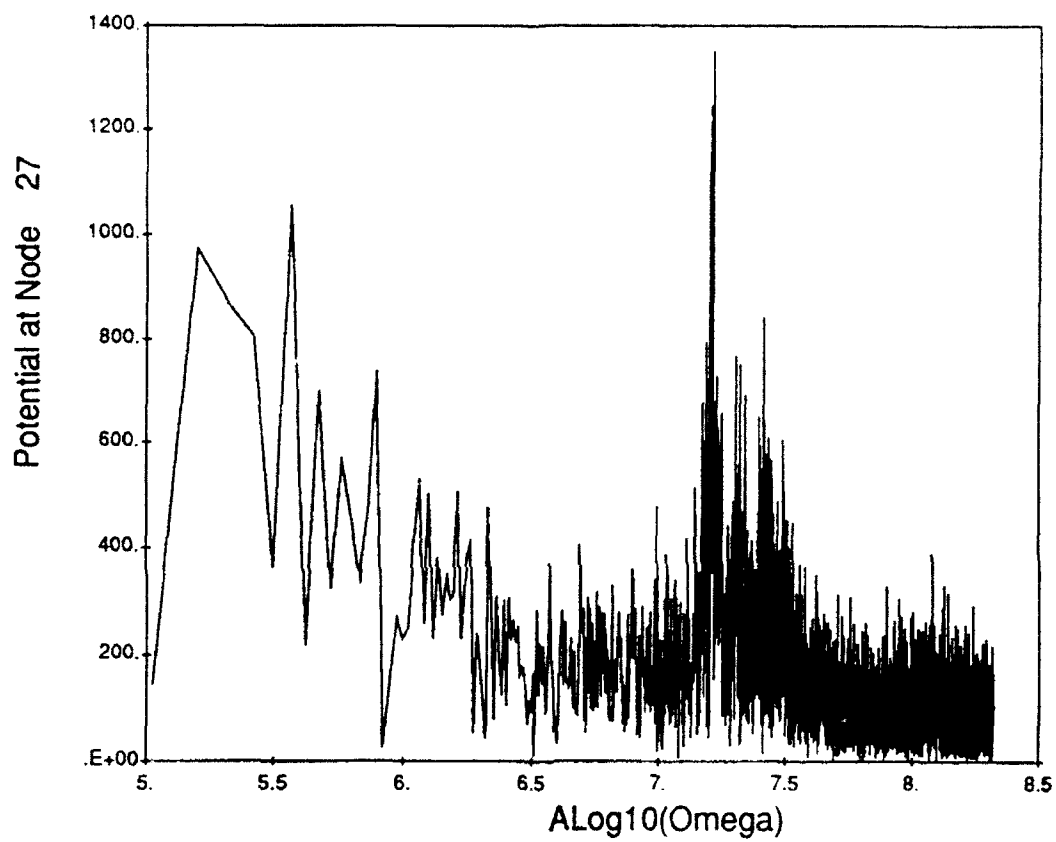
Figure 3.4 Potential plots along radial lines showing maximum at ion stagnation line: (a) radially outward from probe, showing maximum at 21 cm; (b) twenty cm downstream of probe center, showing maximum at 30 cm.

Both figures 3.3 (a and b) show regions of negative potential in the upstream direction. These regions are formed on the axis and grow outward. The timescale for this process is the electron plasma frequency. Figures 3.5 (a, b, c, and d) show the time and frequency domain behavior of the potential at node 27 (3.3 cm upwind of the sphere surface) and at node 122 (15 cm upwind of the sphere surface). At node 27, the noise level is tremendous, with a clear peak at the plasma frequency. Further from the sphere, at node 122, the amplitude of the oscillations is much lower, and the frequency behavior much cleaner.

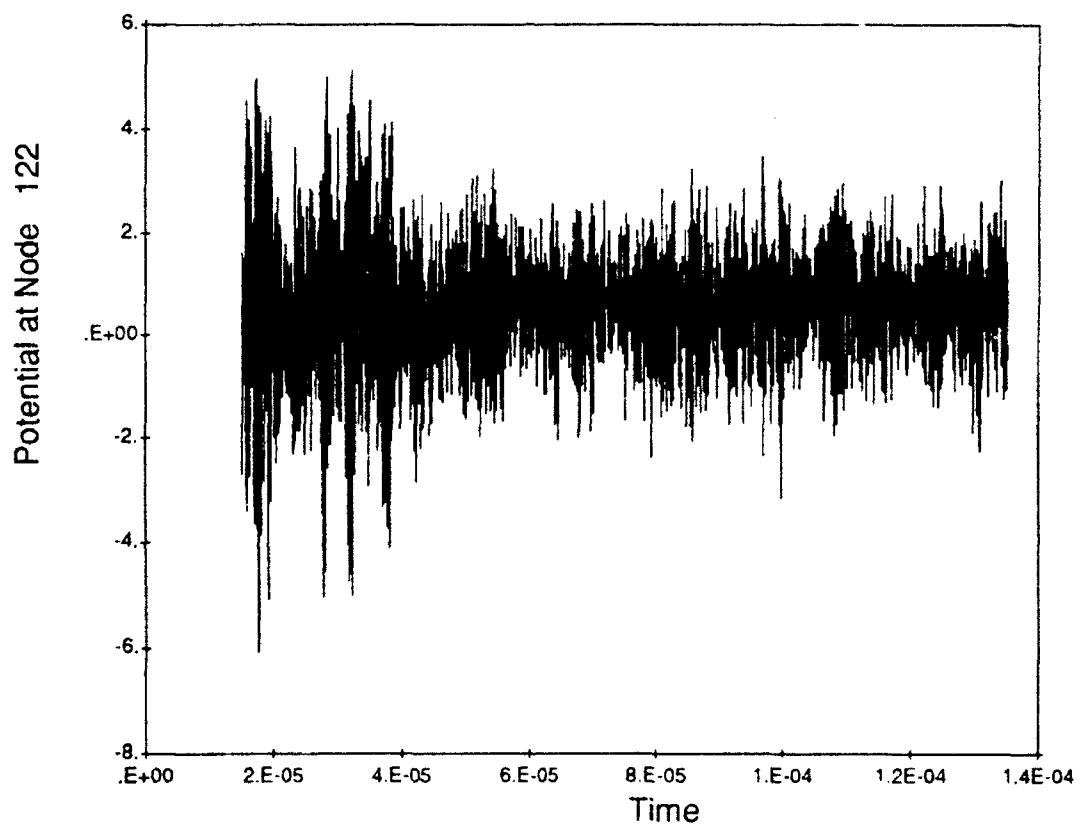


(a)

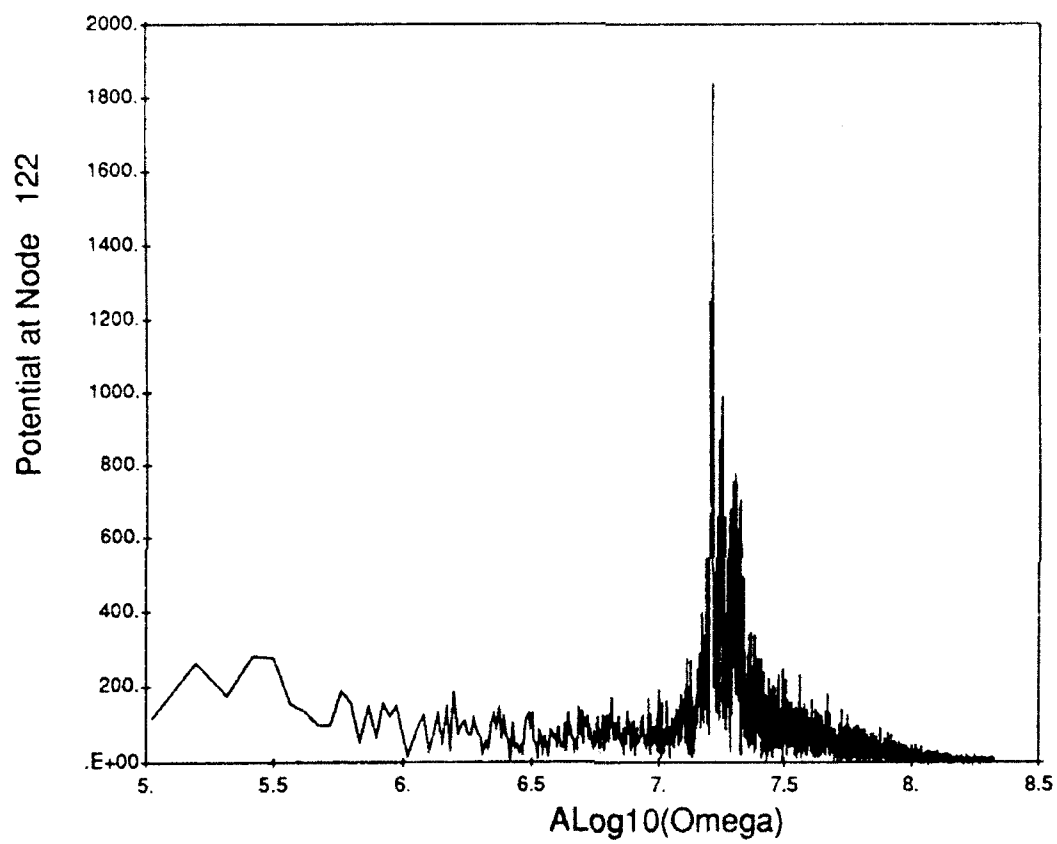
Figure 3.5 Potential fluctuations in time and frequency domain: (a) 3.3 cm upstream, time domain; (b) 3.3 cm upstream, frequency domain; (c) 15 cm upstream, time domain; (d) 15 cm upstream, frequency domain.



(b)



(c)



(d)

3.4 DOUBLE-LAYER MODEL

Noting that we have a high current to the sphere, we are motivated to the following calculation. Suppose we have (for simplicity) a planar sheath with ions penetrating to the level ϵ . Regarding the plasma as being a cold electron source at the 0-potential level, how much electron current is required to make to zero-to-five (i.e., ϵ) volt region a stable double layer, and how thick is the layer?

The double layer has incident and reflected ion currents and transmitted electron currents, so that Poisson's equation for the layer region is

$$-\epsilon_0 \phi'' = p_0 \{ 2 [\epsilon(\epsilon - \phi)]^{1/2} - (\theta/4\pi\phi)^{1/2} \}$$

where p_0 is the ambient plasma density times the unit charge, and θ (to be determined) is the temperature required of the plasma for its one-sided thermal current to equal the minimum current for a stable double layer. Multiplying both sides by ϕ' enables us to integrate this equation once. If we then apply the boundary condition that $\phi' = 0$ at $\phi = 0$ and at $\phi = \epsilon$ we find that $\theta = 16\pi\epsilon$ and

$$(\phi')^2 = (2p_0/\epsilon_0) \{ 4[\epsilon(\epsilon - \phi)]^{1/2} + (\theta\phi/\pi)^{1/2} - 4\epsilon \}.$$

For a ram energy of 5 eV, a stable double layer at the sheath requires the electron thermal current of a 250 eV plasma!!! Since the actual temperature is 0.1 eV, we can only achieve such a current with a "convergence factor" of 50. This explains why an extended sheath (or presheath) must exist for ram electron collection. For the plasma density used above, we can also show that the thickness of a stable double layer would have a lower bound of about 3 cm.

4. TRANSIENT SHEATH DYNAMICS

This work appeared in the Interim Report (30 September 1990) for this contract. It had previously been presented at a SPEAR-II review, and was subsequently presented at the High Voltage Workshop, Port Hueneme, CA, 19-21 March, 1991.

4. TRANSIENT SHEATH DYNAMICS

We have long suspected that SPEAR II would not establish an equilibrium sheath because of the long time required for ions to clear the sheath. The equilibrium sheath radius for SPEAR II is about two meters, while the most optimistic ion speed estimate (100 keV ions) is 1 meter/ μ sec. This observation motivated us to study transient sheath dynamics using the 2-dimensional Gilbert code. These results, with a videotape showing particle and sheath dynamics, were presented at the SPEAR II review held at Chandler, Arizona, March 14, 1990.

4.1 PHYSICAL AND COMPUTATIONAL PARAMETERS

The parameters for this calculation are shown in Table 4.1.

Table 4.1 Parameters for transient sheath calculation.

Sphere radius	0.3 m
Boundary radius	10 m
Sphere potential	$-10^5 (1 - e^{-V/1.5 \times 10^{-6}})$
Plasma density	10^{11} m^{-3}
Plasma temperature	0.1 eV
Debye length	.00743 m
Ion species	O ⁺
Ion thermal current	$4.94 \times 10^{-6} \text{ A}\cdot\text{m}^{-2}$
Timestep	$2.5 \times 10^{-8} \text{ sec}$

The calculation was done for a 0.3-meter sphere in a 10-meter boundary. Plasma conditions were appropriate to the SPEAR II flight. The voltage risetime was chosen to be appropriate to the 3 and 10 μ sec SPEAR II pulses. The equilibrium (Langmuir-Blodgett) solution to this problem is a sheath radius of 15 meters and a current of 14 milliamperes.

The calculation was started with ion macroparticles representative of a uniform charge density. Electrons were taken to be barometric for negative potentials

and to increase linearly for positive potentials. No "charge stabilization" was used. Because of the nonlinear charge density, several potential iterations were needed for each 0.025 μsec timestep during the early parts of the calculation, during which the applied potential was rising rapidly. The ion charge absorbed by the sphere was accumulated, allowing the current as a function of time to be deduced. The sheath radius was determined by periodic visual inspection of the potential plots.

4.2 RESULTS AND DISCUSSION

The results of the calculation (current and sheath radius vs. time) are shown in table 4.2. The sheath expands rapidly to four meters as the potential is applied, then grows slowly due to erosion. The current peaks at about 15 μsec at a value 10 times the equilibrium current, and then drops slowly thereafter.

Table 4.2 Results of the transient sheath calculation.

Time [μsec]	Potential [kV]	Current [mA]	Sheath Radius [m]
0.5	-28	4	1.5
1.0	-49	8	2.4
1.5	-63	3	3.2
2.0	-74	18	3.5
2.5	-81	24	3.6
3.5	-90	35	3.7
4.5	-95	48	3.8
5.5	-97	60	4.0
7.5	-99	83	4.1
9.5	-100	100	4.2
11.5	-100	117	4.2
13.5	-100	130	4.2
15	-100	140	4.3
20	-100	135	
25	-100	128	
30	-100	110	4.7
∞	-100	14	15

The 4-meter sheath radius can be estimated by equating the charge in the sheath to the Laplacian charge on the probe:

$$Q \sim 4\pi R^3/3 Ne \sim 4\pi \epsilon_0 r V$$

which gives a sheath radius of 3.7 meters. The current can be estimated as the large sheath limit of the Langmuir-Blodgett cold cathode current between two concentric spheres:

$$I = 0.8551 (4\pi\epsilon_0) (32e/81m)^{1/2} V^{3/2} (r/R)^{3/2}$$

which gives 95 mA for the parameters of this problem. As this is far greater than the plasma thermal current to the sheath surface (1 mA), the sheath expands by plasma erosion. Equating the current to the erosion rate gives an expansion rate of about 3 cm/ μ sec. Other scaling relations can also be defined. We predict a time of about 0.01 seconds to expand to an equilibrium sheath.

4.3 DYNAPAC SIMULATION

To demonstrate the capability of performing a dynamic particle-tracking calculation, we used DynaPAC to calculate in three dimensions the Gilbert result for transient current collection by a 1-foot radius sphere biased to -100 kV. The procedure was:

1. Initial ions were placed in the grid to mimic a uniform density of 10^{11} m^{-3} .
2. The potential was initialized at a time appropriate to the sphere potential at 0.5 μ sec using barometric electrons.
3. A particle pushing timestep of 0.5 μ sec was taken.
4. The sphere potential was advanced 0.5 μ sec, and one major potential iteration performed. The -100 V contour is taken as the "sheath" radius.
5. Return to 3.

Figure 4.1 shows the initial potentials with -28 kV on the sphere. The diamond-shaped zero contour is an artifact; contours are rounded down to the -10 V

contour at 3.0 meters. Analytically, we estimate the sheath radius to be a bit over 2.4 meters, which is the location of the -100 V contour.

Figure 4.2 shows a cut of the ion positions after the first 0.5 μ sec push. Note that a uniform ion density requires a slightly nonuniform ion spacing.

Figure 4.3 shows the second set of potentials. The sphere is at -49 kV, and the -10 V contour has moved to 3.5 meter radius. Figure 4.4 shows the second set of ion positions, indicating visible ion movement at up to 1-meter radius.

Figure 4.5 shows the contours at 3.5 μ sec. The 10 V contour has now entered the coarsest (2-meter resolution) grid. The corresponding ion positions are shown in figure 4.6. Note how much less the ions from the corners of the fine grid have moved than the ions from the nearest grid boundary. The sphere is now beginning to collect ions from the 0.5 meter resolution grid.

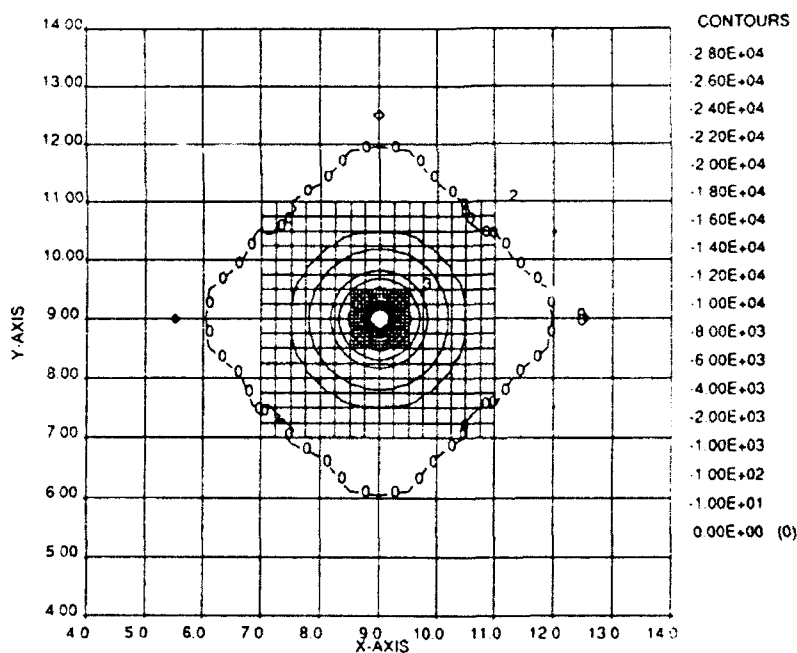


Figure 4.1 Potentials around sphere at 0.5 μ sec.

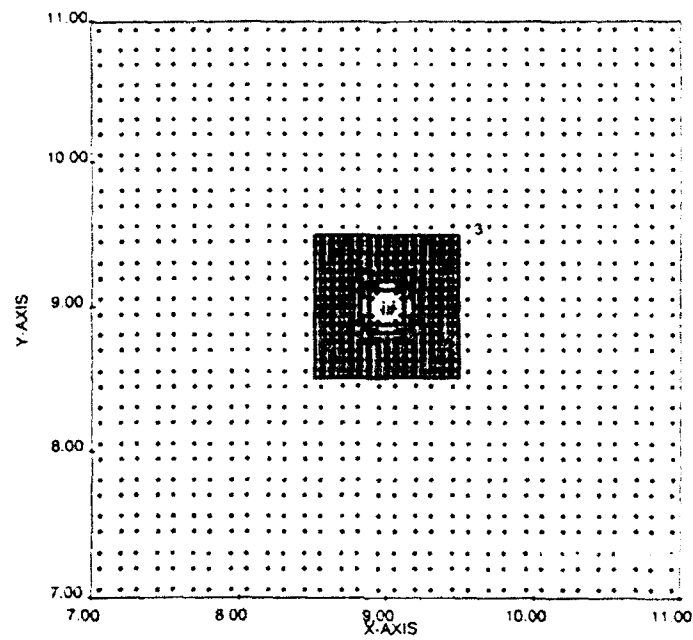


Figure 4.2 Particle positions after the first 0.5 μsec push.

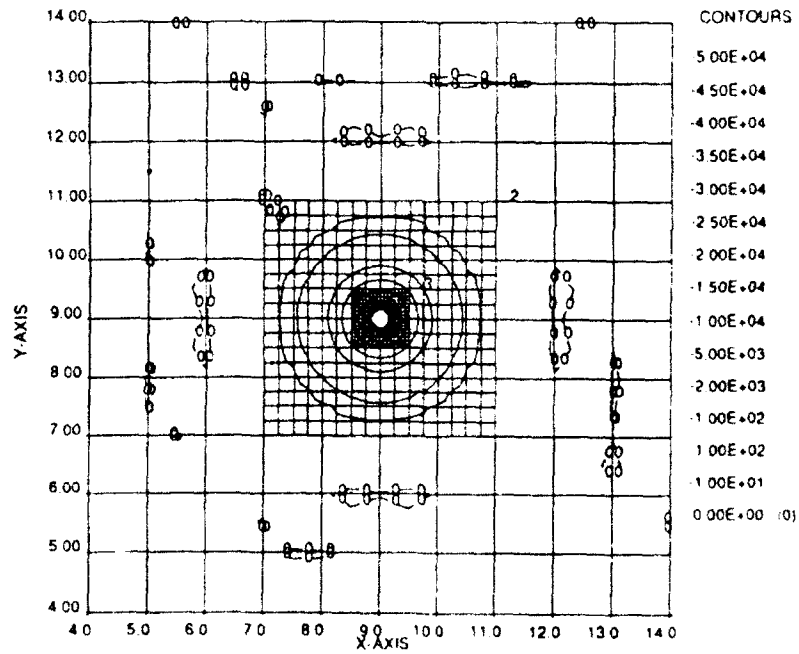


Figure 4.3 Potentials around sphere at 1.0 μsec .

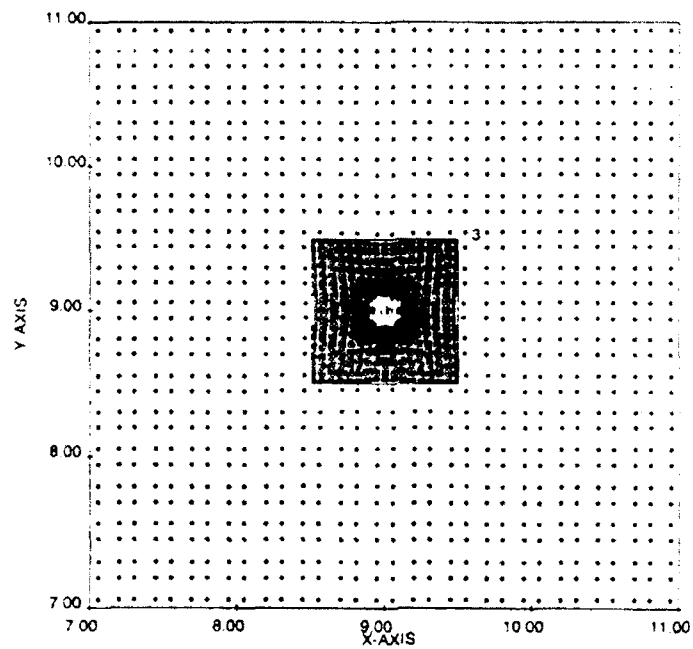


Figure 4.4 Particle positions after 1.0 μsec.

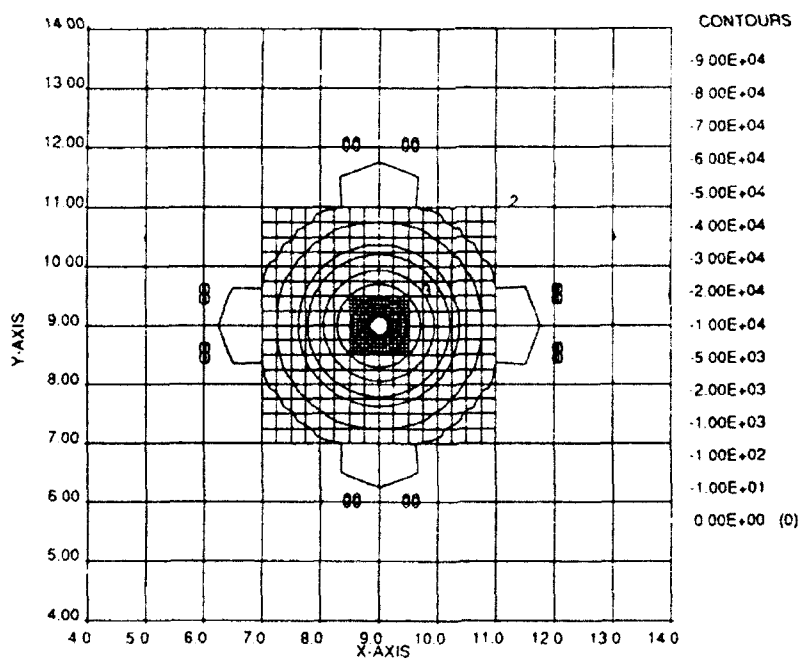


Figure 4.5 Potentials around sphere at 3.5 μsec.

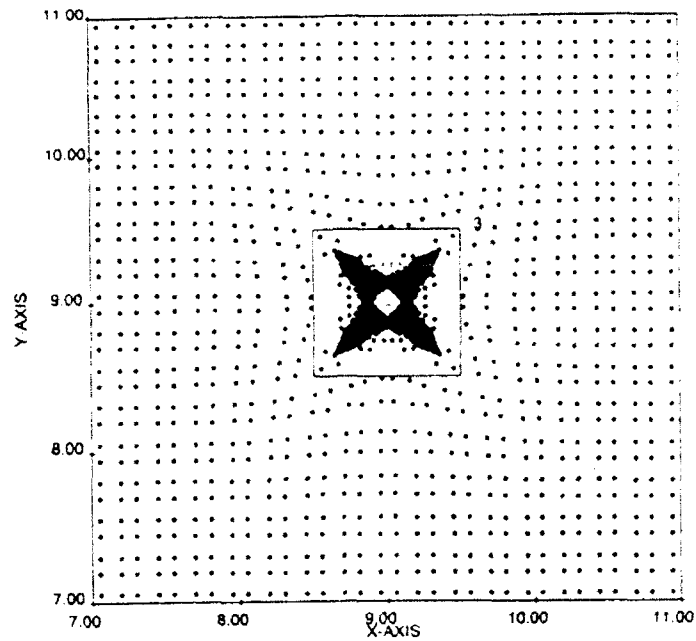


Figure 4.6 Particle positions after 3.5 μ sec.

Figures 4.7 through 4.10 show potentials and particle positions at 9.5 and 15 μ sec. Ions that originated just inside 3 meters are just entering the innermost grid at 15 μ sec.

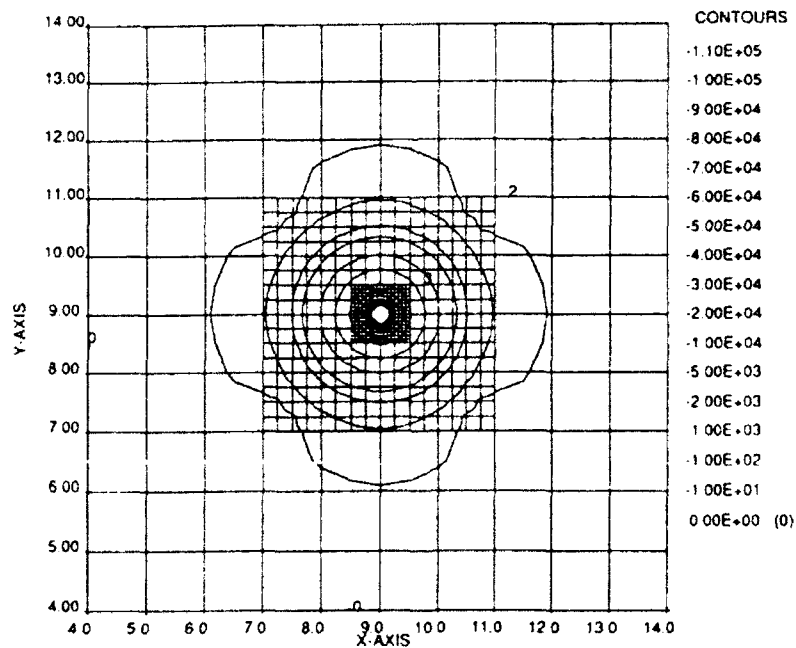


Figure 4.7 Potentials around sphere at 9.5 μ sec.

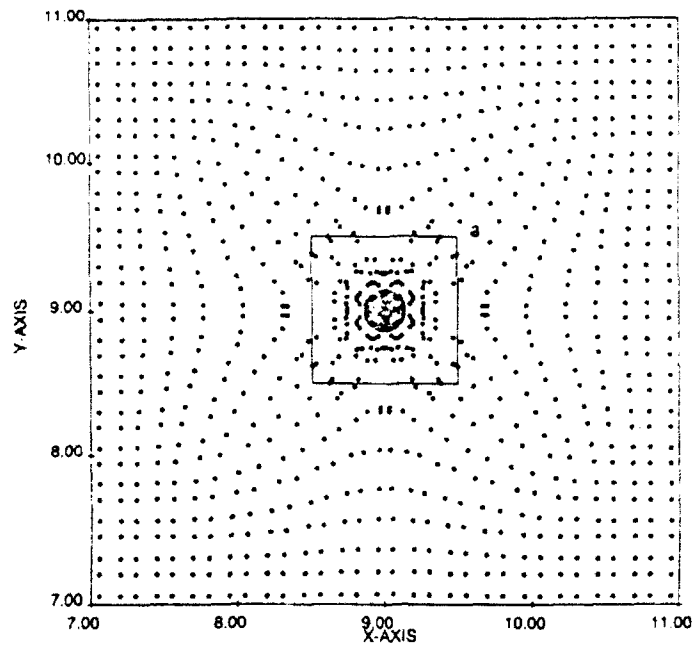


Figure 4.8 Particle positions after 9.5 μ sec.

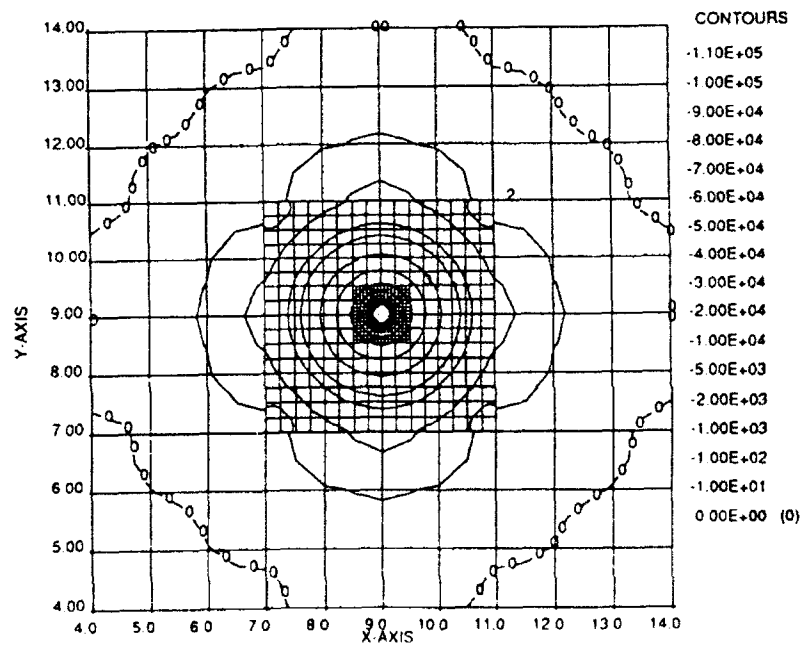


Figure 4.9 Potentials around sphere at 15 μ sec.

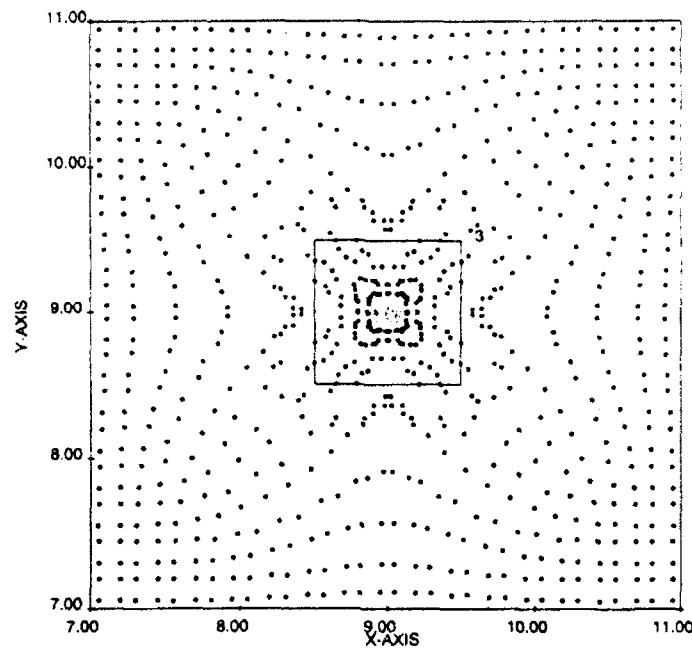


Figure 4.10 Particle positions after 15 μ sec.

Table 4.1 shows the DynaPAC results in comparison with the Gilbert results. DynaPAC shows a somewhat faster rise in current to a somewhat *higher peak* value. Also, the sheath radius is somewhat smaller. This is consistent, as a smaller sheath leads to higher electric fields. A possible reason for the difference between Gilbert and DynaPAC is that the DynaPAC potentials were not fully converged at each timestep. The total charge collected in the DynaPAC calculation corresponds to the charge in a 2.75 meter radius spherical region, which is consistent with the final particle positions (figure 4.10).

Table 4.3

Time (μ sec)	Potential (kV)	Current (mA)		Sheath radius (m)	
		Gilbert	DynaPac	Gilbert	DynaPAC
0.5	-28	4	.2	1.5	2.4
1.0	-49	8	5.4	2.4	2.8
1.5	-63	13	15.4	3.2	3.2
2.0	-74	18	23.3	3.5	3.3
2.5	-81	24	31.8	3.6	3.4
3.0	-86		40.9		
3.5	-90	35	44.6	3.7	3.5
4.0	-93		71.3		
4.5	-95	48	87.3	3.8	3.6
5.0	-96		38.8		
5.5	-97	60	90.7	4.0	3.7
6.0	-98		98.1		
6.5	-99		96.6		
7.0	-99		108.1		
7.5	-99	83	96.1	4.1	3.8
8.0	-100		133.7		
8.5	-100		122.7		
9.0	-100		72.1		
9.5	-100	100	152.2	4.2	3.9
10.0	-100		148.2		
10.5	-100		132.2		
11.0	-100		96.1		
11.5	-100	117	156.2	4.2	4.0*
12.0	-100		136.2		
12.5	-100		126.2		
13.0	-100		138.2		
13.5	-100	130	120.2	4.2	4.1**
14.0	-100		156.2		
14.5	-100		184.2		
15.0	-100	140	68.1	4.3	4.2
20.0	-100	135			
25.0	-100	128			
30.0	-100	110		4.7	
Inf	-100	14		15	

* the sheath begins to move to grid 1, a lower resolution grid.

** taking sheath contour in grid 2.

5. APPLICATION TO SPEAR-II

This work appeared in the Interim Report (30 September 1990) for this contract. The predictions were presented immediately prior to the SPEAR-II chamber tests.

5. APPLICATION TO SPEAR II

During SPEAR II development, the NASCAP/LEO code was used to calculate the equilibrium sheath structure and currents to the payload. The equilibrium sheath was relatively large, and currents were focussed on the high-voltage probe. It was not anticipated that the currents calculated by the equilibrium code would have any noticeable effect.

Later, a "frozen ion" approximation was put into NASCAP/LEO. This showed that the transient sheath would be far smaller than the equilibrium sheath. However, it was not known what the implication of this would be for the currents to the payload.

Calculations summarized in the previous section indicated that transient currents could exceed equilibrium currents by an order of magnitude. Prior to the ground test, the sphere results were scaled to SPEAR II, using the sheath size calculated with the "frozen ion" approximation. These scaled results suggested that the current to the high-voltage probe would be sufficient to disturb the probe reading. The ground test results clearly indicated that the high-voltage probe, which functioned well in vacuum, was unable to measure the transformer secondary voltage in the presence of the laboratory plasma. DynaPAC calculations currently under way give the time-dependent incident ion currents to the various payload components.

5.1 SCALING SPHERE RESULTS TO SPEAR II

(These results were presented at Plum Brook on June 17, 1990.)

Table 5.1 shows scaling of the transient sheath results to predict peak current collected by the SPEAR II high-voltage probe. The SPEAR II equilibrium and transient sheath radii were inferred from calculations using the static plasma interactions code NASCAP/LEO with the default and "frozen ion" space-charge

formulations. The SPEAR II currents were estimated from the observation that the peak current occurred at twice the "transit time" and had a value of one-fourth the sheath charge. The results suggest that in the laboratory the probe will collect 0.1 amperes of incident ion current. The total plasma current to the probe will be about one ampere due to secondary electron emission. Since the nominal circuit current through the probe is 0.1 ampere, this will cause the probe reading to be in error.

Table 5.1 Estimated peak currents to the SPEAR II high-voltage probe.

	Sphere	Flight	Lab
Density	1×10^{11}	1×10^{11}	1×10^{12}
Equilibrium sheath radius	15 m	2.3 m	1.8 m
Equilibrium current	0.014 A	0.0016 A	0.010 A
Transient sheath radius	4 m	1.3 m	1.0 m
Transit time $(2R mR/eV)^{1/2}$	7.5 μ sec	2.4 μ sec	1.6 μ sec
Sheath charge	4.3 μ coul	0.15 μ coul	0.7 μ coul
$Q/4\tau$	0.14 A	0.015 A	0.1 A

5.2 PLUM BROOK RESULTS

The SPEAR II ground test at Plum Brook demonstrated that the high-voltage components could be conditioned and operated both in vacuum and with plasma present. The plasma density was about 10^{12} m^{-3} , under which condition we predicted that the high-voltage probe would collect about an ampere of plasma current (assuming a secondary electron yield of about 10) and that its reading would be perturbed.

Figures 5.1 and 5.2 show the circuit diagnostics, without and with plasma, for clean 80 kV, 50 μ sec pulses. It can be seen that all diagnostics are the same except for the curve labeled "transformer secondary current," which is actually (proportional to) the current flowing through the low-voltage portion of the probe. The plasma causes the probe current to drop to about a quarter of its vacuum value, recovering somewhat toward the end of the pulse.

The probe consists of ten 0.1 M Ω resistors in series. If -100 kV is applied to the negative end, and plasma current I is injected into the node one resistor away

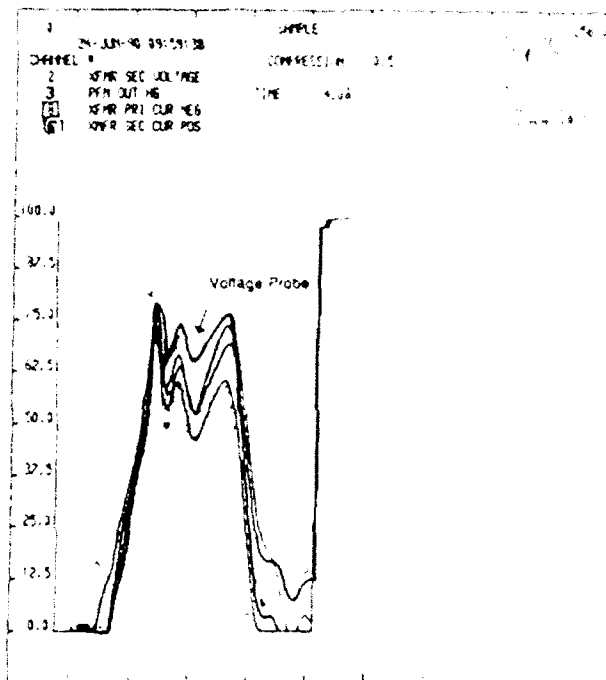


Figure 5.1 SPEAR II voltage probe response (upper curve) in vacuum.

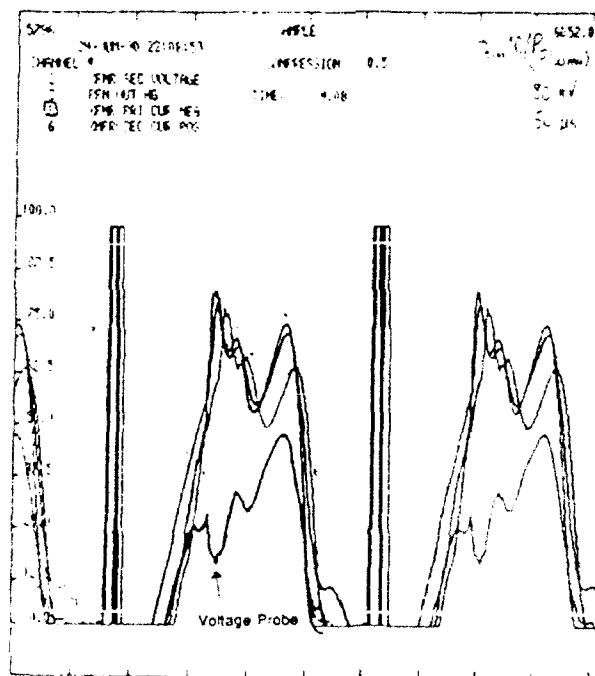


Figure 5.2 SPEAR II voltage probe response (lower curve) in plasma.

from the negative end, the current through the remainder of the probe is $0.1(1-I)$ amperes. Thus an injected plasma current of a sensible fraction of an ampere will cause the probe reading to be very low, as is seen in the experimental results. Had the plasma density been an order of magnitude less, as might have been expected in flight, the probe reading would have been less severely affected, perhaps dropping on the order of 20 percent.

6. CALCULATION OF CURRENTS TO SPEAR II

This work appeared in the Quarterly Report for 1 October through 31 December 1990. It was subsequently presented at the High Voltage Workshop, Port Hueneme, CA, 19-21 March, 1991.

Note that these calculations proceeded at a rate of one one-microsecond timestep per day on a Sun Microsystems SPARCStation I. Subsequent DynaPAC recoding led to at least a factor of three speed increase, and transfer to an SGI Iris Indigo to another factor of three. Were we to repeat the calculation, we should be able to do several timesteps per day.

6. CALCULATION OF CURRENTS TO SPEAR II

DynaPAC was successfully used to calculate time-dependent currents to the SPEAR II high-voltage components under ground test conditions. The plasma was specified as an Ar^+ plasma of density 10^{12} m^{-3} . The pulse shape, intended to represent a SPEAR II 50 μsec pulse, was given by

$$V(t) = -1.26 \times 10^5 [1 - \exp(-t/3 \times 10^{-6})] \exp(-t/50 \times 10^{-6})$$

This voltage function has a peak of -100 kV at about 9 microseconds.

The calculation was carried out in timesteps of one microsecond, with each timestep consisting of a particle pushing operation followed by a potential solution. On a SPARCstation 1, the calculation proceeded at a rate of about one timestep per day, with about 20 percent of the time devoted to particle pushing and 80 percent to potential solving.

Figure 6.1 shows the ion current incident on the various components. The klystrode battery-pack and the transformer (which are electrostatically well-shielded by struts and bulkheads) have peak currents of about 12 milliamperes, each occurring about 6 microseconds into the pulse. The current to the high-voltage probe (which influences a larger volume of plasma) rises to a peak exceeding 30 milliamperes at about 12 microseconds. The total current (which includes current to the high-voltage leads) peaks around 55 milliamperes at about 8 microseconds. All currents fall off slowly after reaching their peak values. For comparison, an equilibrium calculation for these conditions gives a total payload current of about 6 milliamperes.

Figure 6.2 shows the sheath distance as a function of time. We define the sheath distance to be the distance from the high-voltage end of the probe to the -100 volt contour. During the first 5 microseconds, as the potential is applied, the sheath grows rapidly to its "frozen ion" value of 1.3 meters. During the remainder of the calculation it grows at a slow, constant rate of about 4

centimeters per microsecond. This growth by erosion takes place even though the potential is decreasing slightly during this time.

Figure 6.3 and 6.4 show the potential contours and particle positions at 3 microseconds. This is past the peak currents to the klystrode battery and the transformer, and it can be seen that their confined regions have been depleted of ions. Ions can be seen moving toward the high-voltage probe.

Figure 6.5 and 6.6 show the potential contours and particle position at 9 microseconds. Complex flow patterns are set up as ions travel to the probe from the neighborhood of grounded surfaces such as the top bulkhead, the doors, and the plasma accelerator.

Figure 6.7 and 6.8 show the potential contours and particle positions at 21 microseconds. Most of the current to the probe now consists of particles originating a meter or more from the probe in grid number 2. However, a large number of macroparticles originating in the subdivided regions near the object are still alive. Ions originating in the low-field region at the lower-left corner of grid number 3 remain unmoved.

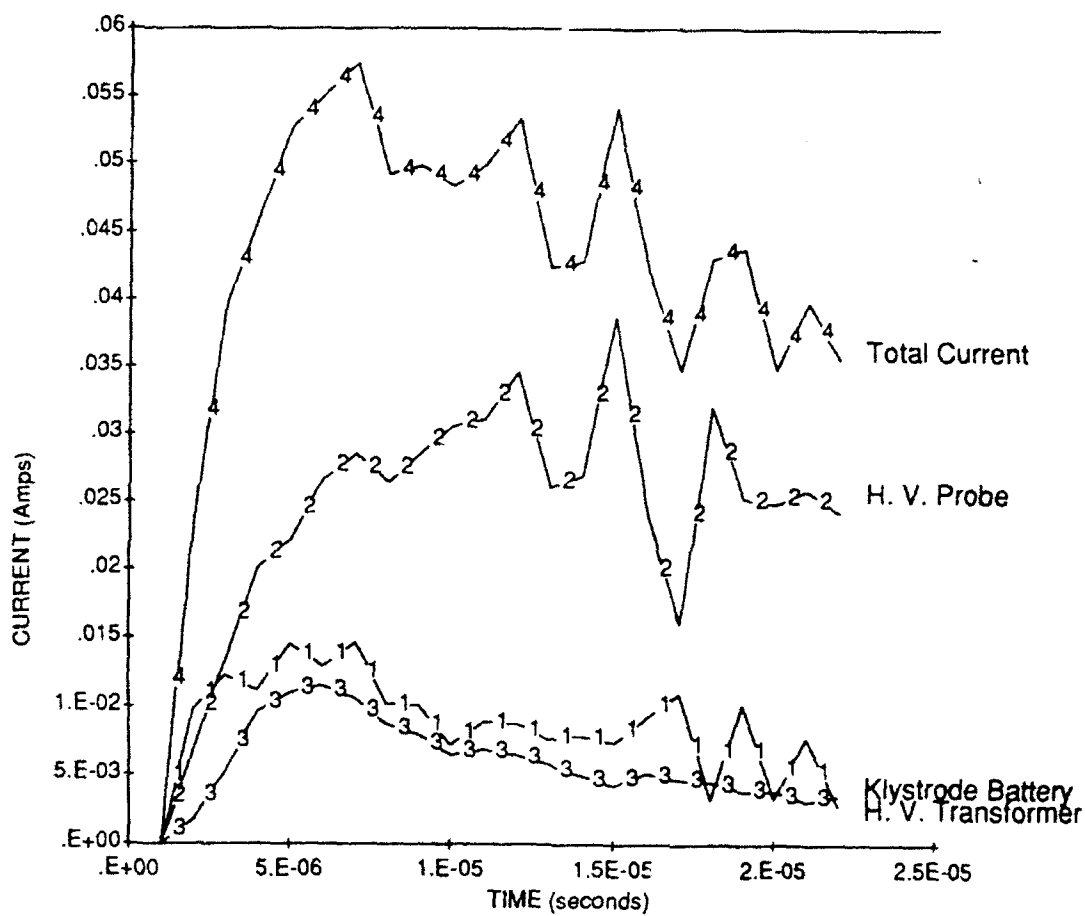


Figure 6.1 Time-dependent ion current incident on the various SPEAR II high-voltage components under laboratory conditions for a 50 μ sec, 100 kV pulse.

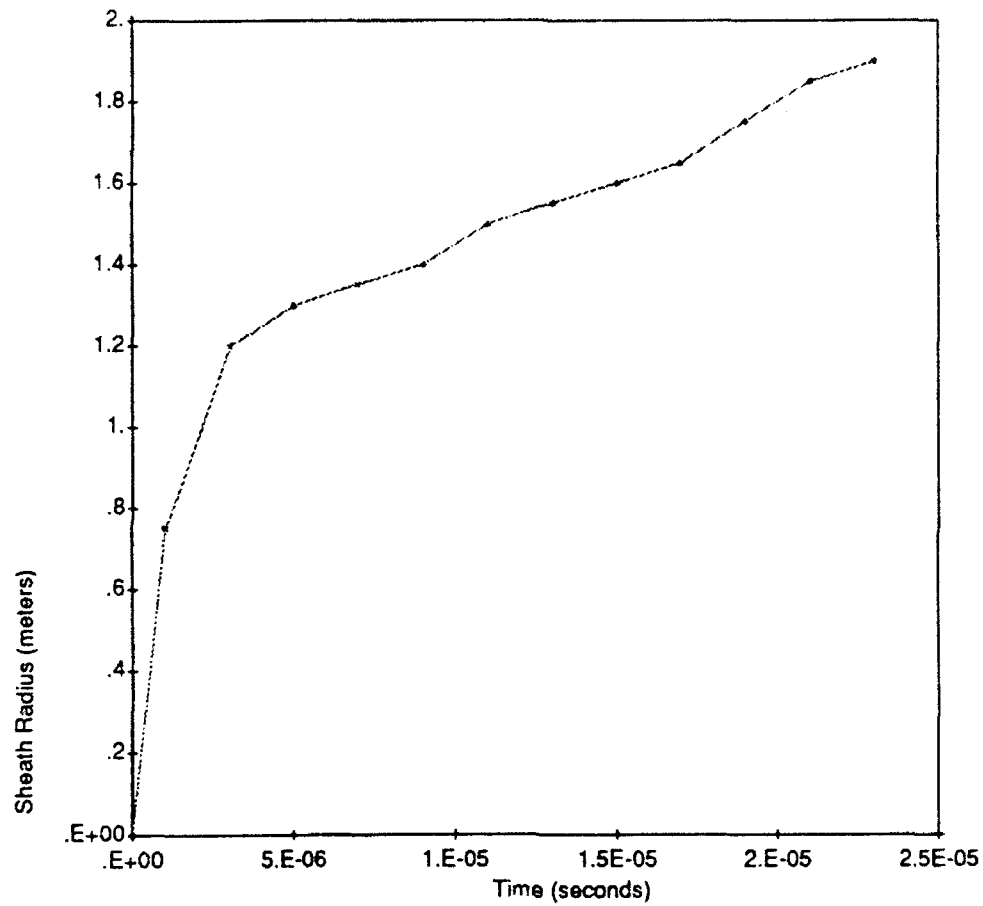


Figure 6.2 Distance of the sheath from the SPEAR II high-voltage probe.

Data Name: POTG Time= 3
 Slice Z = 6.0000
 Mesh Size = 1.0000E+00 meters
 Min= -7.5009E+04 Max= 4.0498E+01

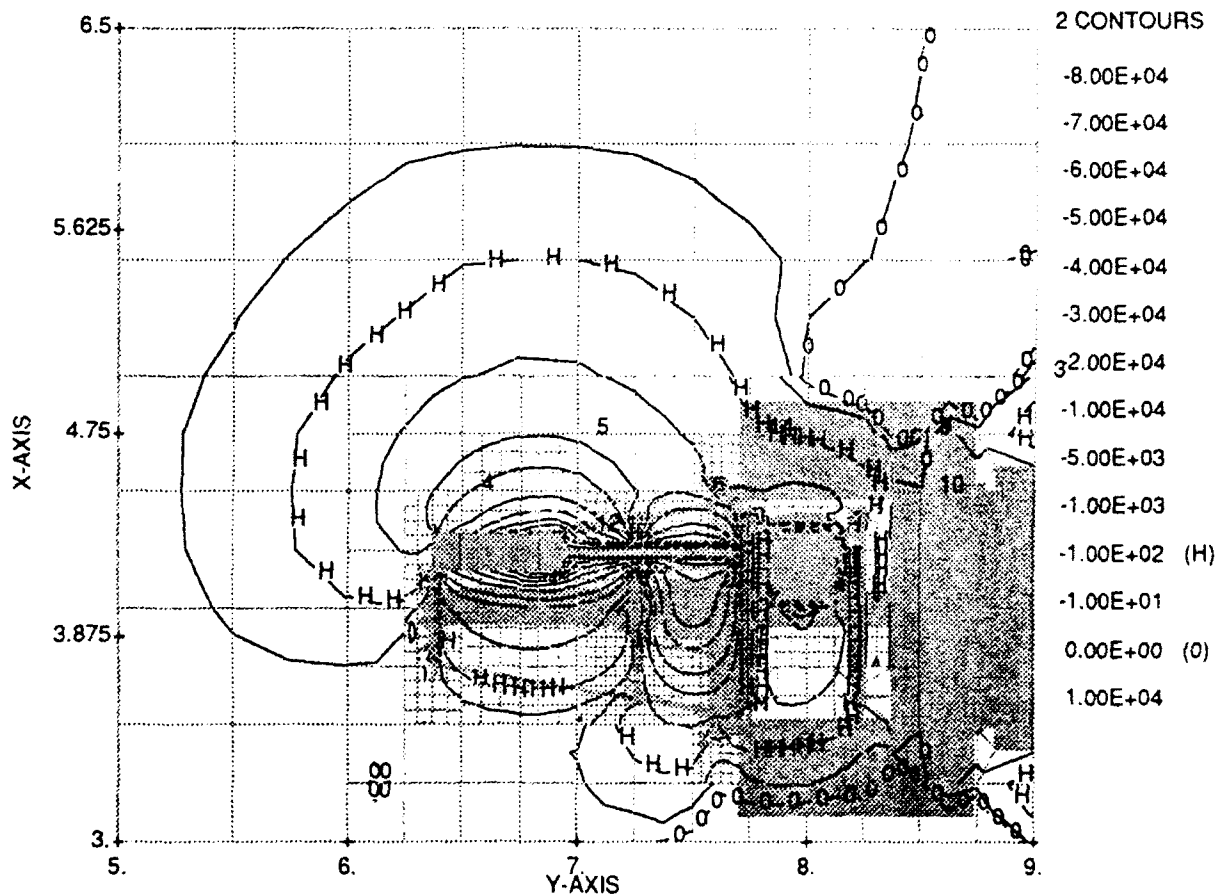


Figure 6.3 Potential contours about SPEAR II 3 μ sec from the beginning of the pulse.

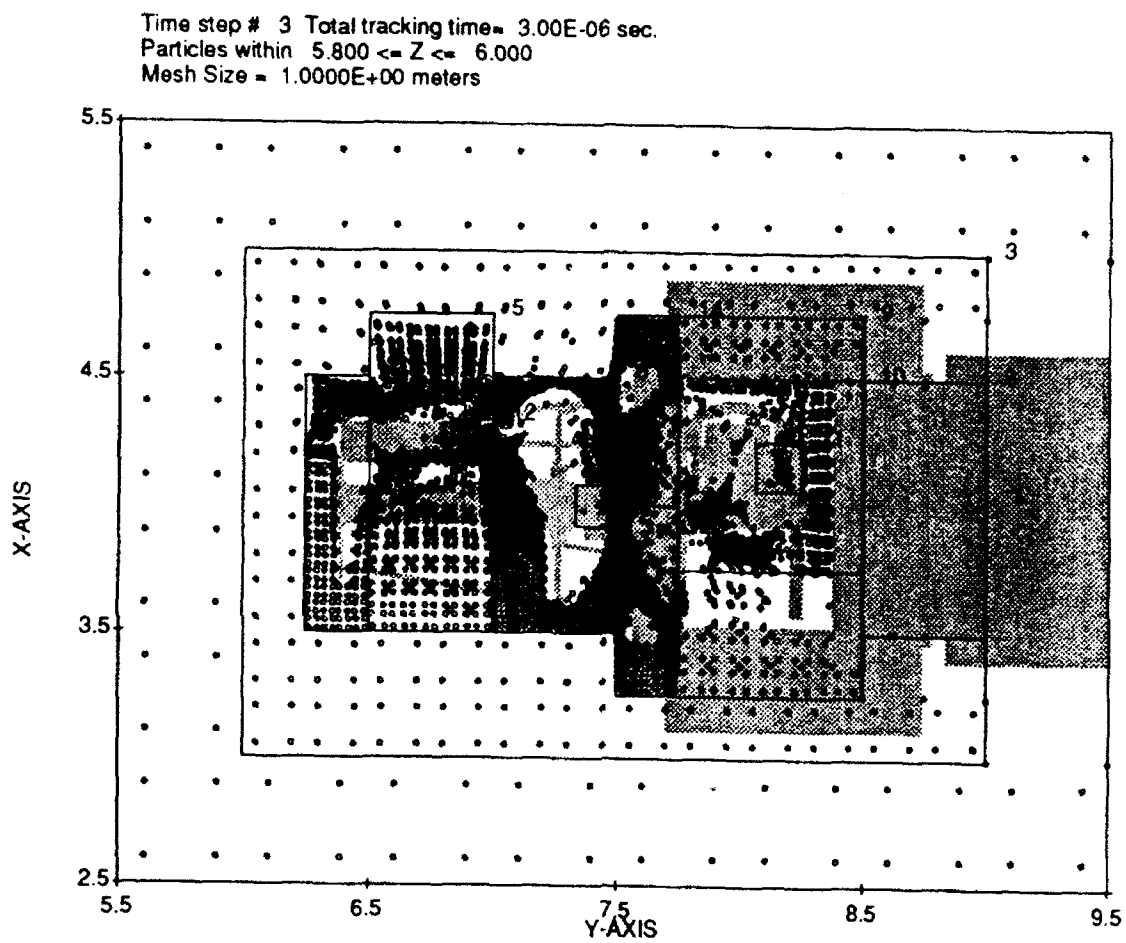


Figure 6.4 Ion macroparticle positions at 3 μ sec.

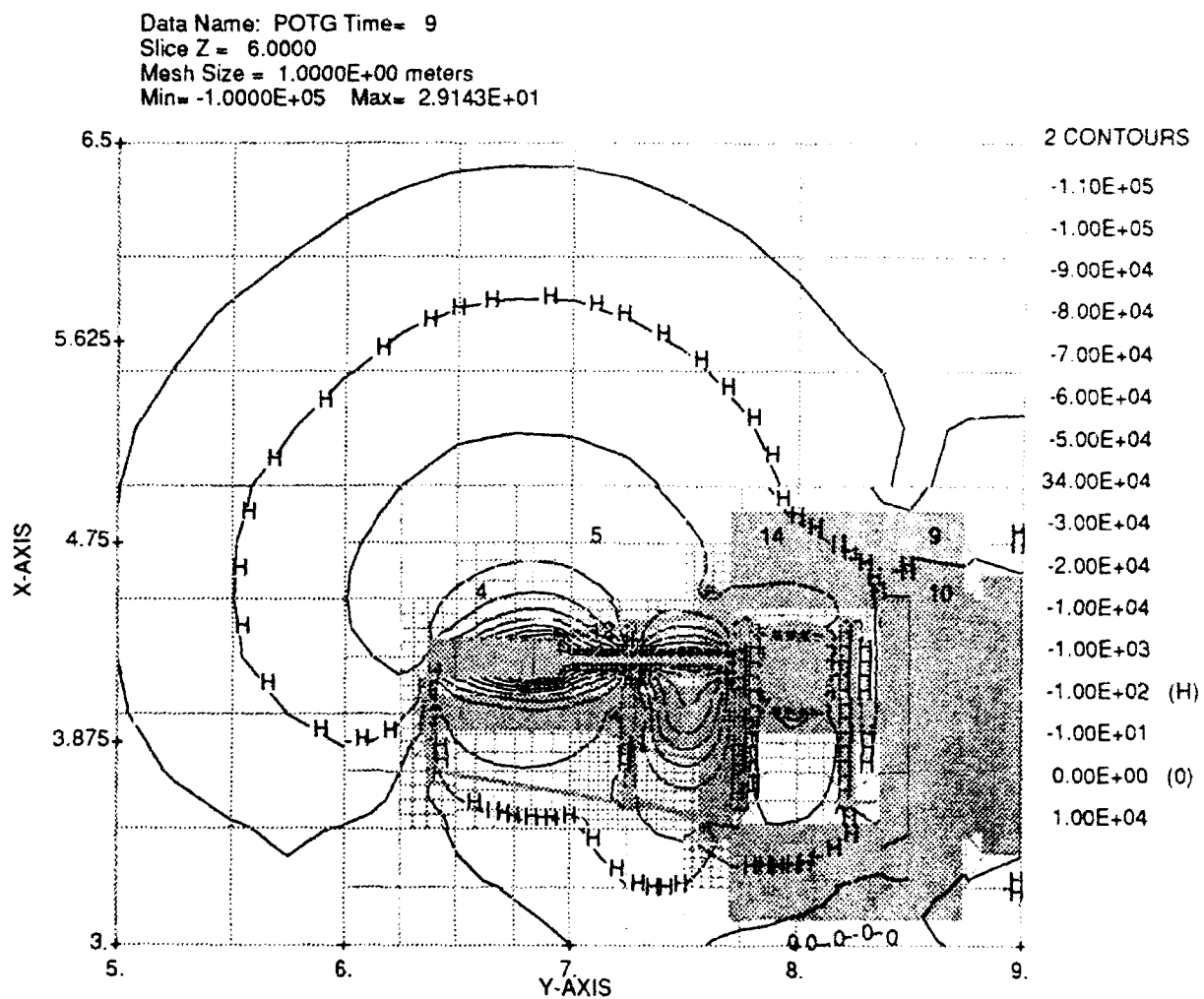


Figure 6.5 Potential contours about SPEAR II 9 μ sec from the beginning of the pulse.

Time step # 9 Total tracking time= 9.00E-06 sec.
Particles within 5.800 <= Z <= 6.000
Mesh Size = 1.0000E+00 meters

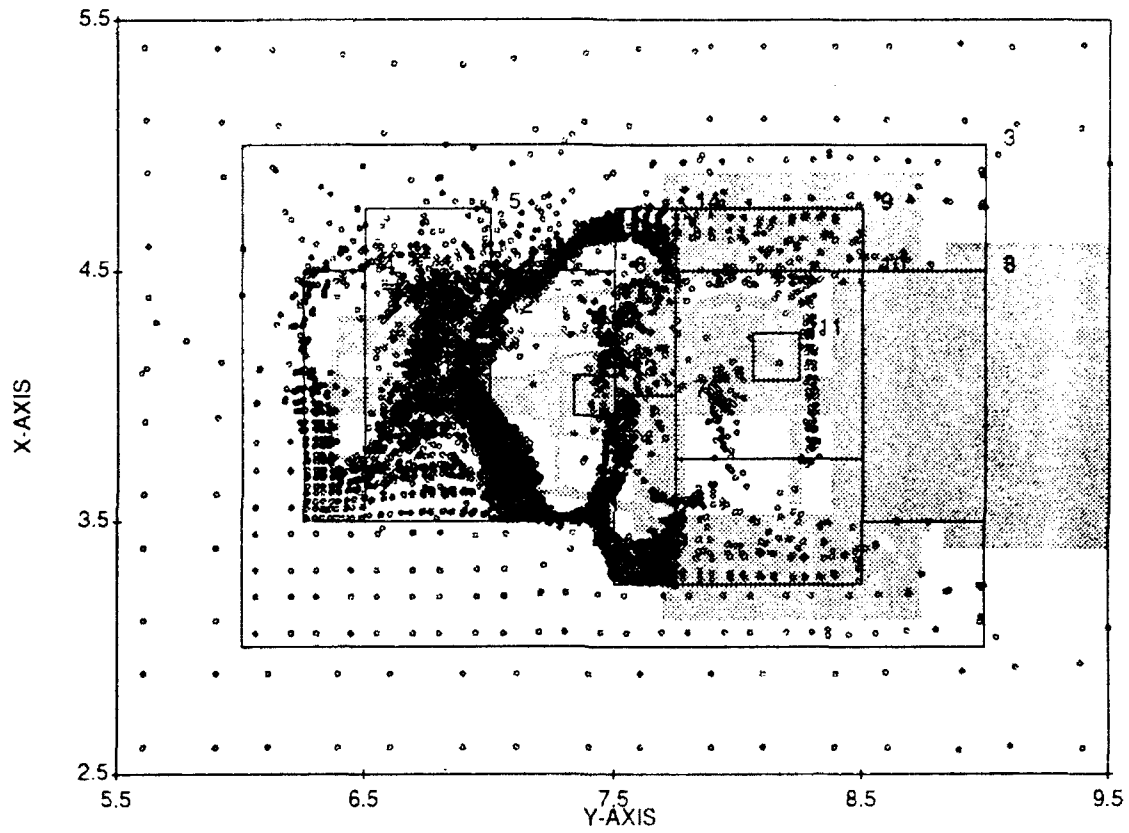


Figure 6.6 Ion macroparticle positions at 9 μsec.

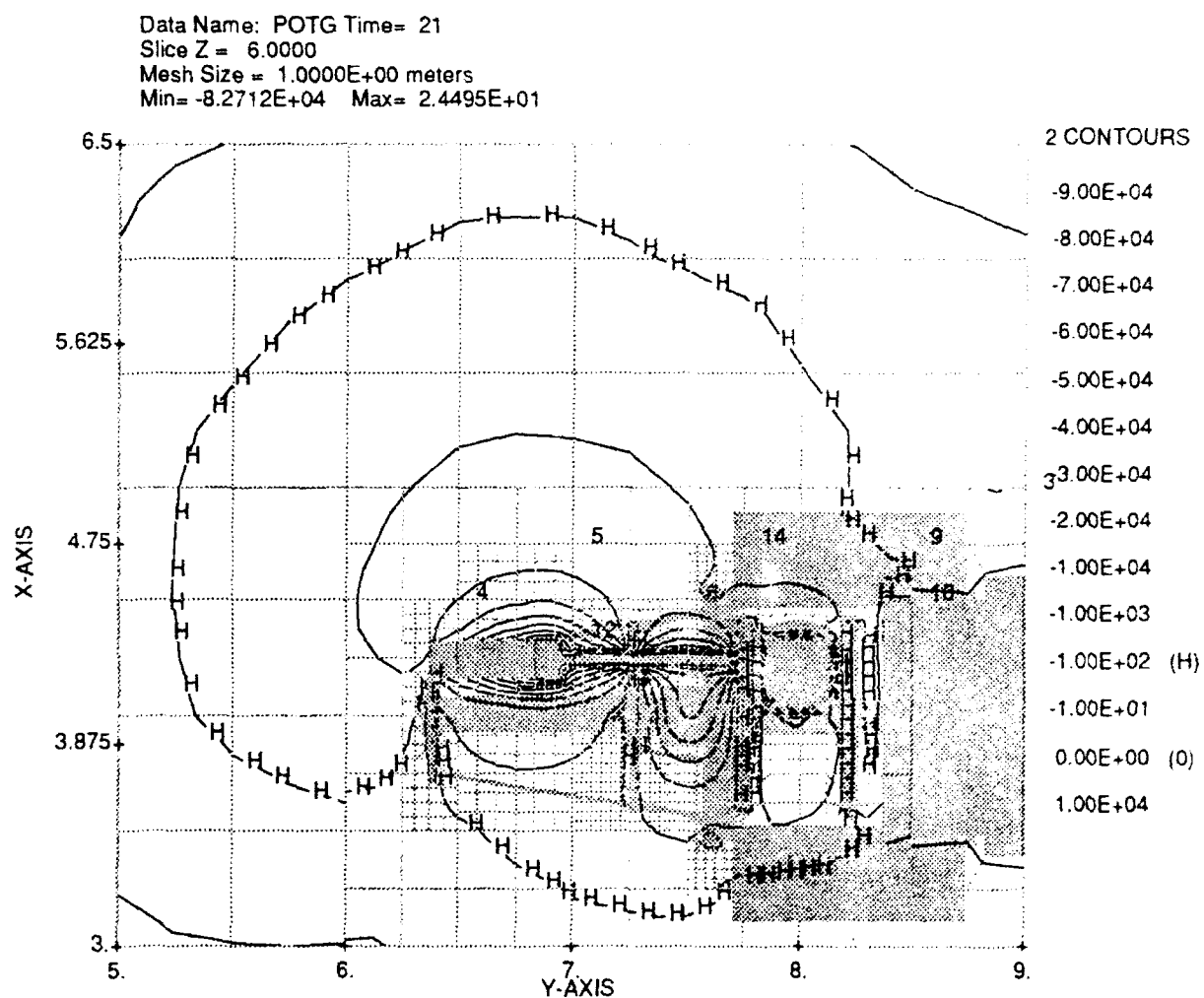


Figure 6.7 Potential contours about SPEAR II 21 μ sec from the beginning of the pulse.

Time step # 21 Total tracking time= 2.10E-05 sec
Particles within 5.800 <= Z <= 6.000
Mesh Size = 1.0000E+00 meters

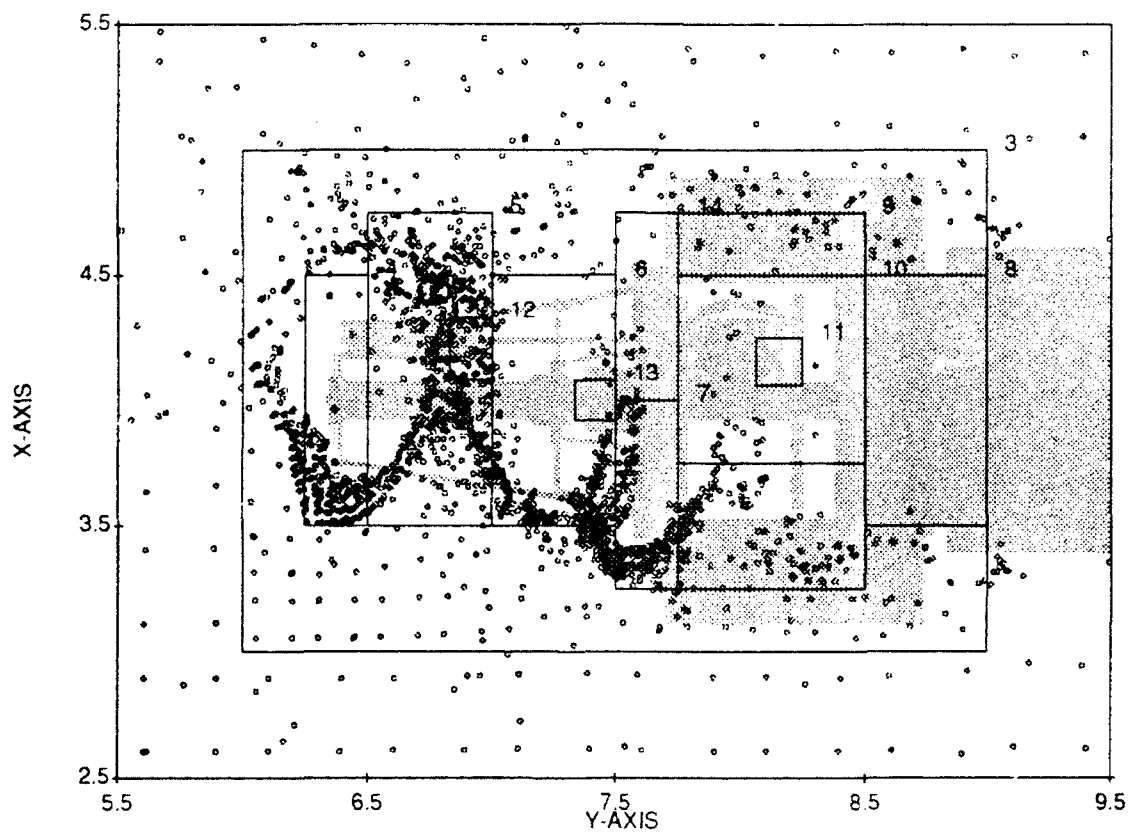


Figure 6.8 Ion macroparticle positions at 21 μsec.

7. SPEAR-II PRODUCTS REPORT

This chapter is the Spring 1992 revision of S-Cubed's contribution to the SPEAR-II Products Report. The final extensive rewriting was performed under contract F19628-91- C-0187, entitled "Space System-Environment Interactions Investigation." The work was also supported by contract DNA001-87-C-0091, entitled "Enhancing Surface Breakdown Strength Components in Space."

An earlier version of this report appeared in the Quarterly Report for 1 January through 31 March 1991.

DEVELOPMENT AND APPLICATION OF PLASMA INTERACTION MODELS FOR REALISTIC HIGH POWER SPACECRAFT

Introduction

Recognizing that an understanding of the ambient plasma interactions with high voltage, pulsed power systems was essential to extending the SPEAR technology to other systems and environments, two existing S-Cubed plasma simulation codes, NASCAP/LEO and Gilbert, were challenged to make SPEAR predictions. Since neither of these codes could perform simulations which were both dynamic and fully three-dimensional, the SPEAR program contributed to the development of the DynaPAC (Dynamic Plasma Analysis Code) code^[1]

NASCAP/LEO is a three-dimensional computer code developed by the NASA/Lewis Research Center^[2] for the study of high-voltage plasma interactions and the design of high voltage systems in LEO. It has been successfully applied to numerous laboratory and spaceflight experiments.^[3,9] NASCAP/LEO was successfully used to predict plasma currents and floating potentials for SPEAR I, whose geometry, while truly three-dimensional, was relatively simple. The SPEAR II mock-up and chamber tests showed, for the first time, that NASCAP/LEO could predict sheath plasma currents for a complicated geometry.

Gilbert is a general-purpose, two-dimensional, plasma and electrostatic analysis code developed internally by S-Cubed. The Gilbert calculations performed for the SPEAR II program provided important quantitative assessments of the validity of space plasma simulations using laboratory chambers. Experiments showed that the computational techniques used in Gilbert were accurate enough to be used in the design of independent components for space-based power systems. Pending development of a 3-D dynamic code, transient-to-equilibrium current scaling relations developed using Gilbert were coupled with NASCAP/LEO sheath calculations in the "equilibrium" and "frozen-ion" approximations to make successful pretest estimates of enhanced transient currents to the SPEAR-II payload.

DynaPAC is a fully three-dimensional, dynamic plasma interaction code, which includes, through models developed and validated as a part of the SPEAR program, much of the knowledge of plasma physics and system/plasma interactions gained during the SPEAR program. The code allows the SPEAR I and II laboratory data to be extended to orbital plasma conditions for systems using different geometries.

Applications

NASCAP/LEO models high voltage/plasma interactions in three dimensions and is CAD/CAM compatible. NASCAP/LEO will be released domestically by NASA/Lewis Research Center in the near future. When released, the code will assist researchers in the study of high voltage spacecraft/plasma interactions and spacecraft designers in the design of high voltage spacecraft

operating in LEO.

Gilbert is a two-dimensional computer code for the modeling of static and dynamic high voltage/plasma interactions. The code assists researchers in the study of high voltage spacecraft/plasma interactions and spacecraft designers in the design of high voltage spacecraft for use in LEO. Under the SPEAR program, the code was applied to (1) simulations of high voltage breakdown experiments performed at Maxwell Laboratories, Inc., (2) modeling of the time-dependent currents to the SPEAR II payload measured in a small space simulation chamber, and (3) modeling of the sheath expansion around and the transient currents to a high voltage sphere.

DynaPAC allows plasma interaction specialists to perform realistic analyses with direct application to engineering problems. Its current capability is illustrated by its application to SPEAR II. In the immediate future, DynaPAC will be used primarily as a development workbench for algorithms and approximations appropriate to different regimes of spacecraft/plasma interactions. Eventually, a version of DynaPAC, containing a selection of validated and documented plasma formulations, will be released for engineering use.

In addition to SPEAR II, many other space experiments and space power system analyses require a three-dimensional, dynamic treatment. Some examples are 1) spacecraft charging by an electron beam at an arbitrary angle to the earth's magnetic field, 2) neutral particle beam charging, 3) beam plasma interactions, 4) beam/surface interactions, 5) ionization instabilities within electron sheaths, and 5) ionization breakdown within ion sheaths including cathode surface effects, to name just a few.

Prior State-of-the-Art

The SPEAR-I laboratory and flight experiments, along with three-dimensional computer modeling, demonstrated the capability to predict steady state interactions between geometrically simple high voltage spacecraft and the space plasma. However, (1) the ability to make calculations for spacecraft which are truly geometrically complex had not been demonstrated, and (2) the time-dependent response of the space plasma to the high fields and voltages associated with pulsed power systems such as SPEAR II, and the associated dynamic spacecraft charging, had not been fully investigated. Processes not adequately modeled include formation of the space charge sheath, current flow in the quasi-neutral pre-sheath, breakdown phenomena, plasma kinetics, ionization processes, and the effect of dynamic processes on spacecraft charging.

These inadequacies became apparent in trying to make plasma interaction predictions for the SPEAR II high voltage system. Equilibrium sheath calculations (e.g., using NASCAP/LEO) gave very different results from sheath calculations using short time approximations. The plasma currents to the high voltage components could therefore not be calculated with confidence. Existing Particle In Cell (PIC) codes had neither the generalized geometry necessary for realistic

systems nor the sophisticated algorithms required to make simulations of the SPEAR II payload possible in a reasonable amount of computer time. Two dimensional dynamic codes, such as Gilbert, could give only a hint of the detailed information needed for the design of complex three-dimensional systems.

Innovative Concepts

NASCAP/LEO is the first code to combine plasma sheath physics with fully CAD/CAM compatible, three-dimensional geometry. Thus, it was the first code with the ability to model a payload with the geometrical complexity of SPEAR II.

A "frozen ion" capability was developed and incorporated into NASCAP/LEO in order to provide estimates of very early time plasma sheath currents. In the frozen ion approximation, the time scales are assumed to be short enough that inertia prevents the ions from moving under the influence of the fields. This was a stop-gap method for calculating time-dependent currents to the SPEAR II payload prior to the development of the DynaPAC code.

The Gilbert code uses grids created with commercial finite element programs (such as PATRAN^[10]). This gives the ability to use grids with variable resolution in order to model processes in detail, where needed, while still modeling extended range interactions. Higher-order finite elements with continuous electric fields and a third-order particle tracking algorithm are used in order to obtain the accuracy needed for time-dependent calculations. The code allows choosing the appropriate plasma description for the problem under consideration. Models based on particle tracking, analytic formulas, and hybrid methods are available. The code is written with advanced programming and numerical techniques to take advantage of modern computational capabilities and to promote ease of use, ease of modification, and data interchange with other codes.

In order to model SPEAR laboratory experiments (described later in this chapter) an internal boundary condition to mimic the presence of a grid (made of ordinary window screen) was developed and incorporated into Gilbert. It was shown that the mean potential of the screen was related to the electric field discontinuity across the screen.

The data from space simulation chamber tests of the SPEAR II payload revealed the importance of transient plasma phenomena to high voltage power systems. DynaPAC, the first three-dimensional, dynamic, plasma interaction code which resolves the complex geometry of realistic systems, was developed as a part of the SPEAR II program. This code was written with advanced programming and numerical techniques to take advantage of modern computational capabilities and to promote ease of use, ease of modification, and data interchange with other codes. A screen-handler utility provides for interactive input file generation. DynaPAC's DataBase Manager is a programmer-friendly way of allocating, storing, and retrieving large blocks of gridded or otherwise structured data. DynaPAC pioneers the use of higher order elements which produce strictly continuous electric fields and potentials. Arbitrarily nested grids accommodate

simulations of complex systems with extended-range plasma interactions. Graphical display is available using a variety of graphics interfaces, including the X-Windows protocol, which allows display from a remote host.

Description of the NASCAP/LEO Steady State Plasma Sheath Code

NASCAP/LEO^[2,4] is a three-dimensional, finite-element code based on a cubic grid structure. For NASCAP/LEO, a spacecraft is defined as a boundary surface element representation using any standard finite element preprocessor. NASCAP/LEO places the spacecraft within a cubical grid structure, and geometrical descriptions and coupling matrices are constructed for cubic zones containing the object surfaces. Local subdivision of the basic grid is used to resolve critical regions, and nested outer grids are used to include a large volume of space.

NASCAP/LEO was used to calculate the plasma current distributions to the SPEAR II payload. Such calculations are based on the concept that a high voltage object in a dense plasma forms a sheath within which the plasma is highly disturbed, and outside of which the plasma is quiescent. All of the computer codes described in this chapter solve Poisson's equation

$$-\epsilon_0 \nabla^2 \phi = \rho \quad (10-1)$$

in various ways, where ϕ is the potential, ϵ_0 is the permittivity of free space, and ρ is the space charge density. In order to achieve short computational times, NASCAP/LEO does not use particle trajectory information to calculate the space charge density appearing in Eq. (10-1). Instead, a nonlinear analytic expression for the charge density as a function of the local potential and electric field, based upon a spherical sheath, is used:

$$\begin{aligned} \rho/\epsilon_0 &= -(\phi/\lambda_D^2)(1 + |\phi/\theta| C(\phi, E))/(1 + (4\pi)^{1/2} |\phi/\theta|^{3/2}) \\ C(\phi, E) &= |\theta/\phi| [(R_{sh}/r)^2 - 1] \\ (R_{sh}/r)^2 &= 2.29 |E \lambda_D / \theta|^{1.262} |\theta/\phi|^{.509} \end{aligned} \quad (10-2)$$

- ρ = space charge [coul-m⁻³]
- ϵ_0 = 8.854x10⁻¹² [farad-m⁻¹]
- λ_D = plasma Debye length [m]
- θ = plasma temperature [eV]
- ϕ = local space potential [volts]
- E = local space electric field [volts-m⁻¹]

The sheath structure is usually spherical where the charge density most greatly influences the potential, so Eq. (10-2) is a good approximation for the LEO environment.

Using Eq. (10-2) for the space charge within the sheath region, together with the appropriate

boundary conditions at surfaces, NASCAP/LEO solves Eq. (10-1) to determine the electrostatic potential about a spacecraft having a highly complex geometry. Knowing the potential field, the sheath boundary can then be identified, and plasma ions and electrons crossing the sheath boundary can be tracked to determine the current distribution on the spacecraft.

Description of the Gilbert 2-D Dynamic Plasma Code

Gilbert is a two-dimensional (R-Z or X-Y) finite element computer code. It solves Poisson's equation (Eq. 10-1) and performs particle generation, tracking, and deposition on a grid whose elements may be linear triangles, bilinear quadrilaterals, and/or biquadratic quadrilaterals. A commercial finite-element preprocessor (such as PATRAN ⁽¹⁰⁾) is used to generate the grid. Sequences of nodes can be specified for use in assigning electrostatic boundary conditions or as current sources. Elements can be specified as empty-space or dielectric filled (with optional conductivity).

The code is highly modular and flexible. Preprocessors are used to interpret the finite element grid input and to generate initial particle distributions. The main analysis routine solves problems either by time-stepping or by iteration on a nonlinear problem. Postprocessors display potential contour plots, particle scatter plots, time history plots, and generate and display particle trajectories.

Description of the DynaPAC Three-Dimensional Dynamic Plasma Code

DynaPAC (Dynamic Plasma Analysis Code) is designed to perform static or dynamic plasma calculations for geometrically complex problems. It is written to take advantage of modern techniques for input generation, problem solution, and visualization. The core modules of DynaPAC allow the user to:

- (1) Define the spacecraft geometry and the structure of the computational space,
- (2) Solve the electrostatic potential about the spacecraft, with flexible boundary conditions on the spacecraft surfaces and a space charge computed either fully by particles, fully analytically, or in a hybrid manner, and
- (3) Generate, track, and otherwise process representative macroparticles of various species in the computational space.

The core modules are designed to have the maximum practical user control and to facilitate the incorporation of new or modified algorithms. Preprocessors are provided to set boundary conditions and generate input files in a modern, screen-oriented way. Similarly, screen-oriented postprocessors are provided for graphical and textual data display.

Spacecraft geometrical definitions are done using standard finite element preprocessors, such as PATRAN^[10]. Among the advantages of this approach are that the geometry can be realistically represented, and that finite element models of a spacecraft, constructed for other purposes, can be adapted for plasma calculations. The computational space around the spacecraft is constructed interactively using the GridTool module. Arbitrarily nested subdivision allows resolution of important object features while including a large amount of space around the spacecraft. A high-order, finite element representation for the electrostatic potential assures that electric fields are strictly continuous throughout space. The electrostatic potential solver uses a conjugate gradient technique to solve for the potentials and fields on the spacecraft surfaces and throughout the surrounding space. Space charge options presently incorporated include Laplacian (appropriate in the absence of plasma), equilibrium sheath (appropriate to timescales of milliseconds or longer), "frozen ions" (appropriate to the submicrosecond stage of a negative transient pulse), "mobile ions - barometric electrons" (appropriate to the SPEAR II case of several microsecond time scale response to a negative pulse), and "full PIC" (appropriate to nanosecond timescales).

Particle tracking is used to study sheath currents, to study particle trajectories, or to generate space charge evolution for dynamic calculations. Macroparticles can be generated at either a "sheath boundary" or throughout all space. Particles are tracked for a specified amount of time, with the time step automatically subdivided at each step of each particle to maintain accuracy. The current to each surface cell of the spacecraft is recorded for further processing.

The strength of DynaPAC lies in the wide range of length scales, time scales, and physical phenomena it can handle. Arbitrarily nested subdivision allows the modeling of small geometrical features within large scale problems (e.g., features a few centimeters in size in sheaths several meters in dimension). By suitable choice of algorithms, a user can model equilibrium problems, problems dynamic on an ion timescale (microseconds), or problems dynamic on an electron timescale (nanoseconds). Trajectories are calculated taking account of user-specified magnetic fields, and it is planned to introduce a procedure to obtain potential and space charge fields consistent with magnetic effects.

Gilbert Application to High Voltage Breakdown Experiments

The SPEAR program supported a series of experiments at Maxwell Laboratories, Inc., to study systematically the influence of a background plasma in promoting the breakdown of representative high voltage fixtures^[11]. Figure 10-1 shows a typical test fixture, consisting of a 1 cm diameter electrode protruding from a 3 cm diameter insulator, which was embedded in a 7 cm diameter ground plate. In vacuum, this fixture would hold off a few kilovolts indefinitely with the center electrode at a negative potential, but in a plasma the insulator surface would flash over in a short time.

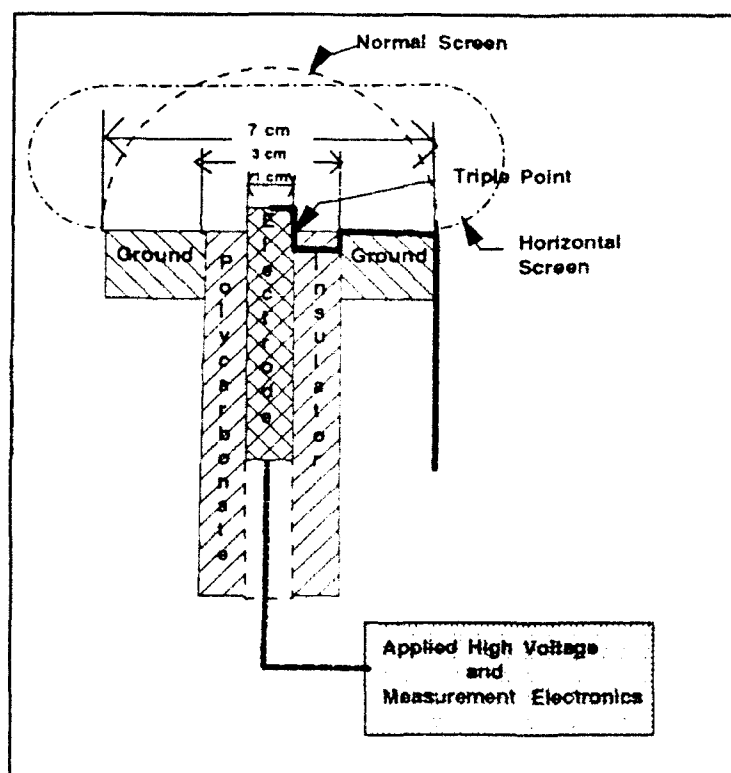


Figure 10-1. Typical axisymmetric test fixture for high voltage breakdown experiments. Two alternative discharge-mitigation screens are shown. The heavy solid line indicates the fixture outline as seen in Figures 10-2 through 10-4.

If the plasma-induced discharge resulted from electric field modification by plasma charge collected on the dielectric surface, we would expect the hold-off time to be inversely proportional to the plasma current. Supposing this to be the case, a hemisphere of ordinary aluminum window screen was mounted on the fixture in order to reduce the total ion current collected. Calculations showed that the screen would reduce the ion current by approximately a factor of five. Experimentally, the screen was found to increase the holdoff time from 30 ms to 30 s at -2.5 kV and from 15 ms to 5 s at -5.0 kV in a background plasma density of $4 \times 10^5 \text{ cm}^{-3}$. This increase in the holdoff time was too great to be explained solely in terms of the total plasma current to the fixture.

Calculations of the plasma ion trajectories, performed with the Gilbert code, were used to attempt to understand this phenomenon. Figure 10-2 shows the trajectories of ions impinging on the original fixture (without the screen). It is apparent that ions impact the entire surface of the fixture, including the sensitive "triple point" area where the insulator contacts the high voltage electrode.

In order to study the ion trajectories in the presence of the screen, it was necessary to develop an internal boundary condition that would mimic the presence of the screen. It was found that the mean potential of the screen was related to the electric field discontinuity across the screen. Figure 10-3 shows the ion trajectories with the "normal" screen present. The ion current is focused onto the top of the center electrode, with no calculable ion current to the triple point. Thus, the effect of the screen was to steer plasma ions away from the triple point, in addition to reducing the total ion current to the fixture.

In order to confirm this finding, a further calculation was performed which showed that if the screen was configured horizontally at its attachment point, then there would be calculable current to the triple point (Figure 10-4). The fixture with the horizontal screen broke down in 40 ms with an applied voltage of -15 kV and a plasma density of $8 \times 10^5 \text{ cm}^{-3}$, compared with 750 ms for the normal screen. Additional calculations and experiments, involving larger fixtures and various screen shapes, showed good correlation between rapid breakdown and the calculated ion current to the triple point. (See Table 10-1.) These studies also illustrated that trying to improve breakdown characteristics by the obvious step of enlarging the insulator may, in fact, promote breakdown by reducing the electrostatic-inertial insulation of the triple point. These results show the utility of accurate two-dimensional potential and trajectory calculations in designing axisymmetric high voltage fixtures for maximum holdoff time.

Gilbert Small Chamber Model for SPEAR II

The SPEAR II payload was first tested with a background plasma in a small vacuum chamber at Maxwell Laboratories, Inc. It was observed that the 10 μs pulses were more likely to cause breakdown than the 3 or 50 μs pulses. This finding motivated a computer simulation using Gilbert of the plasma interactions in the small chamber to determine if plasma dynamic effects might be responsible for this phenomena.

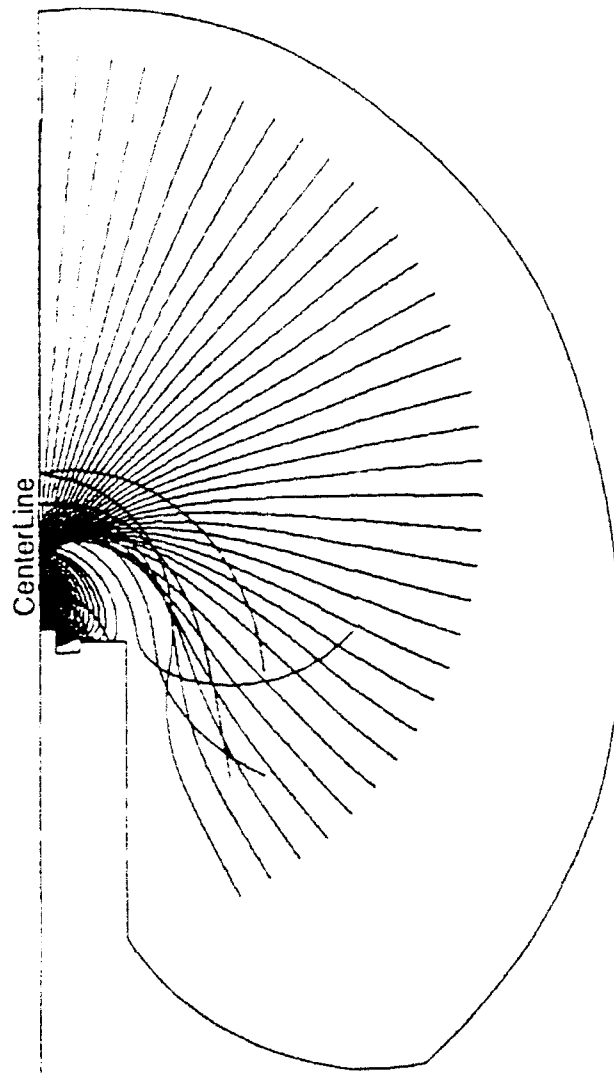


Figure10-2. Ion trajectories to the test fixture without the screen, indicating substantial current to the triple point. (Refer to Figure 10-1 to relate the fixture outline to the actual fixture.)

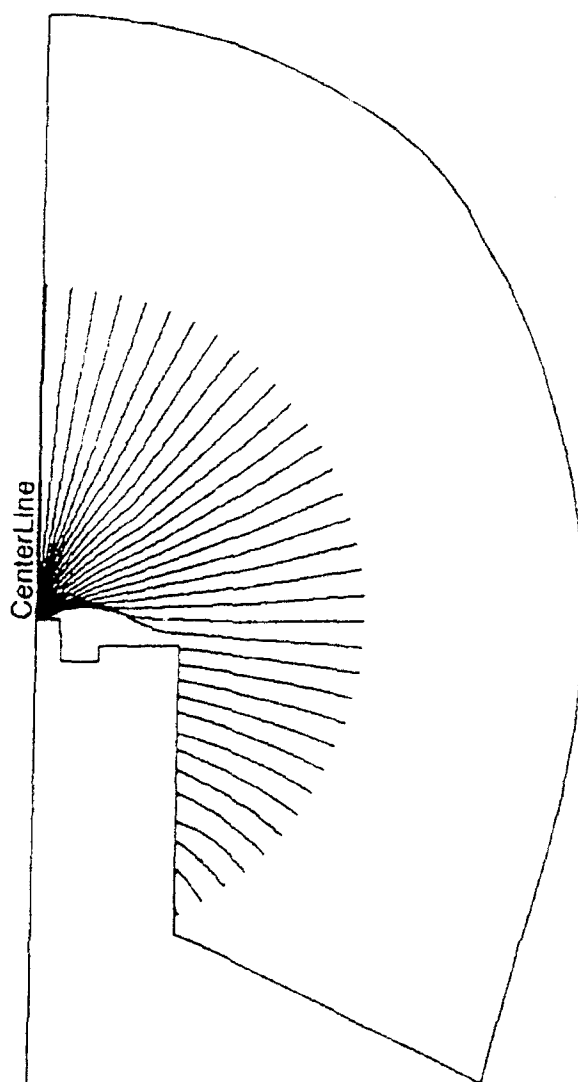


Figure 10-3. Ion trajectories to the test fixture with the normal screen, indicating no calculable current to the triple point. (Refer to Figure 10-1 to relate the fixture outline to the actual fixture.)

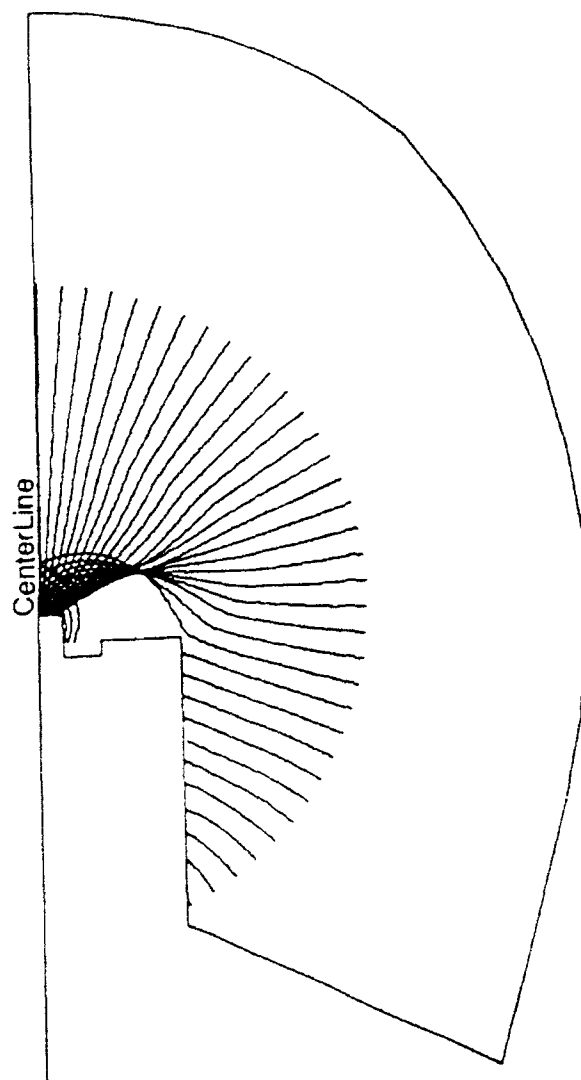


Figure 10-4. Ion trajectories to the test fixture with the horizontally configured screen, showing ions incident on the insulator near the triple point. (Refer to figure 10-1 to relate the fixture outline to the actual fixture.)

Table 10-1. Holdoff time for various insulator widths and screen shapes			
Insulator Width	Applied Voltage	Time to Breakdown	Trajectories to Triple Point
1.0 cm (n)	-15 kV	750 ms	No
1.0 cm (h)	-15 kV	40 ms	Yes
1.0 cm (n)	-50 kV	20 ms	No
2.0 cm (n)	-50 kV	70 ms	No
4.5 cm (l)	-50 kV	7 ms	Yes
4.5 cm (s)	-50 kV	3 ms	Yes

Time to breakdown for fixtures with differing insulator widths. The plasma density was $8 \times 10^5 \text{ cm}^{-3}$. The screen shapes are (n) normal screen (Figure 10-1), (h) horizontal screen (Figure 10-1), (l) "long" screen (not shown), and (s) "short" screen (not shown).

Figure 10-5 shows an artist's concept of the two-dimensional axisymmetric representation of the payload used in the calculation. A grid was constructed to represent the space between the model and chamber walls and ion macroparticles were placed in the grid to represent an initial uniform Ar plasma with a density of $1 \times 10^5 \text{ cm}^{-3}$. The applied voltage on the model was increased with a risetime appropriate to the pulse width under study, and the ions were allowed to move in the resulting fields. Figure 10-6 shows the ion macroparticle positions $4 \mu\text{s}$ into the pulse. The ions are seen to be focused on the high voltage end of the voltage divider, precursive to the results later obtained in three dimensions with DynaPAC. By this time, about half the plasma ions (which initially filled the chamber with a nearly uniform dot pattern) are gone. The chamber will be almost completely drained of plasma ions within about $10 \mu\text{s}$. (The plasma source is not able to replenish the plasma on so short a timescale.)

Figure 10-7 shows the calculated current to the payload for two cases: (1) a risetime of $1.5 \mu\text{s}$ (characterizing the $3 \mu\text{s}$ and $10 \mu\text{s}$ SPEAR II high voltage pulses) and (2) a risetime of $3 \mu\text{s}$ (characterizing the $50 \mu\text{s}$ high voltage pulse). The peak current occurred at about $3 \mu\text{s}$ into the pulse for both cases, but is noticeably higher for the $1.5 \mu\text{s}$ risetime pulse. There is no current beyond $10 \mu\text{s}$, as the chamber is drained of plasma. The suggested interpretation is that:

- (1) The $3 \mu\text{s}$ pulse does not lead to breakdown because the pulse is over when the current peak occurs.
- (2) The $10 \mu\text{s}$ pulse is more likely to cause breakdown than the $50 \mu\text{s}$ pulse due to the higher peak incident ion current.
- (3) Extending the pulse beyond $10 \mu\text{s}$ does not lead to breakdown because there is no further ion current to the payload.

The overall conclusion from these calculations is that a small chamber may produce results unrepresentative of the behavior of a system in a very large chamber or in the ionosphere.

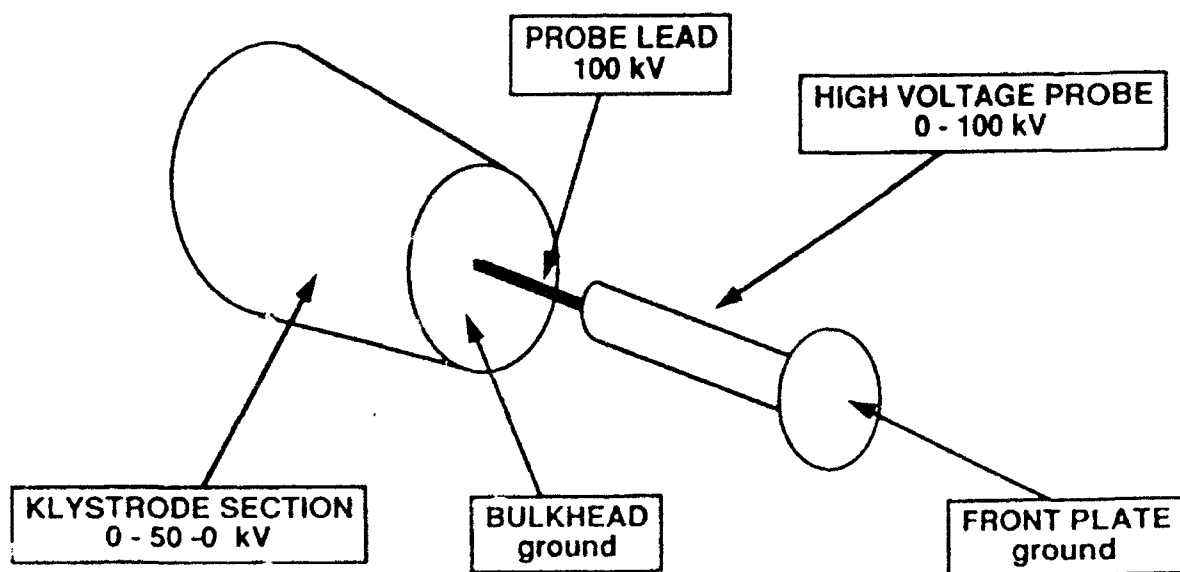


Figure 10-5. Artist's representation of the axisymmetric model of SPEAR II used in the two dimensional plasma dynamic studies. The labels indicate the peak potentials applied to each component: -100 kV on the probe lead, a linear gradient on the high voltage probe from -100 kV at the probe lead to 0 at the front plate, and on the klystron section (representing a cavity partially enclosed by several struts) linear gradients from 0 at either end to -50 kV at the center.

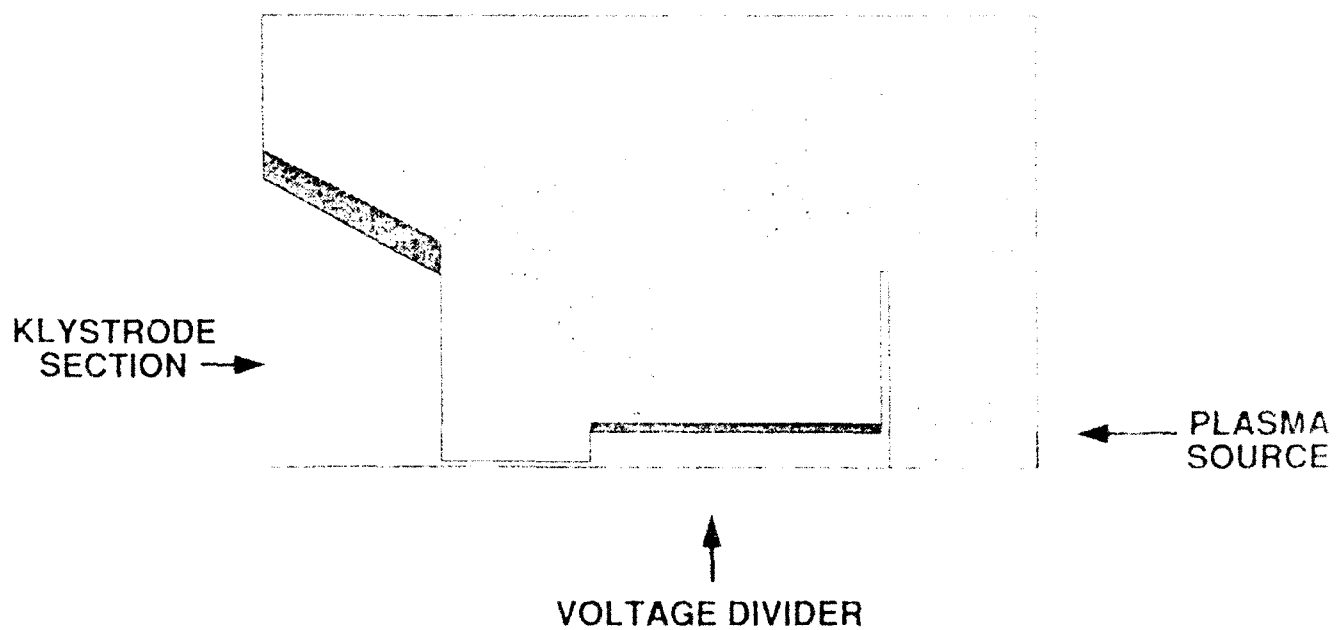
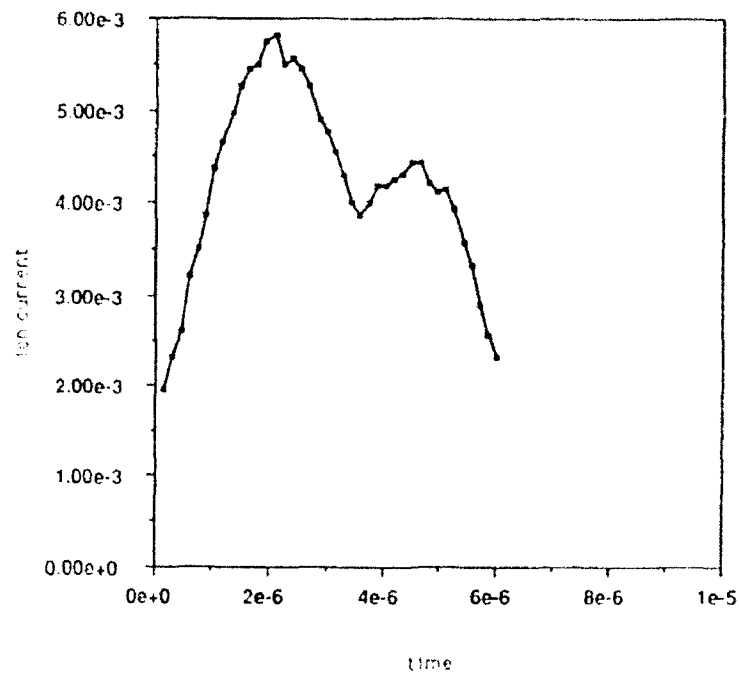


Figure 10-6. Gilbert-calculated ion macroparticle positions $4 \mu\text{s}$ into a SPEAR II high voltage pulse.

1.5 μ s PULSE RISE TIME - 10 μ s PULSE WIDTH



3.0 μ s PULSE RISE TIME - 50 μ s PULSE WIDTH

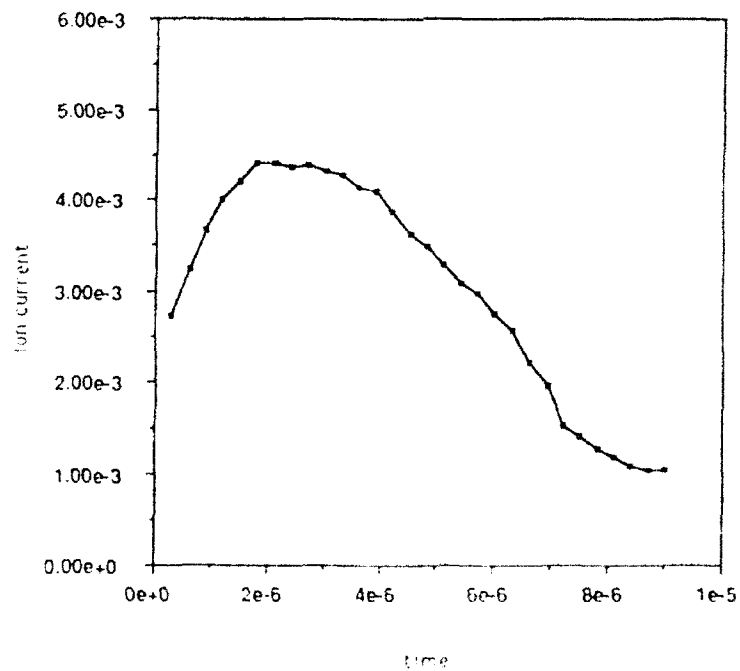


Figure 10-7. The calculated ion currents to the axisymmetric model for 1.5 and 3 μ s rise time pulses (see text for explanation).

SPEAR II Geometrical Model for NASCAP/LEO and DynaPAC

Figure 10-8 shows the geometrical model of the SPEAR II payload used for the NASCAP/LEO and DynaPAC calculations. (The identical model was used for the SPEAR II mock-up.) This geometry was based on the EUCLID (an engineering drafting and modeling product⁽¹²⁾) model constructed by Westinghouse and was converted to a PATRAN (a finite element modeling code⁽¹³⁾) model using IGES (Initial Graphics Exchange Specification protocol⁽¹⁴⁾) files as an intermediate transfer mechanism. The PATRAN "Neutral File" (specifying node locations and surface element connectivities, material numbers, and conductor numbers) is read by the object definition interface module of either code, which places the object in the grid system and performs other appropriate preprocessing.

Figure 10-9 shows the DynaPAC grid for SPEAR II, illustrating the arbitrarily nested subdivision capability. The grid spacing ranges from 1 meter (outermost grid, not shown) to 3 cm in the payload interior. The NASCAP/LEO grid had a basic mesh size of 16 cm, with subdivided regions down to 4 cm, and surrounding outer grids up to 64 cm.

NASCAP/LEO Calculations for SPEAR II

Prior to the development of DynaPAC, NASCAP/LEO was the only plasma interaction code capable of predicting sheath currents and potentials for a payload with the geometrical complexity of SPEAR II. It was recognized that the "equilibrium" plasma treatment used in NASCAP/LEO was not appropriate to the SPEAR II high voltage pulse lengths. Nonetheless, predictions made using an equilibrium code were better than no predictions at all. Figure 10-10 shows the NASCAP/LEO-calculated equilibrium sheath contours for SPEAR II.

As part of the SPEAR program, a "frozen ion" approximation was added to NASCAP/LEO. In the "frozen ion" approximation, it is assumed that electrons instantaneously attain an equilibrium distribution, but ions do not move. The space charge function, eq. (10-2), is thus replaced by

$$\begin{aligned} \rho/\epsilon_0 &= 0 & \phi &\geq 0 \\ \rho/\epsilon_0 &= (\theta/\lambda_D^2)[1 - e^{\phi/\theta}] & \phi &\leq 0 \end{aligned} \quad (10-3)$$

This approximation (appropriate up to about 1 μ s for SPEAR II parameters) provided a means for calculating sheath sizes during the short SPEAR II high voltage pulses. (See Figure 10-11.) However, it did not provide any straightforward means of calculating the transient currents to the payload or the time dependence of the currents and sheath structure.

The first question to be addressed using NASCAP/LEO was the floating potential of the payload during high voltage operation. It was not sufficient simply to assume that the floating potential

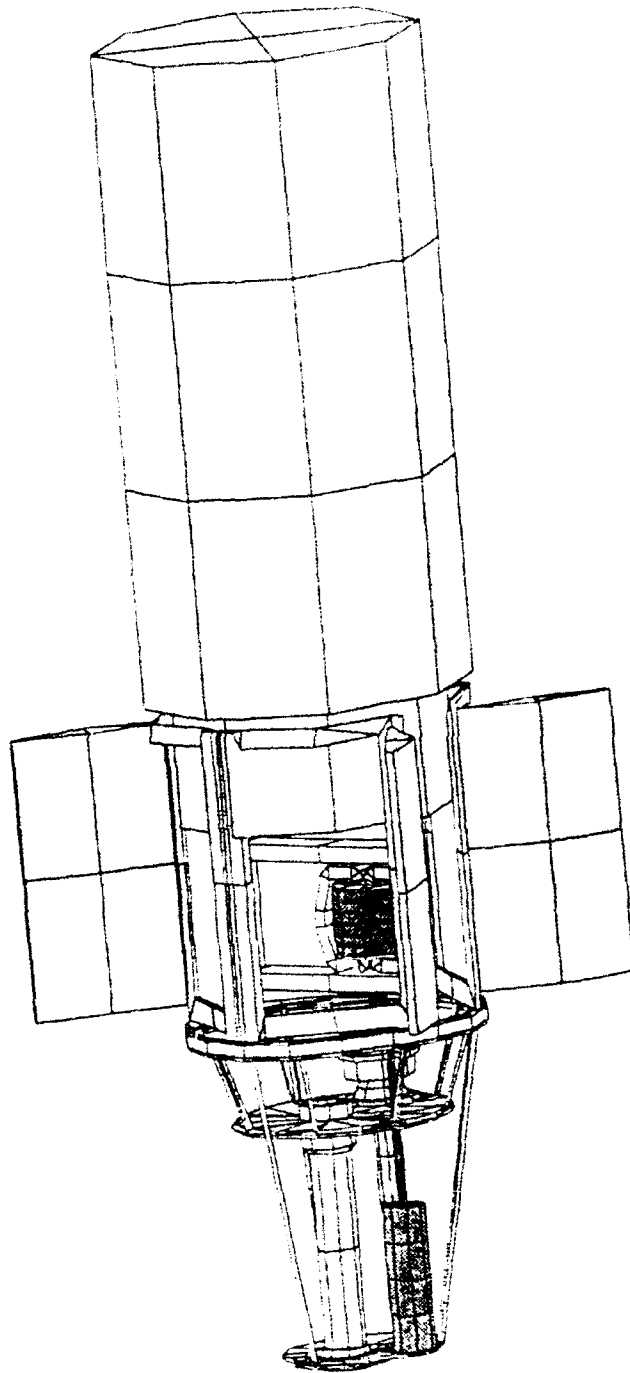


Figure 10-8. Geometrical model of the SPEAR II payload used in the NASCAP/LEO and DynaPAC calculations.

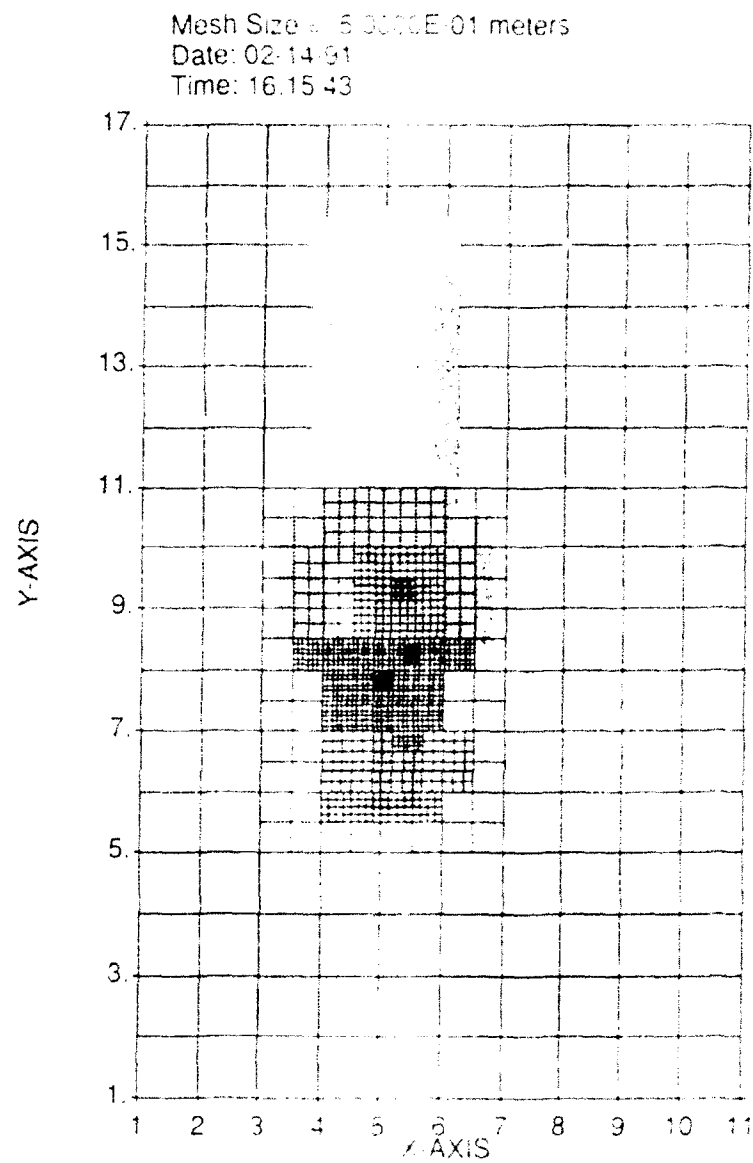


Figure 10-9. DynaPAC grid for SPEAR II. (The outmost grid, with 1 meter mesh spacing, is omitted.)

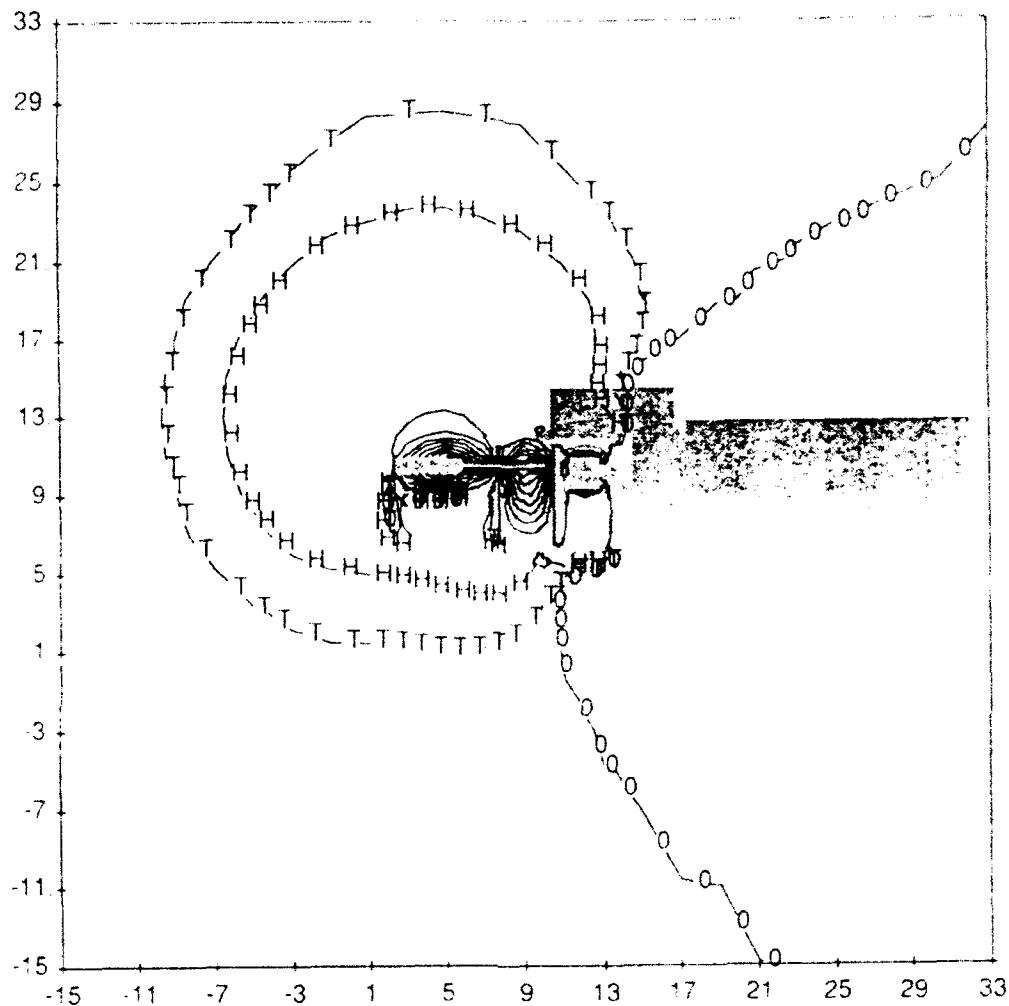


Figure 10-10. NASCAP/LEO calculated equilibrium sheath ("H" contour) about SPEAR II under laboratory conditions ($1 \times 10^8 \text{ cm}^{-3}$; 1 eV). Space charge densities are calculated using formulas appropriate to a steady-state plasma sheath (e.g., Langmuir-Blodgett). The shaded area represents the projection of the payload on the contour plans, and equipotential lines with 10 kV spacings appear near the payload. The contour at -100 volts (marked "H") is considered the sheath contour because the potential should drop to zero within 0.3 meters of the -100 volt equipotential surface. Also shown are contour lines at -10 volts (marked "T") and at zero volts (marked "O"). The payload ground surface is at +100 volts. The horizontal and vertical axes are marked in units of 16.3 cm.

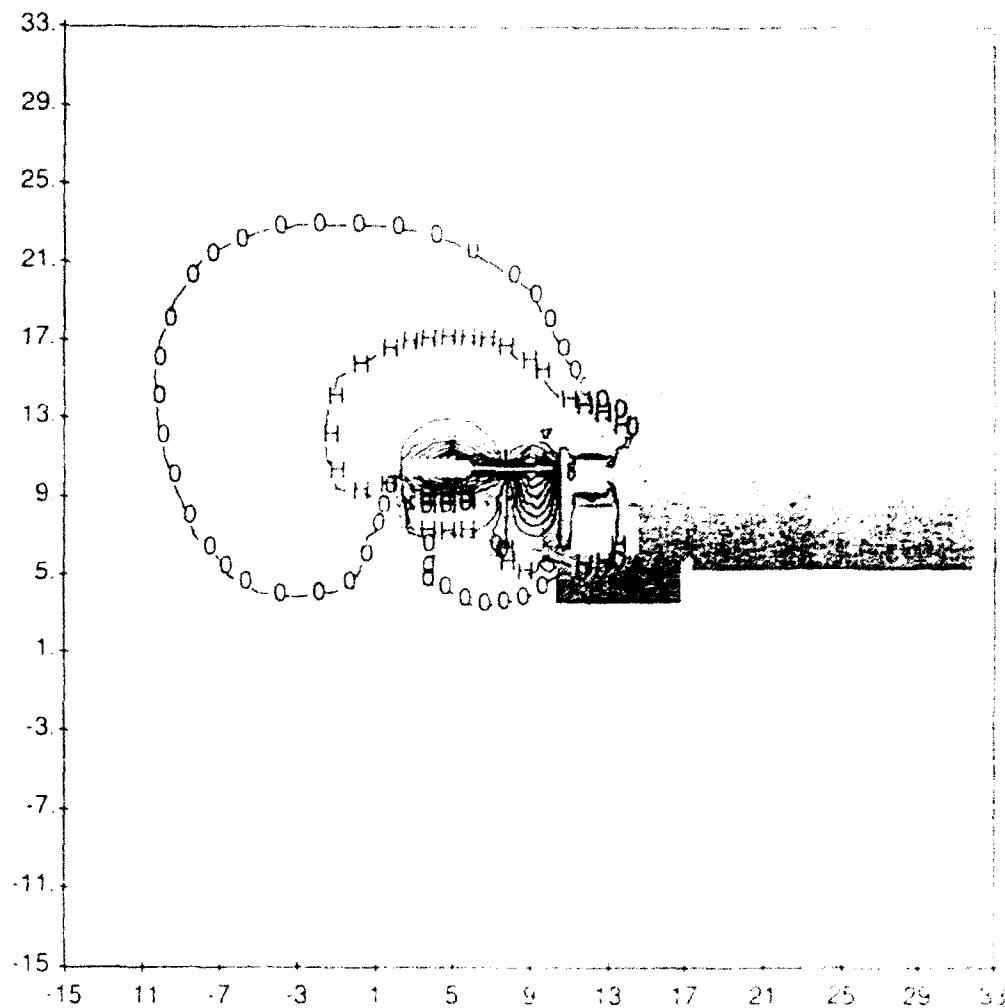


Figure 10-11. NASCAP/LEO calculated "frozen ion" sheath ("H" contour) about SPEAR II under laboratory conditions. Space charge densities are calculated assuming that ion motion is negligible (appropriate to times up to a few microseconds). Otherwise, the description of Figure 10-10 applies. Note that the transient sheath is far smaller than the equilibrium sheath, leading to considerably elevated currents in the transient regime.

calculating the electron and ion currents to the payload for several assumed values of floating potential, NASCAP/LEO predicted that the equilibrium floating potential would be less than 150 V. This prediction was confirmed insofar as the SPEAR II mockup instrumentation was unable to show any evidence of a positive steady state floating potential.

The code was next used to study the current distribution to the various components of the SPEAR II payload. For the mockup test under positive bias, NASCAP/LEO predicted a total current of -1.2 amperes for a plasma of density $1 \times 10^6 \text{ cm}^{-3}$ and temperature 1 eV. The distribution of this current to the SPEAR II components is shown in Table 10-2.

Table 10-2. Currents to SPEAR II Components	
SPEAR II Component	Calculated Current
100 kv portion of probe	500 ma
75 kv portion of probe	410 ma
Klystron battery canister	87 ma
50 kv portion of probe	75 ma
Various grounded surfaces	59 ma
High voltage lead	49 ma
Transformer secondary	34 ma
25 kv portion of probe	5 ma
Klystron bushing	0.2 ma

NASCAP/LEO calculation of currents to components of the SPEAR II mockup under positive bias conditions.

The NASCAP/LEO calculations predicted that nearly all of the current would be incident to the high potential end of the high voltage probe. This prediction was qualitatively confirmed by visual observations during the mockup test of a strong optical glow from the electron bombarded region. However, the question of how dynamic effects would modify this current distribution in the negative bias case remained open.

Transient Current Estimates Using Gilbert and NASCAP/LEO

It was recognized that equilibrium current calculations for the SPEAR II payload could not be trusted for the short pulse durations. Without a three-dimensional modeling capability it was not known to what degree the transient current would differ from the equilibrium current, or how much time was required to achieve the equilibrium configuration. To shed some light on these topics, a two-step strategy was used. First, the Gilbert code was used to calculate the time-dependent current to a sphere with parameters similar to the SPEAR II system. From the results, scaling relations were developed relating the "frozen ion" sheath size to the peak transient current. Second, NASCAP/LEO was run to calculate the size of the "frozen ion" and equilibrium sheaths about the high voltage probe, and the scaling relations were applied to determine the peak transient current.

The sample problem consisted of a 0.3 m radius sphere in an O^+ plasma with a density of 10^{17} cm^{-3} . The potential was raised to -100 kV with a 1.5 μs risetime. Using spherical probe theory, the equilibrium sheath around the sphere was calculated to have a radius of 15 m, and the steady-state ion current to the sphere was 14 mA.

The Gilbert calculation was run for 30 μs . It was found that the transient sheath expands rapidly to a radius of 4.0 m as the voltage is applied, and thereafter expands by plasma erosion at the slow rate of 3 cm/ μs , reaching a radius of 4.7 m at the end of the calculation. The current to the sphere (Figure 10-12) reaches a peak of 140 mA at 15 μs into the pulse, and falls off slowly thereafter. (These calculations gave the first indication that the SPEAR II incident ion currents might be an order of magnitude above the values obtained from the equilibrium treatment.) It was estimated that 10 ms would be required for the current to relax to the Langmuir-Blodgett¹² equilibrium current of 14 mA. (Note that the collected current correlates inversely with the sheath size. This is analogous to the space-charge-limited current collected by an inner sphere from a concentric outer sphere.)

To develop scaling a relation, we postulate that the peak current is given by

$$I_{\text{peak}} = \alpha Q/\tau, \quad (10-4)$$

where Q is a characteristic charge and τ a characteristic time. The characteristic charge is logically taken as the space charge in the sheath (which must balance the surface charge on the probe):

$$Q = (4\pi/3) n e R_s^3, \quad (10-5)$$

where we have neglected the probe volume relative to the sheath volume. The characteristic time may be taken as the time for an ion to travel the sheath radius in a uniform field given by the applied voltage over the sheath radius:

$$\tau = (2 m R^2/eV)^{1/2}. \quad (10-6)$$

For the Gilbert calculation, we have $Q = 4.3 \times 10^{-5}$ coulombs, and $\tau = 7.3 \times 10^{-6}$ seconds, so that the scaling constant takes the value

$$\alpha = I_{\text{peak}} \tau/Q = 1/2, \quad (10-7)$$

and the scaling relation is

$$I_{\text{peak}} = Q/4\tau. \quad (10-8)$$

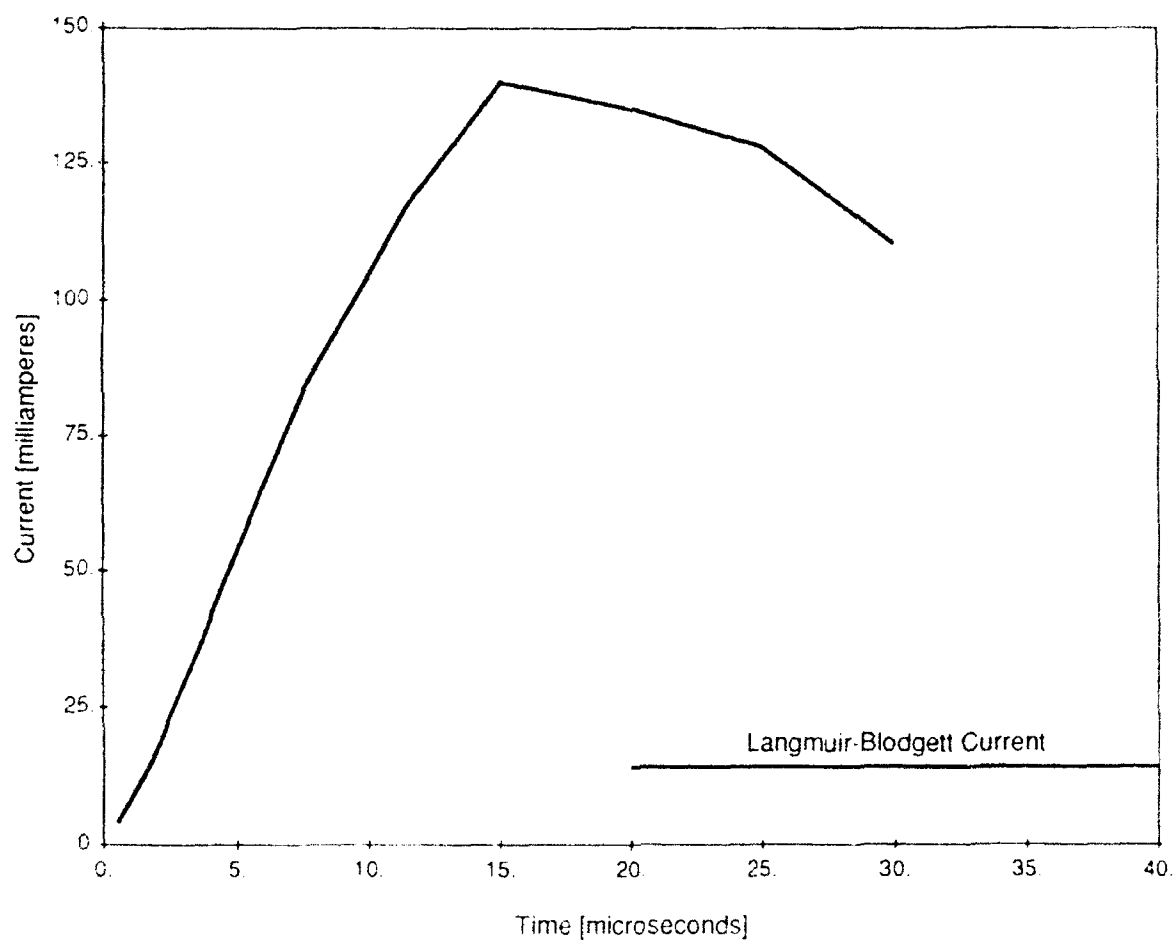


Figure 10-12. Time-dependent ion current to the sphere model of the SPEAR II payload. The Langmuir-Blodgett¹⁴ steady state current is shown for reference.

]Table 10-3 shows "frozen ion" estimates of the sheath size (calculated by NASCAP/LEO for the three dimensional representation of the SPEAR II payload under space and laboratory conditions), and the peak transient currents to the high voltage probe (predicted by scaling the Gilbert results). To obtain the actual parasitic current in the circuit, the incident ion current must be enhanced by a large factor to take into account the secondary electron yield of the incident ions. While there is a great deal of uncertainty in the secondary yield value, a yield of 25 would be a reasonable estimate.^[15] This gives a parasitic current exceeding two amperes under laboratory conditions. For comparison, the fully dynamic results (obtained from DynaPAC, as described below) predicted a total peak incident ion current of 50 mA, with 35 mA on the probe, for a parasitic current of 0.9 amperes.

Table 10-3. Transient Current Estimates			
	Gilbert	Space	Laboratory
Density [cm ⁻³]	1 x 10 ⁵	1 x 10 ⁵	1 x 10 ⁶
Equilibrium Sheath Radius [m]	15	2.3	1.8
Equilibrium Current [mA]	14	1.6	10
Transient Sheath Radius, R _s [m]	4.0	1.3 m	1.0 m
Transit Time, τ [μs]	7.3	2.4	1.6
Sheath Charge [μcoul]	4.3	0.15	0.7
Q/4τ [mA]	140	15	11
Secondary Electron Yield	25	25	25
Peak Parasitic Current [A]	3.6	0.39	2.6

Estimates of peak parasitic current (1) calculated by Gilbert for a 0.3 meter radius sphere; (2) estimated for space conditions (plasma density 10⁵ cm⁻³) using the NASCAP/LEO "frozen ion" approximation; and (3) similarly estimated for laboratory conditions (plasma density 10⁶ cm⁻³).

The predicted current levels would not impair the high voltage system operation, but would seriously impact the ability of the high voltage probe to measure the transformer secondary voltage. Figure 10-13 shows a circuit model of the probe, in which parasitic plasma current is injected one-tenth of the way from the high voltage end, and the voltage measurement is taken one-tenth of the way from the ground end. For the case of -100 kV applied to the probe, this circuit model predicts that a parasitic current of 0.5 amperes will result in the measurement being low by a factor of two.

A comparison of the probe traces obtained from the space simulation chamber tests under vacuum and plasma conditions dramatically illustrates this effect. Figure 10-14 shows diagnostic signal traces for a 50 μs, 80 kV pulse in vacuum. The high voltage probe trace is the dark, upper trace; the other traces are diagnostics taken at other components of the high voltage circuit. In

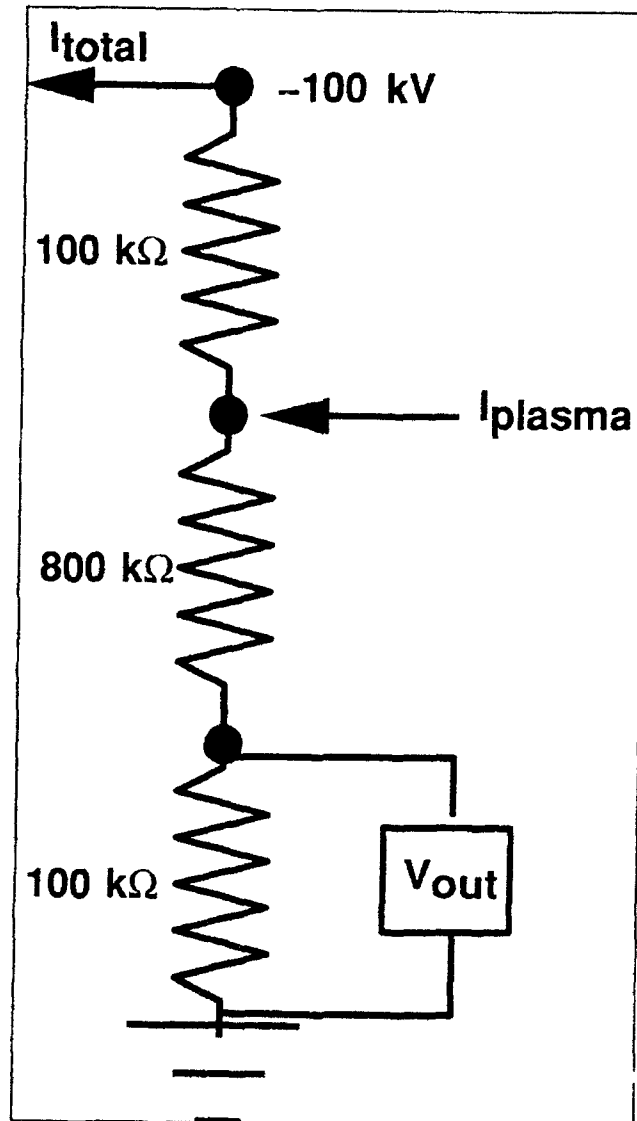


Figure 10-13. Circuit model of high voltage probe, used to estimate the effect of parasitic plasma current. The transformer secondary voltage is measured as $10 \times V_{\text{out}} = (1 - I_{\text{plasma}}) \times 100\text{ kV}$.

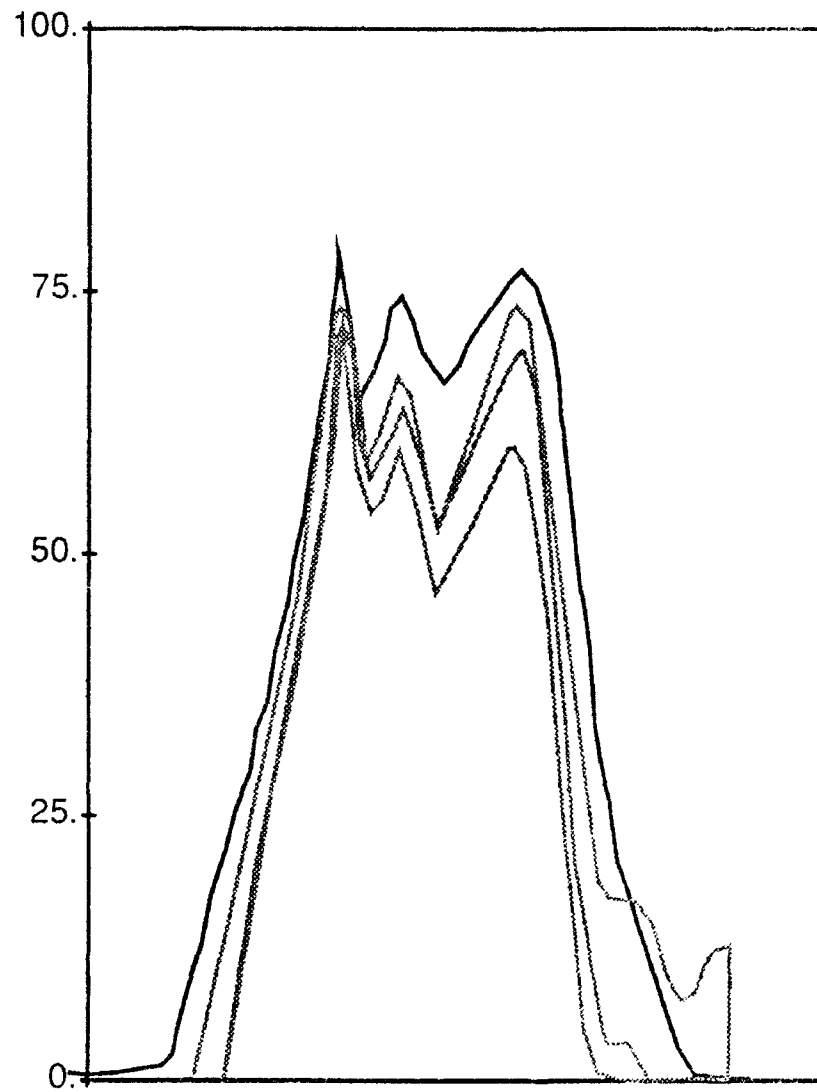


Figure 10-14. Circuit diagnostics for an 80 kV, 50 microsecond SPEAR II pulse with no plasma sources operating. The upper trace represents the transformer secondary voltage as measured by the voltage divider probe. The remaining traces are diagnostics for other components of the high voltage circuit.

Figure 10-15 the trace is shown for the same pulse parameters in the presence of a 10^6 cm^{-3} Ar plasma. The high voltage probe reading is diminished by about a factor of two, but all of the other diagnostic signals are indistinguishable from the vacuum shot. Our conclusion is that the high voltage circuit is operating properly in the presence of plasma, but the high voltage probe is reading incorrectly.

DynaPAC Calculation of Transient Currents to SPEAR II High Voltage Components

All the calculations described above either use an equilibrium or "frozen ion" space charge representation, neither of which adequately model the dynamics of the SPEAR II pulse, or else model the geometry as axisymmetric, which is not an adequate approximation to the partially enclosed structure of SPEAR II. Estimates of the peak incident ion current, the division of this current among the SPEAR II high voltage components, and the timescale of the current obtained by scaling the results of equilibrium codes based on results for poorly representative geometry required confirmation by a fully 3-D dynamic code. For this reason the DynaPAC code, already under development for Geophysics Laboratory (now Phillips Laboratory) was supported by the SPEAR program.

With the development of DynaPAC for the SPEAR II program, it was possible to calculate the time dependent ion currents to the various SPEAR II high voltage components. The geometrical model of the SPEAR II payload was the same as was used for the NASCAP/LEO calculations described above. Initially, each DynaPAC grid was filled with a regular array of ion macroparticles, representing an Ar plasma with a density of $1 \times 10^6 \text{ cm}^{-3}$. At each timestep, a time-dependent voltage, representing a 100 kV, 50 μs pulse with 3 μs risetime, was applied to the high voltage components, the electrostatic potential field was calculated using the known ion distribution and an analytic expression for the electron charge density, and the ion macroparticles were tracked in the new field for the specified timestep length. After 3 μs , the ion macroparticles assumed the configuration represented in Figure 10-16. The figure shows ion voids near the klystron battery pack and the transformer. This indicates that substantial ion motion has taken place in these regions, which had high fields due to the close proximity of grounded struts and bulkheads. By contrast, ions at large distances were just beginning to be accelerated toward the high voltage probe, as indicated by the curvature of the originally straight lines of macroparticles.

Figure 10-17 shows the calculated ion currents incident on various SPEAR II payload components. The klystron battery pack and transformer (which are well shielded electrostatically by struts and bulkhead) had peak currents of about 12 mA each, which occurred approximately 6 μs into the pulse. The current to the high voltage probe (which influences a larger volume of plasma) rose to a peak exceeding 30 mA at about 12 μs . The total incident ion current (which includes currents to the high voltage leads) peaked at around 55 mA approximately 8 μs into the pulse. All of the currents fell off slowly after reaching their peak values. (For comparison, NASCAP/LEO equilibrium calculations for these conditions gave a total payload current of 6 mA. See Table 10-4.)

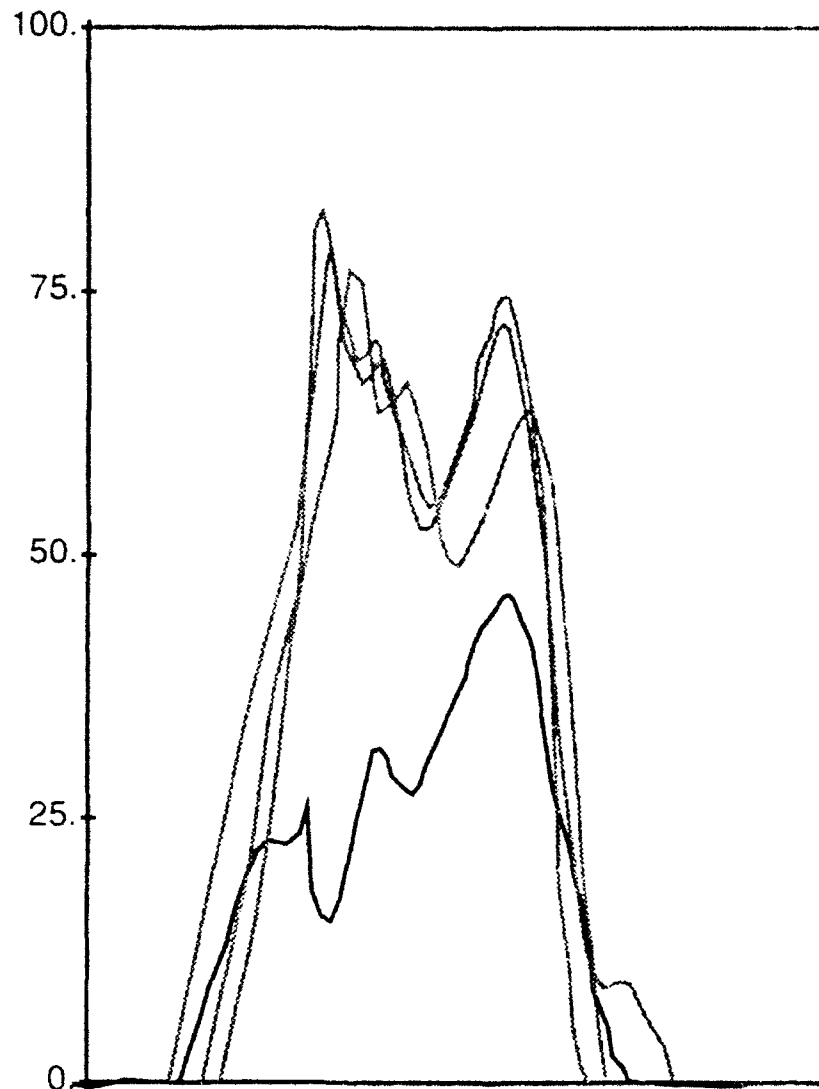


Figure 10-15. Circuit diagnostics for an 80 kV, 50 microsecond SPEAR II pulse with plasma sources operating. The transformer secondary voltage measurement is about half the value measured in vacuum, and now appears as the lower curve. Remaining circuit diagnostics are unchanged. DynaPAC calculations, anticipated by NASCAP/LEO and Gilbert results, showed that the voltage divider probe measurement was incorrect in the presence of plasma due to high incident ion currents to the probe.

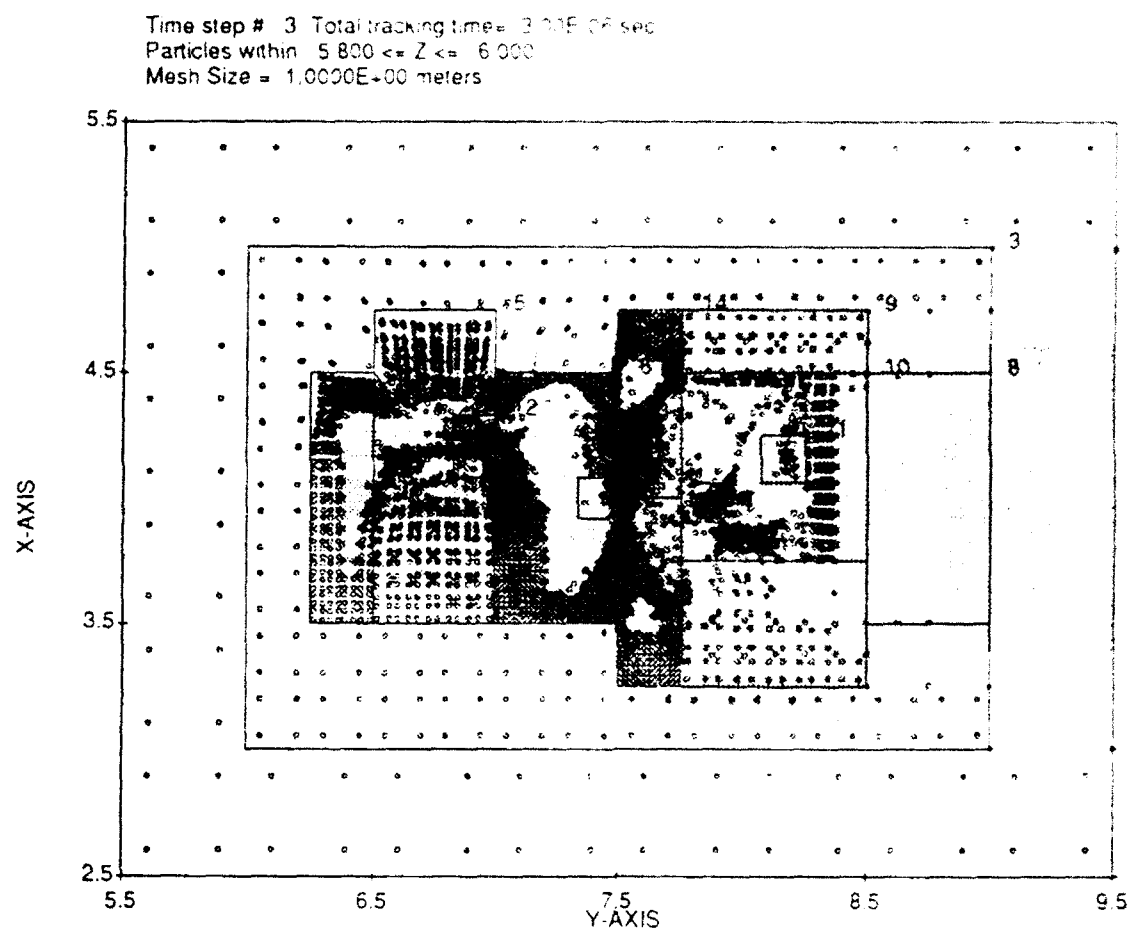


Figure 10-16. Calculated ion macroparticle positions 3 μ s into a SPEAR II high voltage pulse (scale marked in units of meters.)

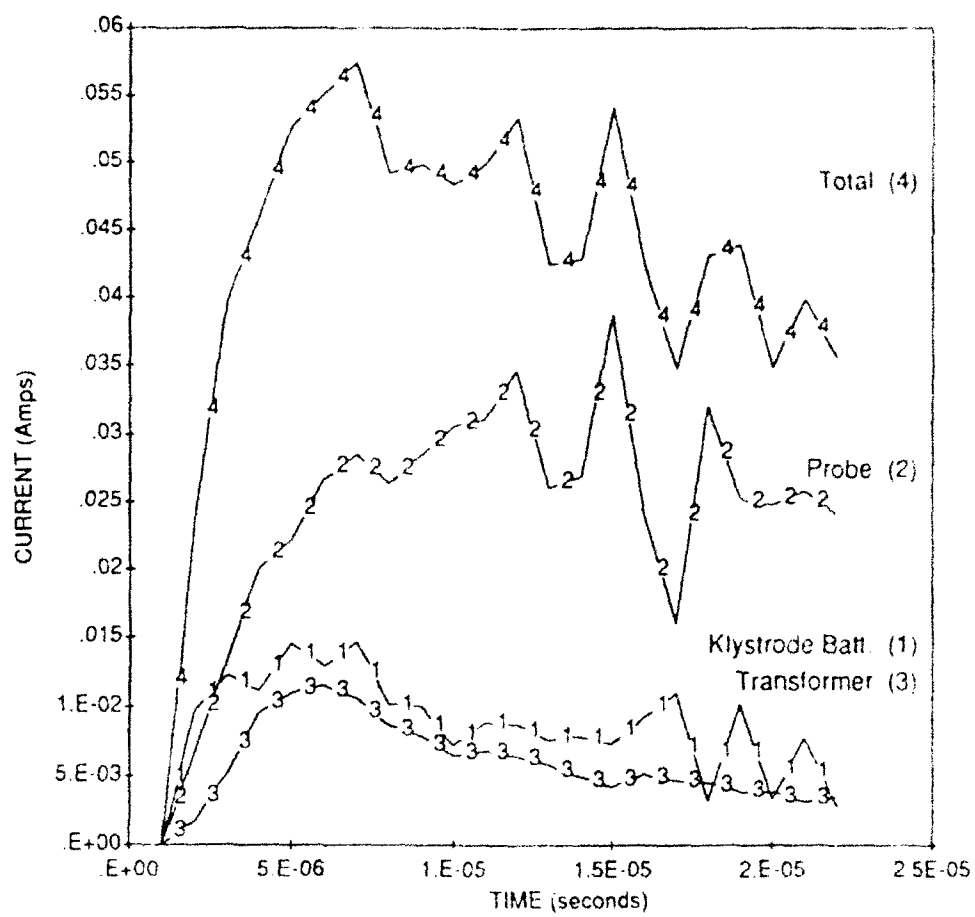


Figure 10-17. Calculated incident ion currents to the SPEAR II high voltage probe, klystrode battery canister, and pulse transformers.

Table 10-4. Predicted Incident Ion Currents to SPEAR II	
Equilibrium Calculation	6 ma
Pre-Test Prediction	100 ma
DynaPAC Calculation	55 ma

Taking into account the secondary electron yield, the predicted parasitic current through the upper part of the probe is nearly one ampere. As discussed in the previous section, this is easily enough current to cause the observed erroneous measurements by the high voltage probe.

A rough estimate of the time needed to approach an equilibrium sheath may be obtained as the time required to drain the equilibrium sheath volume (approximately a 2.1 meter radius sphere) of charge at a mean current of about 40 mA. This approach gives a sheath formation time of 150 μ s, which is three times the longest SPEAR II high voltage pulse. Therefore, the equilibrium formulation is never appropriate for the SPEAR II operating conditions.

Summary of Technical Achievements and Capabilities

This chapter has discussed the development of three plasma interaction model computer codes and their application to the SPEAR program. The two existing codes, NASCAP/LEO and Gilbert, were both enhanced under the SPEAR program, and their ability to make useful and non-obvious predictions was demonstrated. The new code, DynaPAC, demonstrated its ability to perform dynamic plasma interactions calculations for complex systems.

Achievements in the area of code development, enhancement, and validation include:

- (1) For NASCAP/LEO:
 - (a) Demonstration of the ability to calculate equilibrium sheaths and current distributions for systems with high geometrical complexity;
 - (b) Addition of a "frozen ion" approximation to aid in analysis of transient sheath phenomena.
- (2) For Gilbert:
 - (a) Development of an internal boundary condition to mimic the electrostatic effects of a screen;
 - (b) Demonstration of the ability to predict spatial and temporal current distributions with sufficient accuracy to make meaningful physical predictions.
- (3) For DynaPAC:

- (a) Development of a computer code capable of performing dynamic plasma calculations for systems with high geometrical complexity;
- (b) Development of a programmer-friendly DataBase Manager for the allocation, storage, and retrieval of large arrays of data;
- (c) Development of high-order finite element techniques to guarantee accurate potential solutions with strictly continuous electric fields;
- (d) Development of pre- and post-processors for ease of problem setup, input generation, and data visualization.

Applications of these codes to the SPEAR program include:

- (1) Prediction (using Gilbert) of the rapid (or slow) breakdown of a negatively biased high voltage fixture by the presence (or absence) or calculable ion current to the "triple point";
- (2) Calculation (using Gilbert) of dynamic ion currents for the small chamber test of SPEAR II, showing that the intermediate-length pulse was most likely to break down;
- (3) Calculation (using NASCAP/LEO) of the equilibrium current distribution and estimate of the equilibrium floating potential for SPEAR II;
- (4) Development (using Gilbert) of a theory for dynamic sheath development and transient current for a negative probe, showing that transient currents can exceed equilibrium currents by an order of magnitude;
- (5) Pre-test prediction (using Gilbert and NASCAP/LEO) of high parasitic currents to the SPEAR II high voltage probe in the presence of plasma;
- (6) Calculation (using DynaPAC) of the time-dependent plasma currents to the SPEAR II high voltage components.

SURFACE FLASHOVER THEORY WITH APPLICATIONS TO HIGH VOLTAGE CONDITIONING

Introduction

The SPEAR program revealed the need to condition high voltage components for the space environment. Both the high voltage transformer and the klystron bushing required a conditioning sequence before high voltage standoff could be achieved. Conditioning is an art and unpredictable and techniques that work for one design or environment can fail in a different situation. In practice it is not possible to guarantee that a conditioning technique will work or to know how long the conditioning will last. To gain insight into the conditioning process, a surface flashover theory was developed that describes, quantitatively, the initiation of flashover. The theory reveals the role surface desorption plays in the arc initiation process and is an important step in understanding, quantitatively the process of conditioning model to aid in the design of high voltage components and conditioning techniques.

Application

High voltage insulation in space emerges as a critical issue because of the advantages inherent in operating high voltage SDI systems in configurations where bushings, components, and distribution networks are exposed to the ambient environment. Recognizing this, the SPEAR program initiated a number of space simulation experiments, conducted in laboratory plasma chambers, that demonstrated that:

- (1) The plasma induced arcing could be diminished through changes in the geometry of high voltage components. Computer simulations substantiated by laboratory experiments showed that the use of electrostatic screens and electrode shaping redirected ions away from the triple points and increased high voltage standoff.
- (2) High voltage standoff capability of insulators improved with conditioning. Conditioning consists of repeatedly applying high voltages to a component allowing it to arc until it is capable of withstanding the high voltage. The conditioning process is understood qualitatively as resulting from changes in the surface properties such as removal of surface contaminants and gas desorption. The theory developed for the SPEAR program relates high voltage standoff to surface desorption coefficients and conditioning leakage currents to quantity of desorbed gas. As it stands now the theory can predict pressure increases during the condition process which can be used as an independent measurement, (a) to verify that conditioning is occurring, and (b) to estimate the conditioning time required.

Innovative Concepts

The SPEAR model of surface flashover initiation quantitatively predicts breakdown thresholds and gas release given surface electron impact desorption properties. The theory combines the effects of surface charging, surface secondary electron emission, neutral desorption, and ionization within the desorbed gas. Because the theory relates the quantity of desorbed neutrals to the flashover current and applied voltage, it can be tested in laboratory experiments. With additional data on surface desorption over periods of electron impact, the theory can be used to predict the conditioning needed to reduce the desorption rate below flashover thresholds. This also could be tested and if confirmed used in the design of high voltage components and conditioning strategies.

A Theory of Surface Flashover

In SPEAR chamber tests the neutral pressure was observed to increase during conditioning of the high voltage components. This revealed the role of surface neutral desorption in the arc initiation process. Impact by impinging electrons has been proposed as the mechanism for this desorption. We utilize the hypothesis of desorption of gas and its subsequent ionization by electron bombardment to construct a model of surface flashover. The idealized configuration in Figure 10-18 shows two electrodes separated by an insulator length l and charged to a potential difference V . The inter-electrode space may be filled by a plasma of density n_p .

See Figure 10-18 on page 99

Figure 10-18. Idealized configuration for surface flashover problem shows insulator of length l with surface charge density σ_s .

One imagines that the surface of the insulator becomes positively charged so that any electrons emitted from the cathode near the triple point strike the insulator, producing secondary electrons, which also remain close to that surface. Electrons bombarding the surface release adsorbed

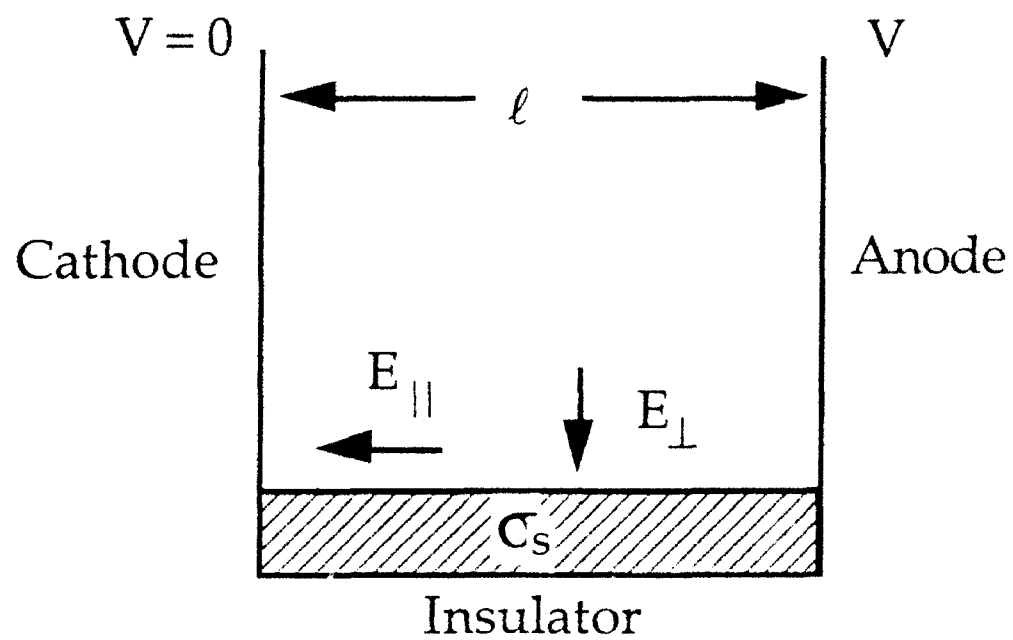


Figure 10-18. Idealized configuration for surface flashover problem shows insulator of length ℓ with surface charge density σ_s .

gases that become ionized by collisions with sufficiently energetic electrons, leading to an increase in the flux of electrons bombarding the insulator.

The model equations for this system are as follows:

$$\frac{1}{e} \frac{d\Sigma}{dt} = j_{out} - j_{in}, \quad (10-9)$$

where Σ is the charge per unit area on the insulator and j_{in} and j_{out} are the ingoing and outgoing fluxes of electrons. The fluxes j_{in} and j_{out} are related by the secondary emission yield $Y(\epsilon)$ at the energy of the incident electrons is ϵ .

$$j_{out} = Y(\epsilon) j_{in}. \quad (10-10)$$

It is useful to define the surface charge density, σ_e , to be the charge in a layer above the surface

$$\sigma_e = \int n_e dy = \bar{n} \delta, \quad (10-11)$$

where n_e is the electron density in the space above the layer, whose thickness is δ . The charge density, σ_e , is determined by continuity as shown in equation 10-12.

$$\frac{\partial \sigma_e}{\partial t} + \frac{\partial K}{\partial x} = -j_{in} + j_{out} + S. \quad (10-12)$$

The three terms on the right hand side of equation 10-12 are the sources and sinks of charge due to charge leaving the layer, entering the layer from the surface, and creation of charge in the layer due to ionization. In equation 10-12, K is the flux $\sigma_e \bar{v}$ ($\text{cm}^{-1} \text{sec}^{-1}$) corresponding to σ_e . The ionization rate per unit area of the current layer is denoted by S . Recombination and attachment are neglected.

For simplicity we have assumed that all electrons in the layer are born on the surface of the insulator ($y=0$) with a single energy $\epsilon_0 = \frac{1}{2}mv_0^2$ and a velocity v_0 in the y direction.

The preceding equation must be complemented by equations that determine the density N of gas in the layers:

$$NV_0 = j_0 = \gamma j_{in}, \quad (10-13)$$

where γ is the number of gas molecules desorbed per incident electron and V_0 is the mean velocity of desorbed molecules normal to the insulator surface. It is assumed that gas molecules move through δ in times δ/V_0 that are negligible in comparison with the time scales of the phenomena of interest.

We now consider steady state solutions of the foregoing equations and seek conditions indicative of breakdown. From equations 10-9 and 10-10, we require

$$\epsilon = \epsilon_1, \quad (10-14)$$

where ϵ_1 is the first crossover energy defined by

$$Y(\epsilon_1) = 1, \quad (10-15)$$

$$\frac{\partial Y}{\partial \epsilon}(\epsilon_1) > 0. \quad (10-16)$$

We can relate the parallel and perpendicular electric fields as follows. The secondary electrons leave the surface with energy ϵ_0 and return to the surface with energy ϵ_1 a time, $\tau = \frac{2mv_0}{eE_{\perp}}$, later.

The distance traveled under the influence of the parallel electric field is $d = E_{\parallel}\tau$. This along with energy conservation, $\epsilon_1 - \epsilon_0 = E_{\parallel}d$, can be used to produce

$$E_{\perp} = \left(\frac{2\epsilon_0}{\epsilon_1 - \epsilon_0} \right)^{1/2} E_{\parallel}. \quad (10-17)$$

In obtaining this relation, one neglects electron energy loss by ionization as well as by inelastic processes. The effect of this neglect should be examined.

The ionization rate, S , due to collisions by the surface current of electrons, K , with the desorbed gas, N , is:

$$S \approx NK\sigma = \frac{\gamma J_{in}}{V_0} K\sigma. \quad (10-18)$$

The surface current, K , can be expressed in terms of the incident electron flux, J_{in} by noting that K is just the current generated the secondary electrons hopping,

$$eK = (J_{in}\tau) \left(\frac{d_{hop}}{\tau} \right) = J_{in} \frac{4\epsilon_0 E_{\parallel}}{E_{\perp}^2}, \quad (10-19)$$

$$S = \frac{\gamma(\sigma)}{V_0} \left(\frac{2\theta E_1}{\epsilon_1 - \epsilon_0} \right) K^2 = \alpha K^2. \quad (10-20)$$

solving for K and substituting in equation 10-19, we have

Substituting this into equation 10-17, and gathering the constants into the coefficient, α , gives

$$\frac{\partial K}{\partial x} = \alpha K^2, \quad (10-21)$$

integrating equation 10-21 gives

$$K = \frac{K_0}{1 - K_0 \alpha x}, \quad (10-22)$$

where eK_0 is the current at the cathode end of the insulator. Electrons may be liberated at the cathode by field emission or as a result of ion bombardment of the cathode. In general, the magnitude of K_0 depends on the parameters of the discharge and the surrounding ambient plasma including, in particular, the electric field and ion current distribution near the cathode triple point. We denote these dependencies by the expression $K_0 = K_0(\{E_c, \{j_i\})$, that is, K_0 is taken to be some function of the electric field E_c and ion current density j_i at the cathode. The latter includes ions generated by collisions with electrons in the layer δ that move to the cathode under the influence of the fields.

Although the mechanisms associated with cathode emission are not well understood, we can nevertheless define a critical emission current

$$K_{oc} = (\alpha \ell)^{-1}, \quad (10-23)$$

corresponding to breakdown conditions.

Application to SPEAR II and other Systems

We seek to determine if the critical current given in equations 10-23 is in accord with the current $I = 1.3 \times 10^{-4}$ amp observed by Gray ⁽¹⁶⁾ in a simple flashover channel with a gap $\ell = 1.3 \times 10^{-2}$ cm, a flashover field of 20 kV/cm and a channel width $w \sim 10^{-3}$ cm. This gives

$$qK \approx \frac{I}{W} \approx .1 \frac{\text{amp}}{\text{cm}}. \quad (10-24)$$

From equations 15-20

$$\alpha \ell = \frac{\gamma(\sigma)}{V_0} \frac{2\theta E_1}{\epsilon_1 - \epsilon_0} \ell. \quad (10-25)$$

Taking $\langle \sigma \rangle = 10^{-16} \text{ cm}^2$, $V_0 = 4 \times 10^4 \text{ cm/sec}$, $\epsilon_1 - \epsilon_0 \approx 100 \text{ eV}$, we find,

$$qK = \frac{1.6 \times 10^{-19}}{\alpha \ell} = \frac{1.6 \times 10^{-19}}{1.3 \times 10^{-18} \gamma} \approx \frac{0.1}{\gamma} \text{ amp/cm.} \quad (10-26)$$

This value is in reasonable accord with experimental results for $\gamma \sim 1$. A desorption probability of a few molecules per electron is consistent with results reported by Hackam^[17], and is a reasonable value if the surface is heated by electrons.

The theory relates the surface current, K , to the rate of desorption of gas from the insulator surface. As will be shown below, the rates predicted are in qualitative agreement with the pressure increases observed in SPEAR II during conditioning sequences on the pad at White Sands.

Using equation 10-13, we can integrate the flux of desorbed neutrals over the surface contributing to the flashover to get the total current of neutrals, R .

$$R = \iint_{\text{surface}} NV dA, \quad (10-27)$$

with equations 10-19 and 10-22 this can be expressed in terms of the flashover current, I_c , as

$$R = \gamma \frac{I_c}{e} \frac{(1 - K_0 \alpha \ell) \ln(1 - K_0 \alpha \ell)}{K_0 \alpha d}. \quad (10-28)$$

During flashover described by equations 10-22 and 10-23 a large but obviously finite current flows. Power supplies have current limits and will control K_0 to give a large but finite currents. With this in mind we can approximate equation 10-28 by assuming $K_0 \alpha \ell$ is near 1 say .9-.99 corresponding to an amplification of 10-100. In this case we have,

$$R \approx (.1 \text{ to } .3) \cdot \gamma \frac{I_c}{e} \frac{\ell}{d}. \quad (10-29)$$

This equation for low value of $K_0 \alpha \ell$ where the prefactor in equation 10-29 is one, states that the

rate of desorbed neutrals equals $R = \left(\text{Current of electrons in flashover, } \frac{I_c}{e} \right) \cdot \left(\text{Number of hops along flashover paths, } \frac{\ell}{d} \right) \cdot \gamma$. The

total amount of neutrals produced during conditioning flashover is the rate of neutral production times the flashover time. For the SPEAR II conditions, the number of electrons involved in a typical flashover of length $\tau = 10^{-5} \text{ s}$ is

$$\frac{I_c \tau}{e} = \frac{10a \cdot 10^{-5}s}{1.6 \cdot 10^{-19}C} = 10^{15} \quad (10-30)$$

The ratio, $\frac{l}{d}$, is the number of hops of the electrons along the flashover surface. This is just the number of intervals with energy $e_1 = 50\text{eV}$ make up the standoff voltage.

$$\frac{l}{d} = \frac{10^5\text{v}}{50\text{v}} = 2000 \quad (10-31)$$

For each electron impact onto the surface γ neutrals are released into the chamber. The precise value of γ is uncertain but is between 1 and 10 for impact energies of $e_1 = 50\text{eV}$. The number of gas molecules released during a discharge is the $n = 10^{18} - 10^{19}$.

Assuming during the SPEAR II conditioning sequences that this amount of neutrals was emitted into a volume of about a cubic meter it would produce a pressure of between 10^{-4} and 10^{-3} torr. This is consistent with the observations from White Sands that the pressure increased during each conditioning sequence.

Equations 10-20, 10-22 and equation 10-29 are important steps in understanding conditioning. Equations 10-20 and 10-22 reveal the drivers in the surface flashover process. In general it is not possible to control the flashover path length, l , so conditioning must modify the surface desorption properties described by α , namely γ . Decreasing the surface desorption coefficient will increase the flashover threshold. Conditioning does exactly this by driving neutrals from the surface of the insulator. Moreover, equation 10-29 relates the amount of surface desorption to the conditioning current. With further development and experimental confirmation, this could be used to diagnose conditioning of high voltage components by giving a measure to the conditioning process. For example, measuring the flashover current and the pressure of the desorbed neutrals could be used with equation 10-29 to give γ which could be used as a measure of the condition of the surface.

New Technical Achievements and Capabilities

- (1) A new surface flashover theory has been developed for use by the SPEAR program and other high voltage operations in space.
- (2) The theory relates surface flashover current to electron impact induced surface desorption. The pressure increases due to these neutrals and are consistent with the pressure observations during the SPEAR II conditioning sequences on the pad at White Sands.
- (3) The theory provides an important first step in understanding the process of high voltage conditioning. Further development could result in a predictive model of conditioning.

QUICK MODEL OF SPACECRAFT OUTGASSING PLUMES

Introduction

A new, quick running model of the bulk neutral density from outgassing has been developed after the SPEAR I flight for the SPEAR II program. The model includes the effects of reflection from surfaces as well as scattering by the ambient ram neutrals. The model is quick running and can be integrated into engineering design codes such as EPSATTM. The model showed that the outgassing of the G-10 booms was insufficient to cause ionization breakdown during the SPEAR I flight even for the extreme case where the G-10 was assumed to be responsible for the high pressures measured by the neutral pressure gauge. Additionally, return flux of outgassing due to collisions with the ambient environment was shown to be negligible. Preflight calculations performed for SPEAR II showed that sheath ionizations would have no effect on the power system performance. This was confirmed in the Plumbrook chamber tests where no sheath breakdowns were observed.

Application

Typical space systems must operate in a wide range of neutral contaminant environments. The ambient neutral density changes with season, time of day, and orbit. Attitude control thrusters periodically fire. Outgassing rates from surfaces change with time, and accommodation rates depend on incident fluxes, which in turn depend on all of the above. The neutral environment can cause deleterious effects to exposed high voltage components. Paschen breakdown can occur if the neutral density falls near the Paschen minimum. Neutrals in electron collecting sheaths can have bulk breakdown (sheath ionization) to the background plasma and other components as was observed in the SPEAR I Plumbrook chamber tests. When designing for these changing environments, it is necessary to have quick estimates for the neutral density at select positions (such as near a high voltage component) throughout the time period. The SPEAR outgassing model allows the rapid calculation of the bulk neutral densities around complex spacecraft such as SPEAR I and SPEAR II. The model is complementary to the Auburn outgassing model; the S-Cubed model uses the Auburn surface and complex object rates as input and calculates the external expansion including scattering off surfaces and the ambient ram.

Innovative Concepts

The SPEAR contamination model includes the return flux scattered from the ambient ram. The model makes use of the scale in variance of the physics to enable a quick look-up scheme to be employed that replaces the volume integral used in standard contamination codes.

The surface to surface view factors, which determine the reflection contribution from due to neutral accommodation, are computed by breaking the surfaces into triangles and then using the analytic result for the solid angle subtended by a triangle. This approach replaces a surface integral that is used in many contamination models.

The Quick Outgassing Model

The neutral effluent due to outgassing and accommodation is generally of low enough density that collisional mean free paths are large compared with object dimensions. For this case, neutrals leaving a surface travel in straight lines and either leave the region of interest or hit another surface. Neutrals that hit another surface either stick or are accommodated. This process is shown below in Figure 10-19.

See Figure 10-19 on page 107

Figure 10-19. The neutral density at a point arises from a) direct surface outgassing, and b) reflections (accommodation) from surfaces, and c) scattering off of the ambient ram neutrals.

The neutral density at \mathbf{x} is the sum of the outgassing density from each surface plus contributions due to accommodation of neutrals incident from other surfaces and the ram scattering. Each surface contributes a density given by,

$$\rho = \iint dS \cdot r \frac{C}{r^2}, \quad (10.32)$$

where C determines the outgassing rate. The above expression is proportional to the view factor of the surface S at r . It is convenient to evaluate r directly above the surface, S

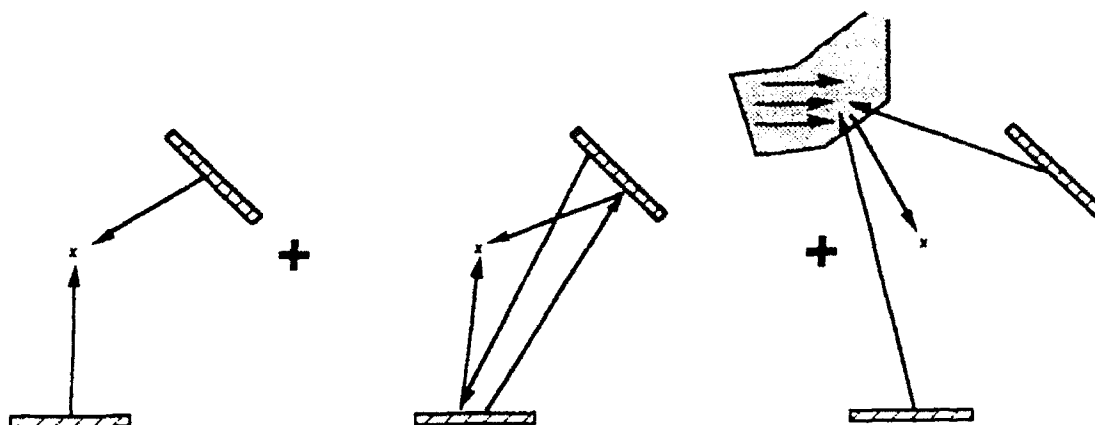


Figure 10-19. The neutral density at a point arises from a) direct surface outgassing, and b) reflections (accommodation) from surfaces, and c) scattering off of the ambient ram neutrals.

$$\rho(0) = 2\pi C. \quad (10-33)$$

Hence we can express the density at r from S in terms of the outgassing density at the surface and the solid angle Ω , subtended by S at r .

$$\rho = \rho(0) \frac{\Omega}{2\pi}. \quad (10-34)$$

The total density from all surfaces is then,

$$\rho = \sum_{\text{surfaces } i} \rho_i(0) \frac{\Omega_i}{2\pi}. \quad (10-35)$$

In the above expression, $\rho_i(0)$ is not the bare density due to outgassing by surface i but must include accommodated neutrals from other surfaces. Designating ρ^0 to be the bare outgassing density column vector for all surfaces and $\rho(0)$ to be a vector containing the total neutral densities for all surfaces, including multiple accommodations, we have the following matrix equation

$$\rho(0) = \rho^0 + M \cdot \rho(0), \quad (10-36)$$

where M is a matrix of surface to surface view factors including an accommodation factor (which conserves flux at the surface and depends on the incoming flux and the surface temperature). Although this can be directly solved for $\rho(0)$ in terms of ρ^0 as,

$$\rho(0) = (1 - M)^{-1} \rho^0, \quad (10-37)$$

it is more convenient to iteratively estimate $\rho(0)$ using,

$$\rho(0) = \rho^0 + M \cdot \rho^0 + M \cdot M \cdot \rho^0 + \dots \quad (10-38)$$

Each iteration corresponds to a reflection. Typically one iteration (corresponding to single reflection) is sufficient. The calculations presented below use the single reflection approximation. In practice M , is computed once for a system configuration and then used for any ambient ram environments and outgassing rates.

Finally, the total neutral density at a point is given by the sum of the contributions from each surface plus the ram scattering contribution. This latter component can be expressed as a volume integral over the scattering sources throughout space with

$$P_{\text{return}} = P_{\text{outgassing}} \frac{A_s}{\lambda X_s} \iiint \frac{\mathbf{r}_s \cdot \mathbf{v}_s}{r_s^3} \frac{\mathbf{r} \cdot \mathbf{v}_r}{r^3} r^2 dr d\cos\theta, \quad (10-39)$$

where $\vec{r}_s = \vec{r} - \vec{x}_s$, A_s is the area of the surface, $\rho_{\text{outgassing}}$ is the outgassing density at the surface, λ^{-1} is $\sigma \rho_{\text{ambient}}$, and \vec{V}_s , \vec{V}_r are unit vectors in the direction of the outgassing surface and the ram respectively. All distances are expressed in terms of x_s , the distance between the surface and observation point. In the above equation, if the dot products are less than zero, the dot product is taken to be zero. This occurs when the integration volume is behind the outgassing surface and when the scattering by the ram cannot get to the observer.

See Figure 10-20 on page 110

Figure 10-20. The ram scattering contribution to the neutral density can be expressed as a volume integral over the scattering sources throughout space.

As seen in equation 10-39 the dimensional variables have been entirely scaled out leaving only the orientational (angular) dependences α , β , and ϕ . Therefore, the integral can be done numerically for several values of these angles and tabulated for subsequent use. This reduction of a three dimensional integral to a simple table look-up is the key to the speed of the backscatter return flux calculations in the SPEAR outgassing model.

Equation 10-39 also shows that return flux from outgassing scattering is negligible unless the size of the source is comparable to the mean free path of the ambient neutral. For SPEAR above 200Km where the neutral density is $< 10^{16}/\text{m}^3$, this is less than 1% effective.

Application To SPEAR

The SPEAR experiments were designed to investigate the space environment interactions with high voltage components. In SPEAR I, high voltage plasma current collection in the presence of the earth's magnetic field was investigated. At issue were the extent that non-classical mechanisms such as anomalous scattering, turbulence, and ionization affect current collection. The methodology of this investigation was to compare the SPEAR I experimental results for

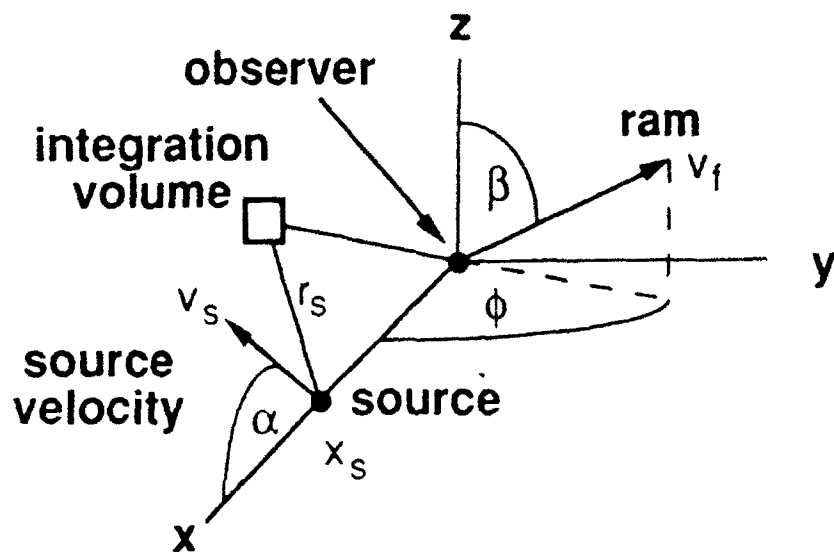


Figure 10-20. The ram scattering contribution to the neutral density can be expressed as a volume integral over the scattering sources throughout space.

current collection with the results of the NASCAP/LEO^[22] and POLAR^[23] codes which assume classical current collection mechanisms (plasma particles move under the influence of non-oscillating fields). This, however, would be conclusive only if the effects of neutral ionization could be ignored. The neutral density calculations using the outgassing model discussed showed just that. Preflight calculations were performed for SPEAR II. The calculations showed that external outgassing would not cause sheath ionization breakdown.

Figure 10-21 shows the SPEAR I object and ranges for surface outgassing rates provided by Lloyd Gordon of Auburn University for the hot aluminum body, G-10 boom and G-10/aluminum bushings and aluminum spheres. The major unknown in these calculations was the outgassing rate of the G-10 booms. Figure 10-22 shows the neutral densities about SPEAR I as calculated using the above theory. The highest densities in this calculation are less than 10^{16} m^{-3} . This is far lower than the neutral densities measured during the SPEAR I flight ($>10^{17} \text{ m}^{-3}$). Because the G-10 outgassing rate was suspect, we increased the G-10 rate until the neutral density in the vicinity of the neutral gauge reached the observed levels. This required an increase in the G-10 outgassing rate by two orders of magnitude. This new outgassing rate was used in the calculation shown in Figure 10-23. This calculation was considered an extreme upper bound on the neutral density about SPEAR I. As seen in the figure, even for the extreme outgassing rate assumed for the G-10 boom, in the sphere region the neutral density is significantly less than 10^{17} m^{-3} . For these densities ionization effects in electron sheaths are not important.

In summary, outgassing on SPEAR I could not have caused any anomalous plasma effects. This is true even for the extreme assumption that the g-10 boom was highly outgassing and responsible for the high neutral pressure gauge readings during flight.

Calculations of SPEAR II external outgassing densities were performed assuming the same outgassing rate for all materials. The value chosen was 0.01 W/m^2 , the maximum ambient rate for hot aluminum. The resultant gas cloud was orders of magnitude less dense than necessary for ionization enhanced sheath currents or for sheath breakdown. The calculated gas cloud surrounding SPEAR II is shown in Figure 10-24. The SPEAR II Plumbrook chamber tests showed no bulk ionization breakdown in the sheath, consistent with the low outgassing densities predicted by the model.

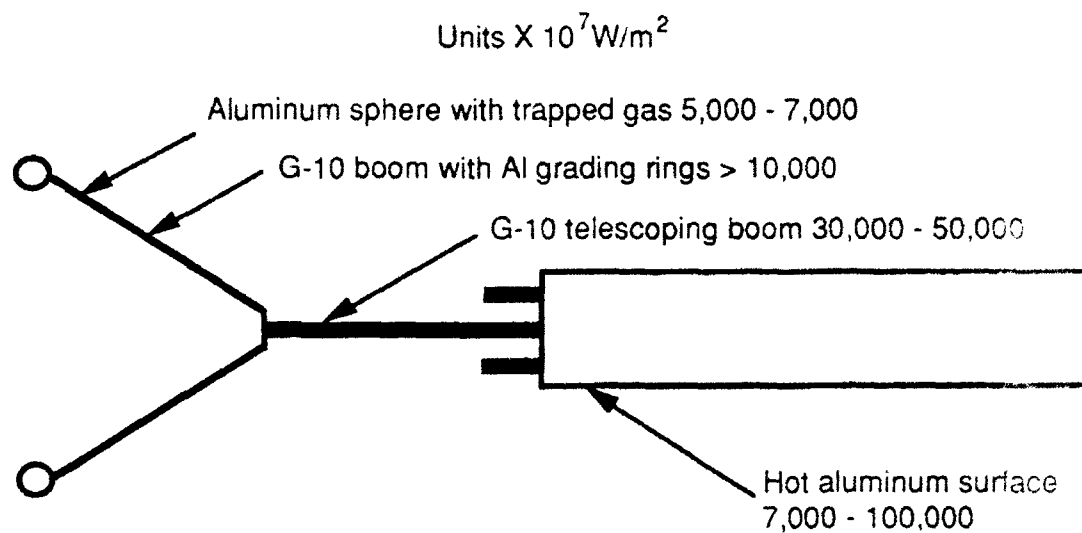


Figure 10-21. Outgassing rates for SPEAR 1 components.

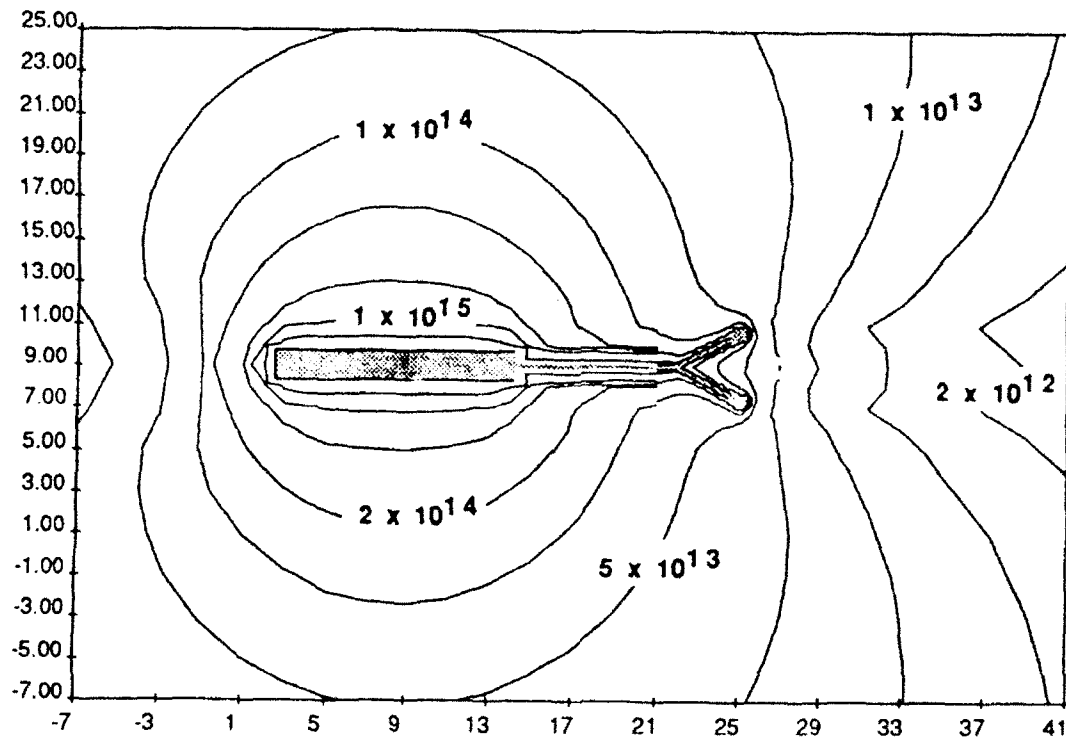


Figure 10-22. Outgassing densities about SPEAR I, taking outgassing rates of $7 \times 10^{-4} \text{ W/m}^2$ for the spheres, 10^{-3} W/m^2 for the bushings, $5 \times 10^{-3} \text{ W/m}^2$ for the booms, and 10^{-2} W/m^2 for the body. These values were provided by Auburn University.

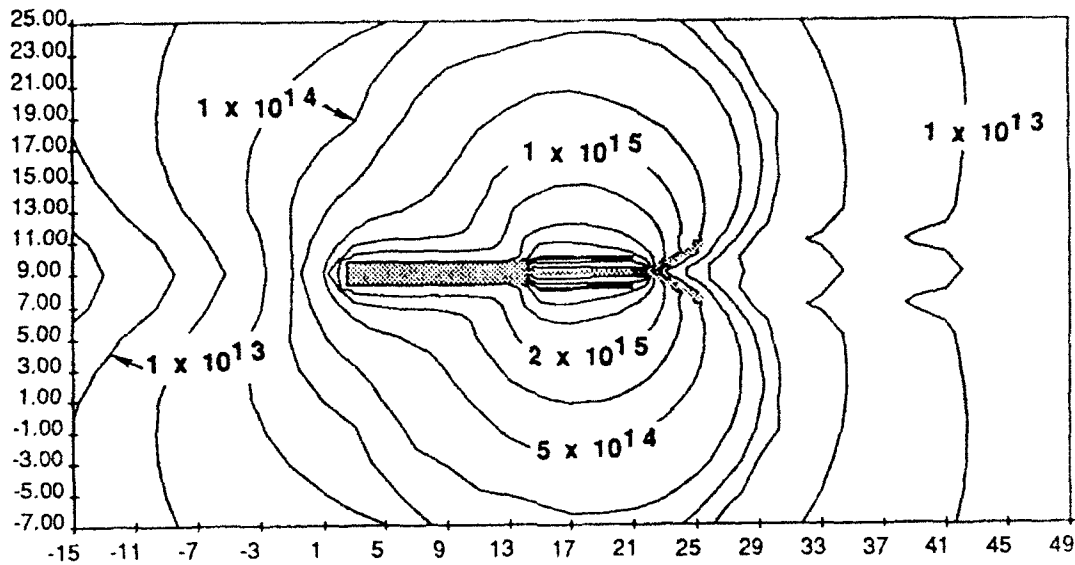


Figure 10-23. Outgassing densities about SPEAR I using elevated G-10 outgassing. Even for this enhanced outgassing and resultant neutral densities, the density in the sphere region is below the sheath ionization thresholds.

See Figure 10-24 on page 116

Figure 10-24. Outgassing densities about SPEAR II using outgassing rates of $.01 \text{ W/m}^2$ for all surfaces.

Summary

The new SPEAR model enables the neutral density due to outgassing, including scattering from the ambient, to be computed quickly making system trade studies practical. The model has been incorporated into the NASCAP/LEO and EPSAT codes for use in engineering design analysis. Calculations using the model show that normal outgassing has little impact on collecting sheaths for the power systems, and that ambient neutral-outgassing scattering is negligible for few meter size systems above 200 km. For SPEAR I the neutral density in the electron collecting sheath due to outgassing was shown to be below breakdown thresholds. This result is consistent with the lack of sheath ionization breakdown during the SPEAR I flight. For SPEAR II, the neutral density in the ion collecting sheaths was shown to be insufficient to cause significant ionization enhancements to the collected current. This is consistent with the Plumbook chamber tests. In Plumbook the observed current collection was in agreement with DynaPAC calculations, implying that only classical phenomena, not ionization, controlled the plasma interaction physics.

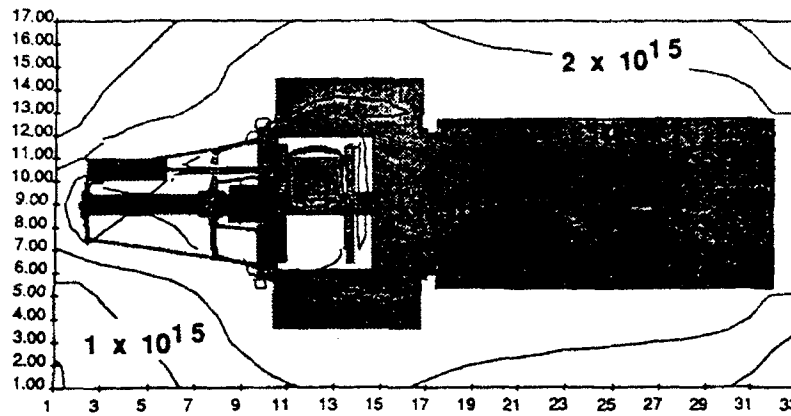


Figure 10-24. Outgassing densities about SPEAR II using outgassing rates of $.01 \text{ W/m}^2$ for all surfaces.

REFERENCES

1. M.J. Mandell, T.T. Luu, J.R. Lilley, Analysis of Dynamical Plasma Interactions with High-Voltage Spacecraft, Interim Report. Maxwell Laboratories/S-Cubed Division, La Jolla, CA, SSS-DPR-90-11973,1990.
2. M.J. Mandell and V.A. Davis, User's Guide to NASCAP/LEO, (Maxwell Laboratories/S-Cubed Division, La Jolla, CA, 1990).
3. I. Katz, M. J. Mandell, G. W. Schnuelle, D. E. Parks, and P. G. Steen, "Plasma Collection by High-Voltage Spacecraft in Low Earth Orbit", *Journal of Spacecraft and Rockets*, 18, 79 (1981).
4. M. J. Mandell, I. Katz and D. L. Cooke, "Potentials on large spacecraft in LEO", *IEEE Trans. Nucl. Sci.* NS-29,1584-1588, 1982.
5. T. Neubert et al., "The sheath structure around a negatively charged rocket payload". *J. Geophys. Res.*, 95, 6155 (1990).
6. M. J. Mandell, J. R. Lilley, and I. Katz, "Computer Modeling of Current Collection by the CHARGE-2 Mother Payload." *Geophys. Res. Lett.* 17,135 (1990).
7. I. Katz, G. A. Jongeward, V. A. Davis, M. J. Mandell, R. A. Kuharski, J. R. Lilley, Jr., W. J. Raitt, D. L. Cooke, R. B. Torbert, G. Larson, and D. Rau, "Structure of the Bipolar Plasma Sheath Generated by SPEAR I," *Journal of Geophysical Research* 94,1450 (1989).
8. M. J. Mandell and I. Katz, "Potentials in a Plasma over a Biased Pinhole," *IEEE Transactions on Nuclear Science* , NS-30, 4307 (1983).
9. M. J. Mandell, I. Katz, G. A. Jongeward, and J. C. Roche, "Computer Simulation of Plasma Electron Collection by PIX-II," *Journal of Spacecraft and Rockets* 23, 512 (1986).
10. PDA Engineering, Inc., Costa Mesa, CA.
11. K.C. Maffei, I. Katz, J.R. Cooper, R.S. Iigermanson, M.J. Mandell, D.E. Parks, A Program for Enhancing the Surface Breakdown Strength of Components and Systems in the Space Environment, (Maxwell Laboratories/S-Cubed Division, SSS-DFR-90-11204, La Jolla, CA,1990).
12. Matra, S.A. Paris, France.

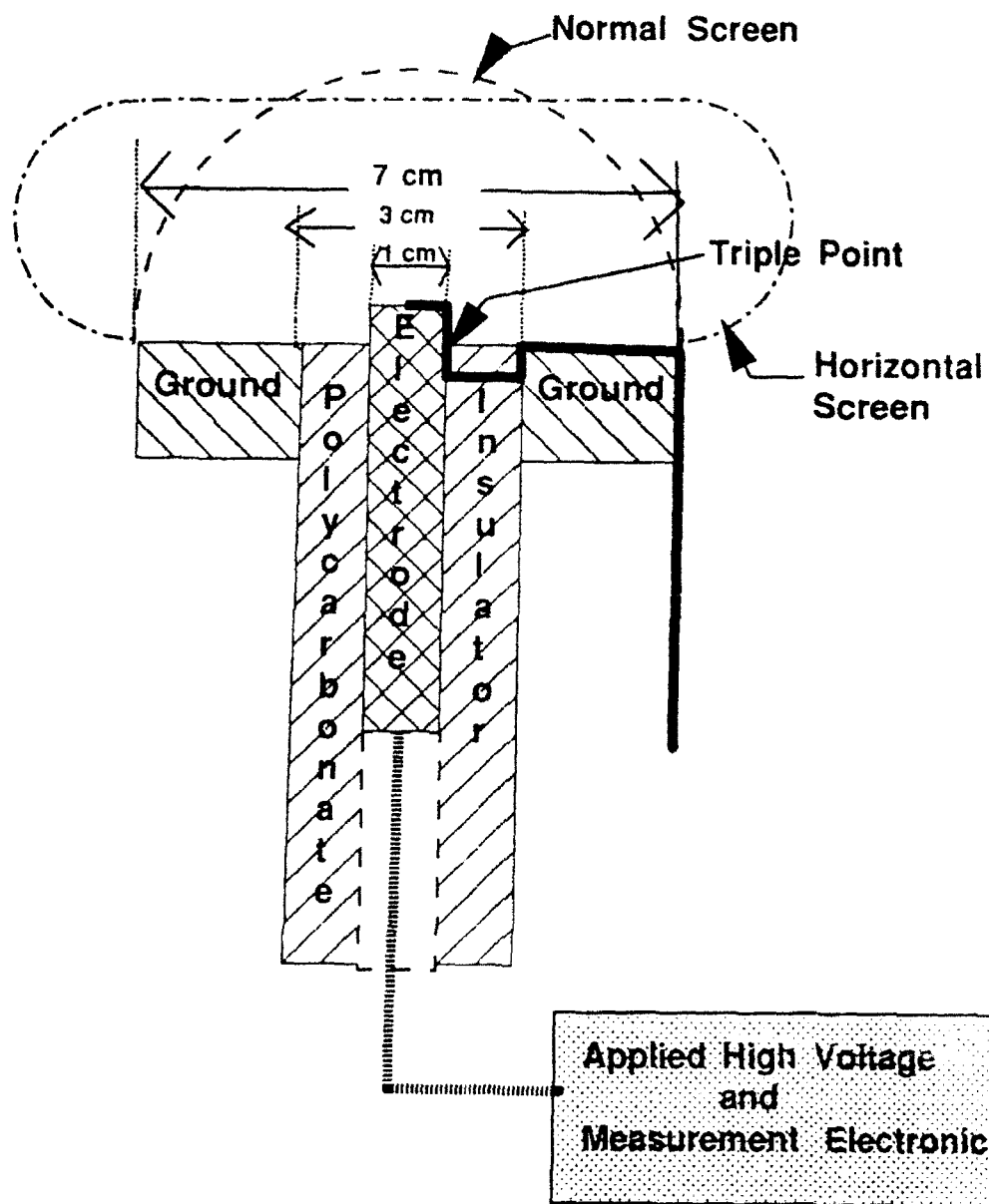
13. American National Standards Institute (ANSI).
14. I. Langmuir and K.B. Blodgett, *Phys. Rev.*, **24**, 49 (1924).
15. L.A. Dietz and J.C. Sheffield, *J. Appl. Phys.*, **46**, 4361 (1975).
16. Gray, Eoin W., Vacuum Surface Flashover: A High-Pressure Phenomenon, *J. Appl. Phys.*, **58**(1) 132, July 1985.
17. Pillai, A. Sivathanu and Reuben Hackam, Surface Flashover fo Solid Dielectric in Vacuum, *J. Appl. Phys.*, **53** (4) 2983, 19???
18. Jongeward, G. A., R. A. Kuharski, E. M. Kennedy, K. G. Wilcox, N. J. Stevens, R. M. Putnam, and J. C. Roche, "The Environment-Power System Analysis Tool Development Program," *Proceedings of the 24th Intersociety Energy Conversion Engineering Conference*, Washington, DC, August 6-11, 1989, p. 371.
19. Hoffman, R. J., and M. A. Hetrick Jr., "Plume Contamination Effects Prediction: CONTAM III Computer Program," *Tech. Rep. AFRPL T752 083*, Air Force Rocket Propul. Lab., Edwards Air Force Base, CA, 1982
20. Rantanen, R. O. and T. D. Gordon, "Contaminant Buildup on Ram Facing Spacecraft Surfaces," *SPIE Paper*, 777-04, May 1987.
21. Melfi, L. T., J. E. Hueser, and F. J. Brock, "Direct Simulation Monte Carlo Technique for Modeling of the Environment in the Vicinity of the Space Shuttle Orbiter," *SPIE Paper*, 286, 1981.
22. Mandell, M. J. and I. Katz, "High Voltage Plasma Interactions Calculations Using NASCAP/LEO," *AIAA Paper*, No. 90-0725.
23. Cooke, D. L., I. Katz, M. J. Mandeli, D. E. Parks, J. R. Lilley, Jr., J. H. Alexander A. G. Rubin, "POLAR Code Development," AFGL-TR-83-0046, *Proceedings of Air Force Geophysics Laboratory Workshop on Natural Charging of Large Space Structures in Near Earth Polar Orbit*, 14-15 September 1982, p. 321, 1983. ADA134894
24. Cooke, D. L. and I. Katz, "Ionization Induced Instability in an Electron Collecting Sheath," *Journal of Spacecraft and Rockets*, Vol. 25, p. 132, 1988.

Comparison Matrix
NASCAP/LEO - Gilbert - DynaPAC

	NASCAP/LEO	Gilbert	DynaPAC
Dimensionality	3-D	2½-D	3-D
Potential Interpolation	TriLinear	BiQuadratic	High Order
Steady-State Sheaths	Yes	Yes	Yes
Generalized Geometry	Yes	Yes	Yes
Time Dependence	No	Yes	Yes
Magnetic Fields	Yes	Yes	Yes
Self-Consistent Sheaths	No	Yes	Yes
Plasma Wakes	Yes	No	Yes
Neutral Ionization	No	Yes	Planned
DataBase Centered	No	No	Yes
User Interface	Good	Good	Best
Development for SPEAR II	Augmented	Augmented	Developed
Validation by SPEAR II	No	Yes	Yes
Extend SPEAR II Results	Yes	Yes	Yes

Note to Editor:

This table is provided for editorial convenience. It does not exist on the disks, and is not called out in the text. It may be conveniently placed in the "Summary of Technical Developments and Capabilities" section at the end of the code portion of the chapter.



8. SIMPLE CALCULATIONS FOR THE BREAKDOWN OF A NEGATIVE SHEATH

This work appeared in the Quarterly Report for 1 January through 31 March 1991.

8. IONIZATION CALCULATIONS

Ionization breakdown for negative potentials takes place according to the following mechanism:

1. An electron emitted from the probe surface creates Γ ions as it is accelerated into space;
2. The collection of those ions results in emission of $\gamma\Gamma$ electrons.

We have breakdown for $\gamma\Gamma > 1$. More precisely, the current amplification factor for a "seed ion" is $1 + \gamma_0 (1 + \Gamma)/(1 - \gamma\Gamma)$, where γ_0 is the secondary yield for the seed ion. Note that:

1. Γ is a function of the potential distribution $V(r)$, the neutral density distribution $N_0 f(r)$, and the ionization cross-section $\sigma(E)$.
2. γ is a function of the distribution of potentials at which ions are created.

One-dimensional calculations have been done under the following assumptions:

1. The probe is represented by a sphere of radius $R = 0.64$ meters (hopefully, an adequate representation of the SPEAR I rocket body).
2. The ionization cross-section is that for electron impact ionization of N_2 .
3. The potential is a confined coulomb potential:

$$V(r) = V_0 (R R_{LB}/r - R)/(R_{LB} - R)$$

where R_{LB} is the Langmuir-Blodgett radius for a plasma of density 10^{11} and temperature 0.1 eV.

4. The neutral density function is $f(r) = 1$ or $f(r) = (R/r)^2$.

5. The secondary yield is

$$\gamma_0(v) = \text{Max}[0.05, 2.4 \times 10^{-5}(v - 5.5 \times 10^4)]$$

where v is the ion incident velocity.

6. Ions and electrons are created with zero energy and with no energy loss to the primary.

The results turn out to be only a little bit nonlinear. Here they are:

V_0	R_{LB}	$t(r)$	γ	Γ	Breakdown N_0
-1000	3.3	1	$0.84 + 7.5 \times 10^{-21} N_0$	$3.6 \times 10^{-20} N_0 + 1.1 \times 10^{-39} N_0^2$	17×10^{18}
-10,000	8.1	1	$5.68 + 4.5 \times 10^{-20} N_0$	$1.9 \times 10^{-20} N_0 + 1.1 \times 10^{-39} N_0^2$	7×10^{18}
-50,000	15.6	1	$15.3 + 1.0 \times 10^{-19} N_0$	$1.1 \times 10^{-20} N_0 + 8.9 \times 10^{-40} N_0^2$	4×10^{18}
-1000	3.3	$(R/r)^2$	$0.435 + 7.5 \times 10^{-21} N_0$	$9.3 \times 10^{-21} N_0 + 6.7 \times 10^{-41} N_0^2$	1.0×10^{20}
-10,000	8.1	$(R/r)^2$	$2.72 + 4.5 \times 10^{-20} N_0$	$3.1 \times 10^{-21} N_0 + 8.8 \times 10^{-42} N_0^2$	0.8×10^{20}
-50,000	15.6	$(R/r)^2$	$7.44 + 1.0 \times 10^{-19} N_0$	$1.0 \times 10^{-21} N_0 + 1.2 \times 10^{-42} N_0^2$	1.1×10^{20}

A few additional comments:

1. For the $(R/r)^2$ density, all the ion production takes place within about two meters of the probe (except for the -1000 volt case).
2. For constant density, as breakdown is approached, we get increasing ionization at the outer boundary.
3. When we exceed about half the breakdown density, we get order-of-magnitude current enhancement.
4. Breakdown develops on an ion transit timescale, which would be tens of microseconds. Accumulated ions will sharpen the potential during this process, reducing Γ from what we have calculated, and leading to a higher breakdown density.
5. In positive potential breakdown, the accumulated ions force trapping of additional electrons to balance their charge. For negative potential

breakdown at threshold, the electron density is negligible and the retained ions tend to suppress breakdown by causing electrons to be accelerated beyond the energy for maximum cross-section more quickly.

6. Calculations can proceed on an ion timescale by generating the entire ionization track of a secondary electron each time an ion strikes the probe. This approach is valid as long as

$$(1/Q)(dQ/dt) \gg 1/\tau_e$$

where Q is the ion content of the grid, and τ_e is the time for an ionization-produced electron (not a secondary electron) to leave the grid. That is, the density must be near the breakdown threshold rather than well above it.

9. SPEAR-3 SHEATH STRUCTURE AND PLASMA CURRENTS

This work appeared in the Quarterly Report for 1 April through 30 June 1991

9. SPEAR III CALCULATIONS FOR PDR

DynaPAC was used to calculate sheath structure and plasma currents for the SPEAR III preliminary design review, Logan, Utah, 12-14 June, 1991. A PATRAN model was constructed having the correct rocket dimensions. Half the gradings were removed from the boom, as had been suggested by the mechanical engineers. As the boom angle was not decided at the kickoff meeting, it was set to approximately 45 degrees. The model is shown in figure 9.1.

Steady-state calculations were done for sphere biases of 5 kilovolts and 20 kilovolts and several rocket potentials for each case. The plasma was taken as O^+ with density $1 \times 10^{11} \text{ m}^{-3}$ and temperature 0.1 eV and the magnetic field was 0.4 gauss. Figures 9.2 show potentials calculated for 20 kilovolt sphere bias, and figures 9.3 show potentials calculated for 5 kilovolt sphere bias.

Tables 9.1 and 9.2 show the calculated electron and ion currents. Ion currents were calculated using the usual sheath method, and no problems were encountered except for the two cases when the sheath filled the grid. Figure 9.4 shows ion trajectories for the case of 20 kilovolt bias and negative 4 kilovolt rocket potential. We also added the ObjPot1 the capability of plotting cell currents and surface current densities. These are shown (for the same case) in figures 9.5. Peak ion current of about 0.7 milliamperes per square meter occurs near the middle of the rocket and opposite the sphere. The high-voltage section (top section) of the rocket is shielded from ion current by the positive sheath, particularly on the side toward the sphere.

Table 9.1 Current (milliamperes) results for SPEAR III with magnetic field normal to rocket-boom plane.

Sphere	Body	Electron Current FieldLine Method			Ion Current	Secondary Electrons	Total
Potential	Potential	Sphere	Boom	Trapped			
19.5 kV	-0.5 kV	-7.1	-5.1	60.	0.6	0.3	-11.1
18.0 kV	-2.0 kV	-11.0	-8.3	?	1.4	3.3	-14.6
16.0 kV	-4.0 kV	-8.7	-5.4	-9.0	1.8	7.1	-5.2
14.0 kV	-6.0 kV	-4.3	-2.7	4.5	2.2	11.3	6.5
12.0 kV	-8.0 kV	5.5	-1.8	-6.9	2.5	15.3	10.5
5000 V	0V	-4.2	-4.0	-9.2	0.03	0	-8.2
4500 V	-500 V	-2.7	-3.2	-9.7	0.3	0.2	-5.4
4000 V	-1000 V	-3.0	-1.6	-9.1	0.8	1.1	-2.7
3500 V	-1500 V	-5.1	-2.4	-4.6	1.0	1.9	-4.6
2500 V	-2500 V	-5.9	-1.7	-0.7	>1.3	>3.7	> -2.3
2000 V	-3000 V	-5.9	-1.0	-0.2	>1.3	>4.2	> -1.3

Table 9.2 Current (milliamperes) results for SPEAR III with magnetic field along boom.

Sphere	Body	Electron Current FieldLine Method			Ion Current	Secondary Electrons	Total
Potential	Potential	Sphere	Boom	Trapped			
9.5 kV	-0.5 kV	-3.0	-0.6	?	0.6	0.3	-1.5
18.0 kV	-2.0 kV	-2.4	0	?	1.4	3.4	2.4
16.0 kV	-4.0 kV	-2.3	-0.4	-15.6	1.8	7.1	6.2
14.0 kV	-6.0 kV	-2.4	0	?	2.2	11.3	11.1
12.0 kV	-8.0 kV	-2.4	-0	?	2.5	15.3	15.4
5000 V	0 V	-2.9	-0.1	-30.2	0.03	0	-3.0
4500 V	-500 V	-2.0	-0.1	-23.8	0.3	0.2	-1.6
4000 V	1000 V	1.3	-0.02	-18.1	0.8	1.1	0.6
3500 V	-1500 V	-1.1	-0.06	-11.2	1.0	1.9	1.7
3000 V	-2000 V	-1.1	-0.1	-8.2	1.2	2.9	2.9
2500 V	-2500 V	-1.3	-0.2	-4.6	>1.3	>3.7	>3.5
2000 V	-3000 V	-1.5	0	-3.2	>1.3	>4.2	>4.0

Electron currents to the sphere and boom proved difficult to calculate. The sheath method gave implausible results and trajectories, particularly for cases where the potential was not extremely well converged. This is due in part to unphysical initial conditions given electrons started by the sheath method. Eventually, we elected to follow electrons along field lines from the computational boundary. This had the disadvantage in that a lot of effort went into tracking electrons through electric-field-free regions but had the nice properties that trapped, as well as collected, currents that could be calculated, and they did not depend (within reason) on the initial particle energy. (Electrons were considered quasi-trapped if they survived after three grid-index loops.) Figure 9.6 shows trajectories for electrons emitted along the line $Z=1$, $X=8.5$ and shows examples of unperturbed, quasi-trapped, and collected electrons.

The electron currents, as expected, were very different between the cases that the magnetic field was (1) normal to the boom-rocket plane or (2) along the boom. In the first case, collected currents were somewhat in excess of the Parker-Murphy limit, with comparable currents collected by the boom and the sphere, and the quasi-trapped current was relatively small. In the second case, the sphere collected well under the Parker-Murphy limit, the boom collected negligible current, and the quasi-trapped current was very high.

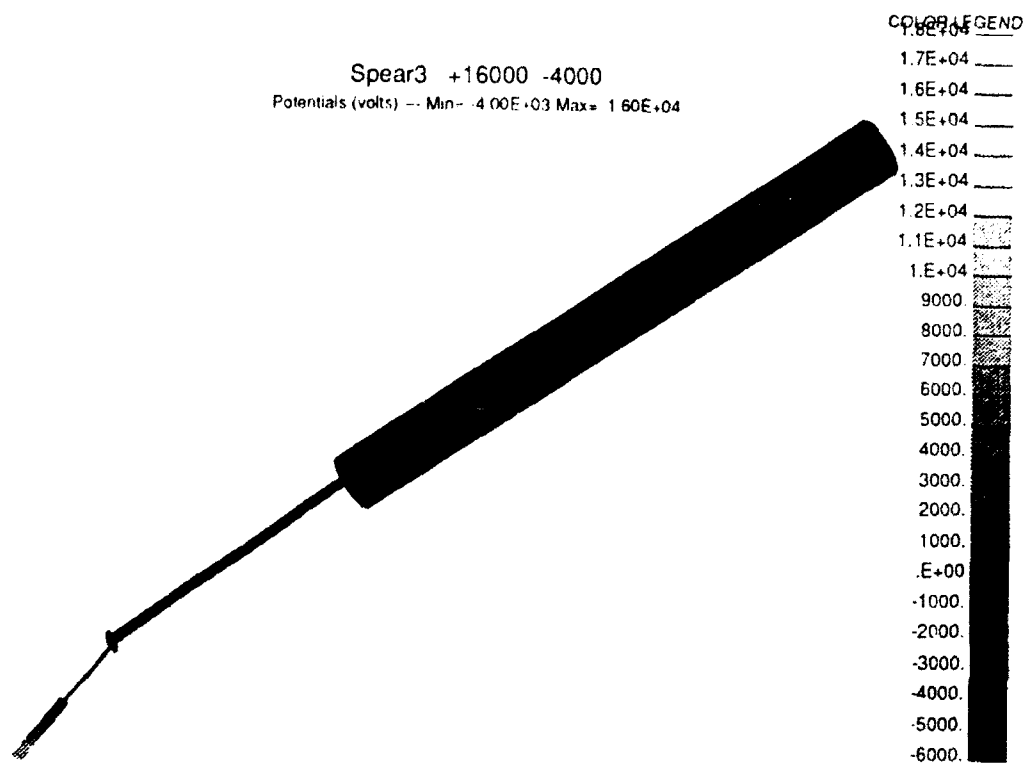
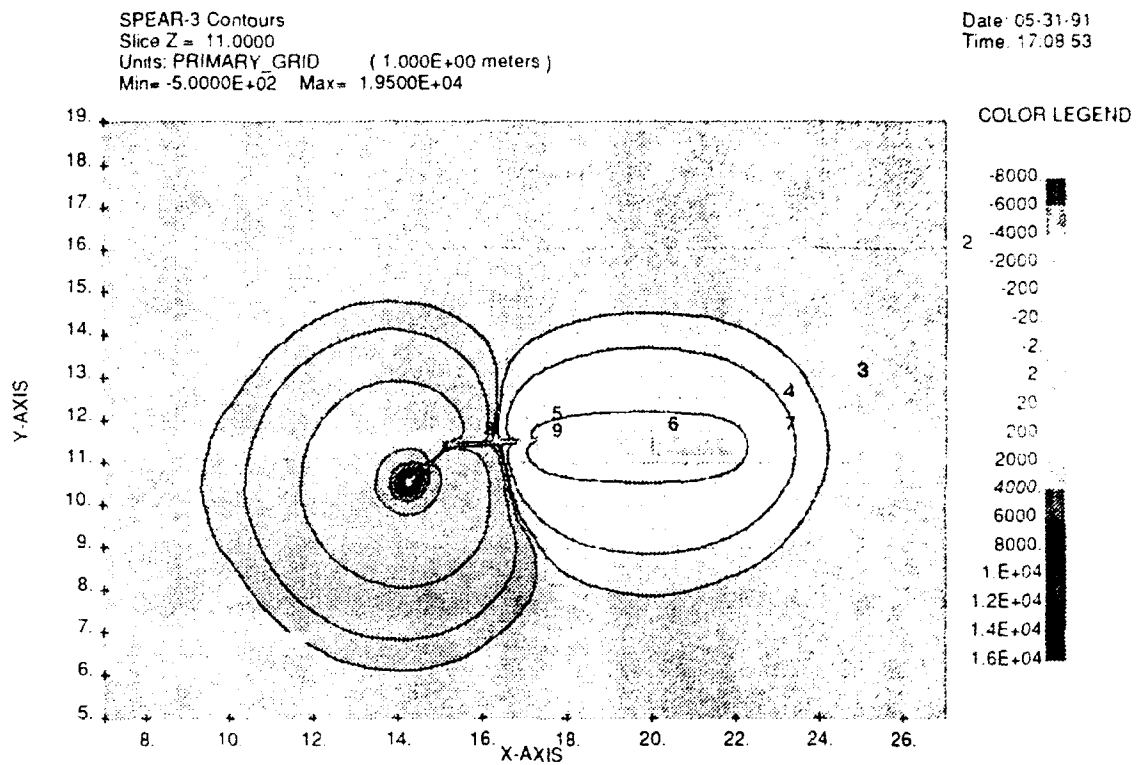


Figure 9.1 SPEAR III model for PDR, with boom at approximately 45 degrees.

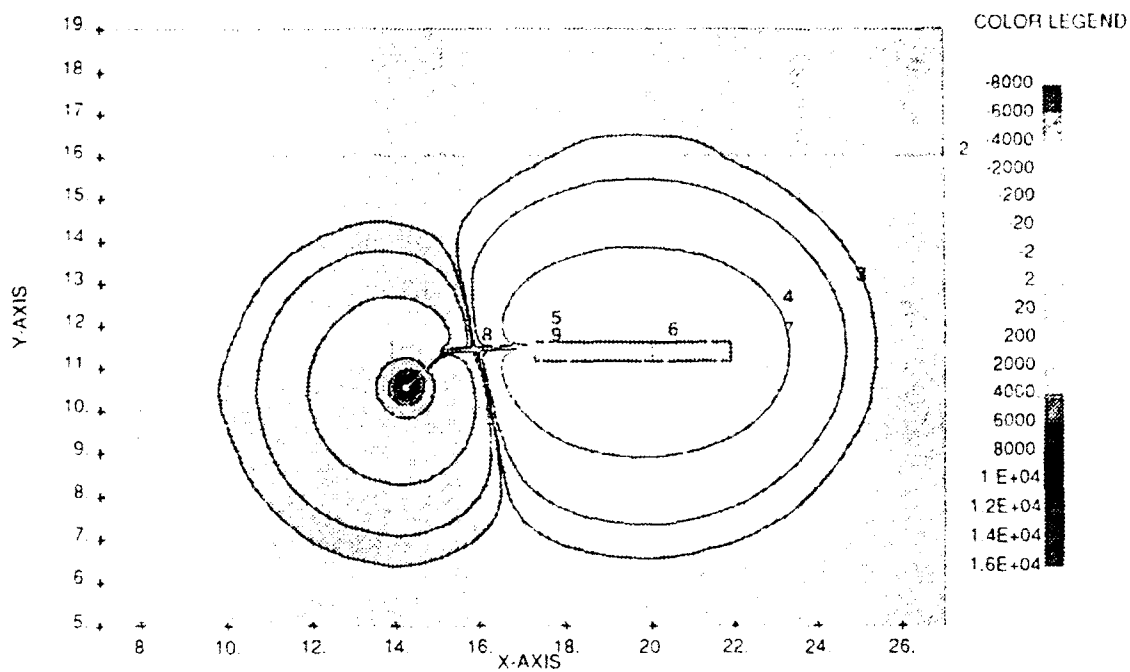


(a)

Figure 9.2 SPEAR III sheath contours for 20 kilovolt bias and rocket body at
 (a) -500 volts; (b) -2000 volts; (c) -4000 volts; (d) -6000 volts.

SPEAR 3 Contours
 Slice Z = 11.0000
 Units: PRIMARY GRID (1.000E+00 meters)
 Min = -2.0000E+03 Max = 1.8000E+04

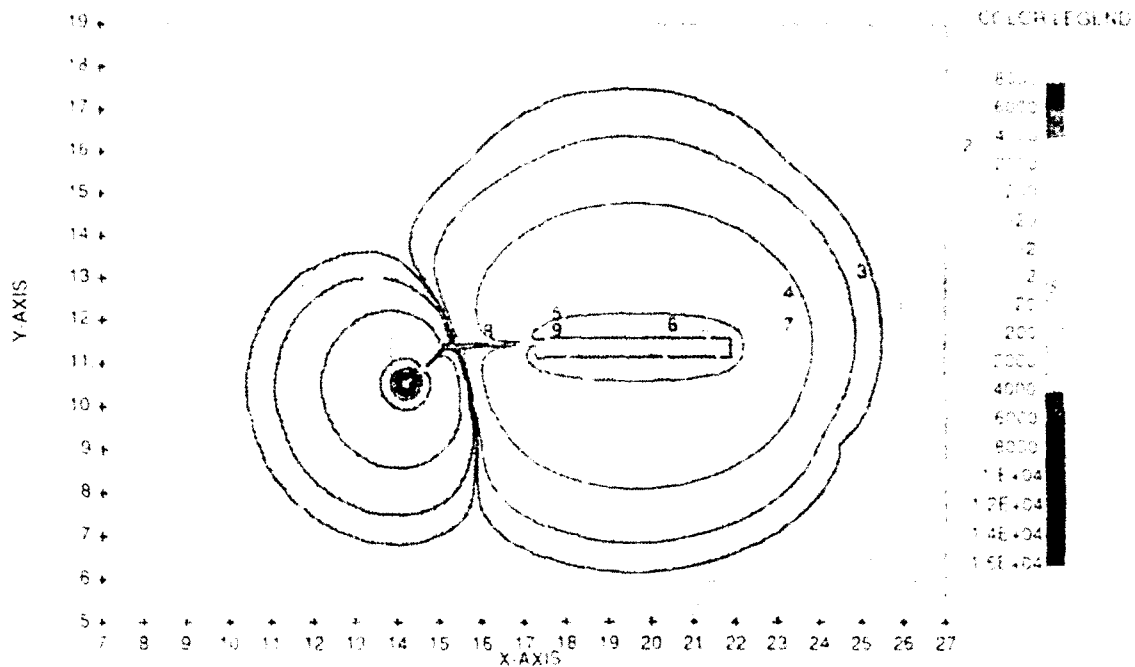
Date: 05/30/91
 Time: 15:53:18



(b)

GREAR 3 Contours
 Slice Z = 12.000
 Units: PRIMARY: GRIL 1.001E+00 meters
 Min: -4.000E+03 Max: 1.000E+04

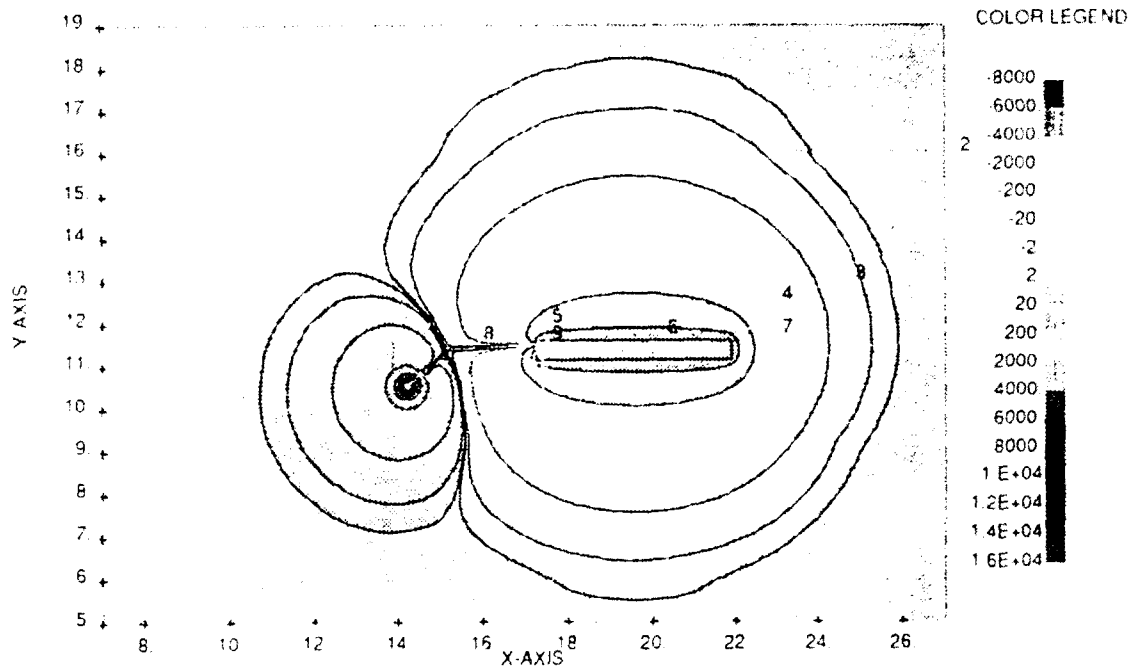
Date: 01-29-91
 Time: 16:47:56



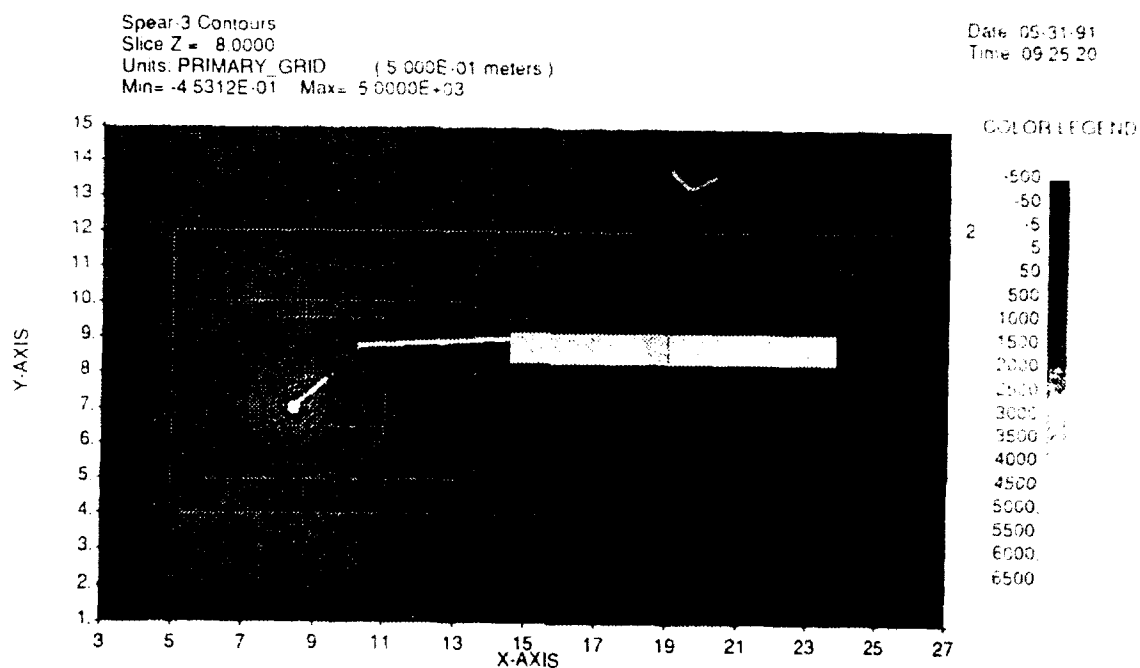
(C)

SPEAR-3 Contours
 Slice Z = 11.0000
 Units: PRIMARY GRID (1.000E+03 meters)
 Min = -6.0000E+03 Max = 1.4000E+04

Date 05-31-91
 Time 09:55:22



(d)

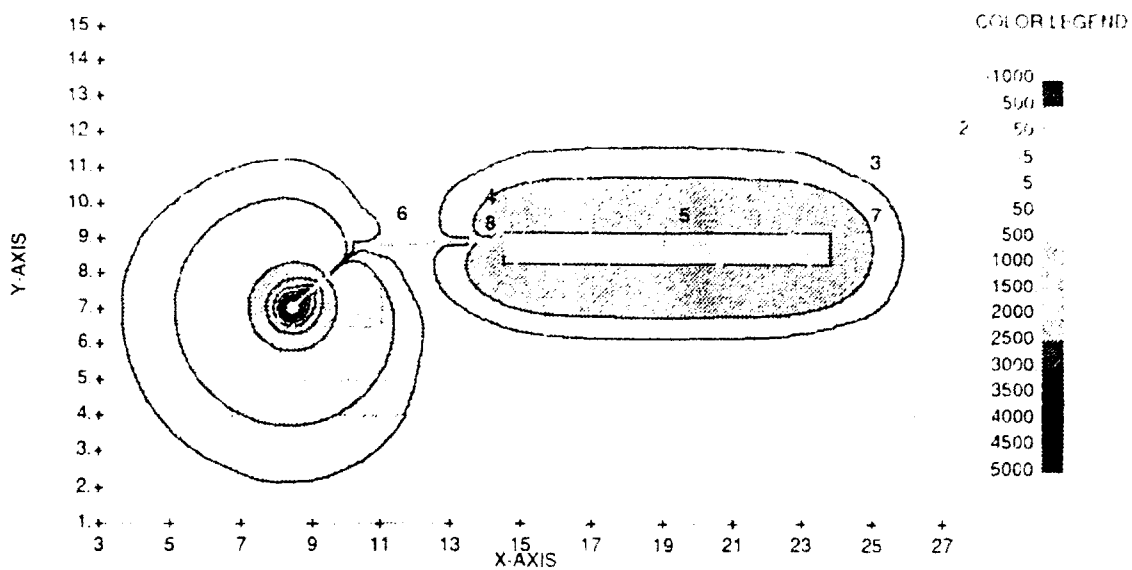


(a)

Figure 9.3 SPEAR III sheath contours for 5 kilovolt bias and rocket body at (a) zero; (b) -500 volts; (c) -1000 volts; (d) -1500 volts.

Spear: 3 4500 - m500
 Slice Z = 8 0000
 Units: PRIMARY_GRID (5 000E-01 meters)
 Min = -5 0000E+02 Max = 4 5000E+03

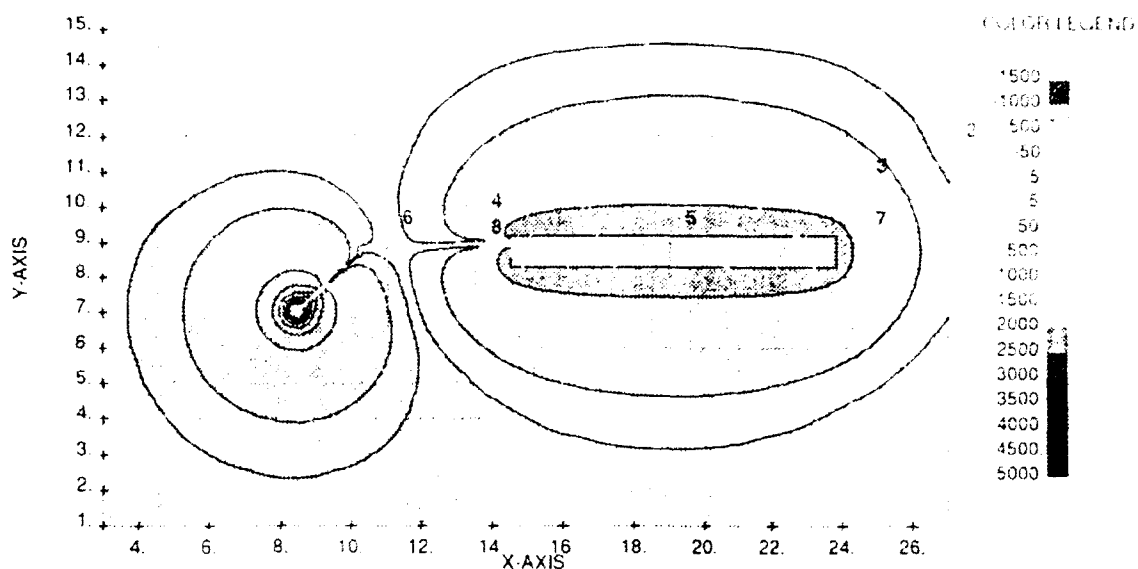
Date 05/28/91
 Time 16:01:40



(b)

Spear3 - 4000 - m1000
 Slice Z = 8 0000
 Units: PRIMARY_GRID (5.000E+01 meters)
 Min = -1.0000E+03 Max = 4.0000E+03

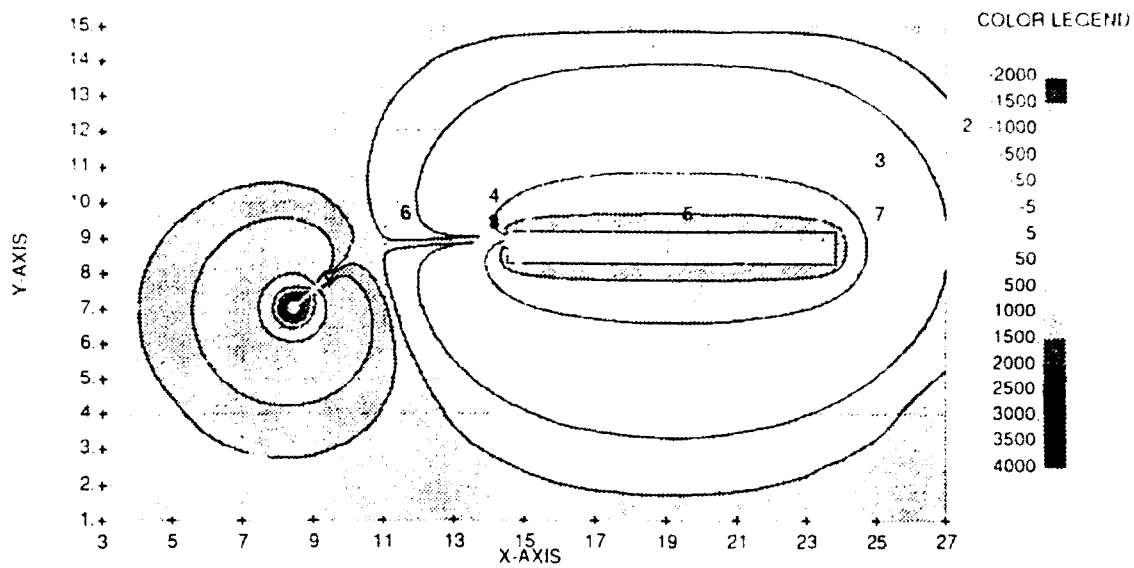
Date: 05/31/91
 Time: 09:27:31



(c)

Spear: 3 - 2500 m1500
 Slice Z = 8 0000
 Units: PRIMARY GRID (5 000E-01 meters)
 Min = -1 500E+03 Max = 3 500E+03

Date 05-30-91
 Time 11:26:15



(d)

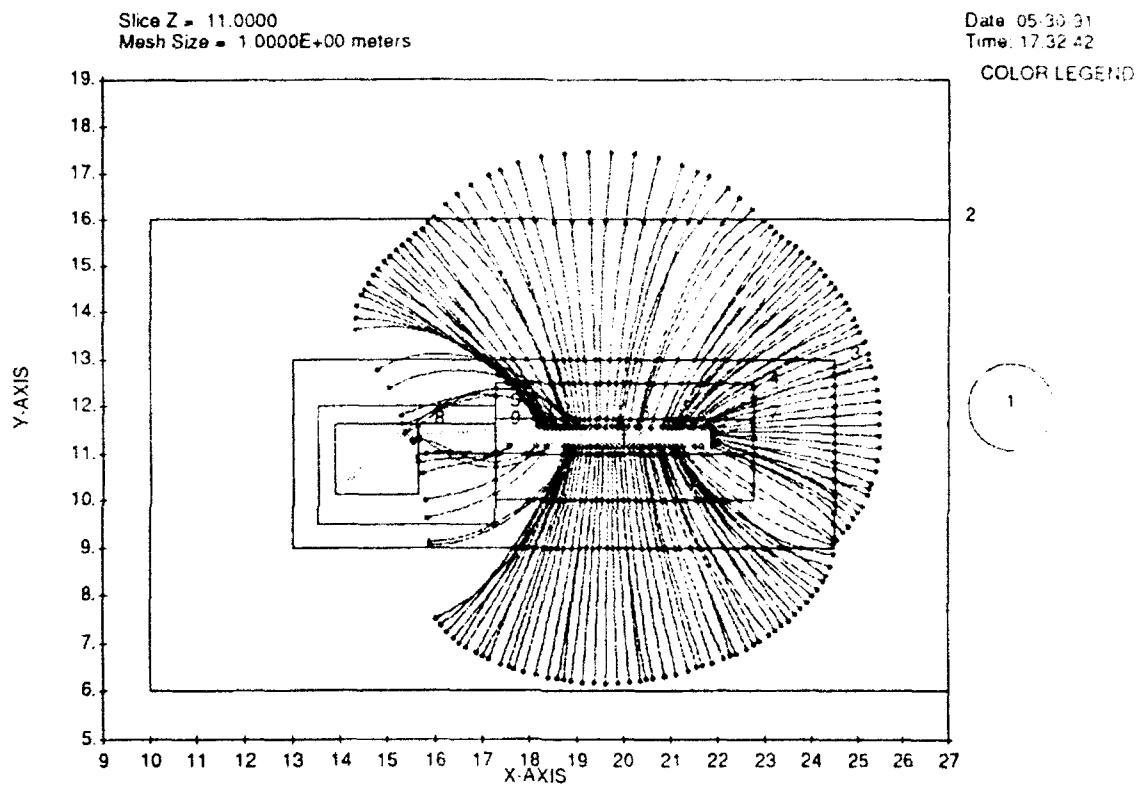
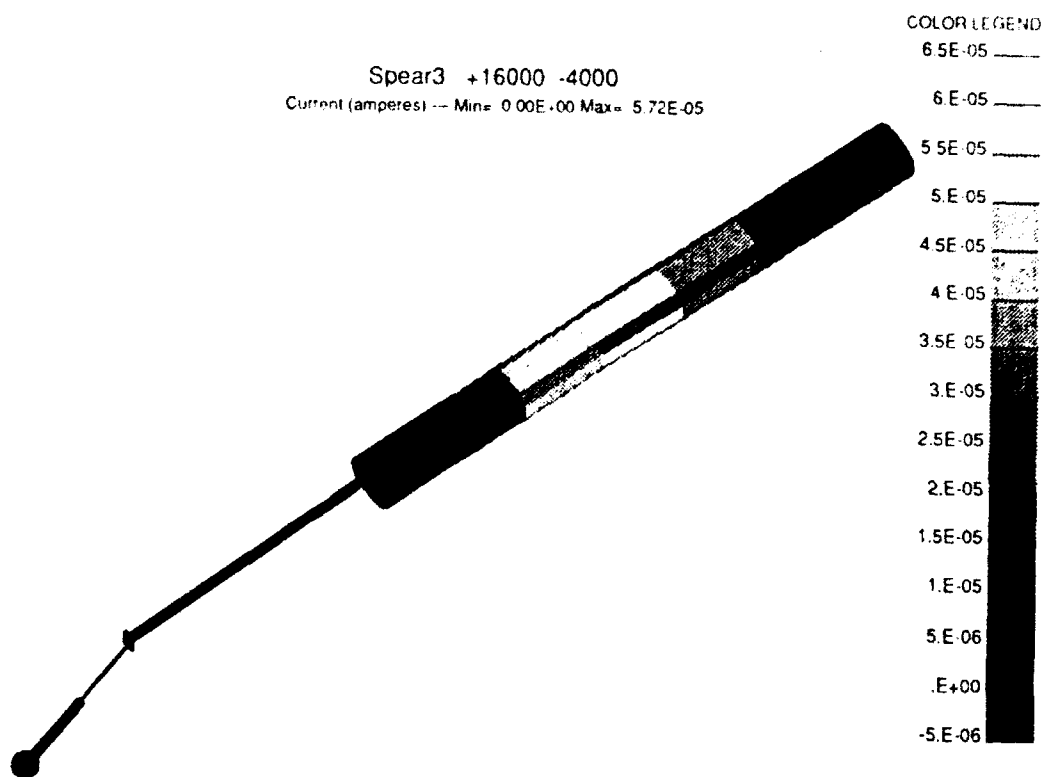
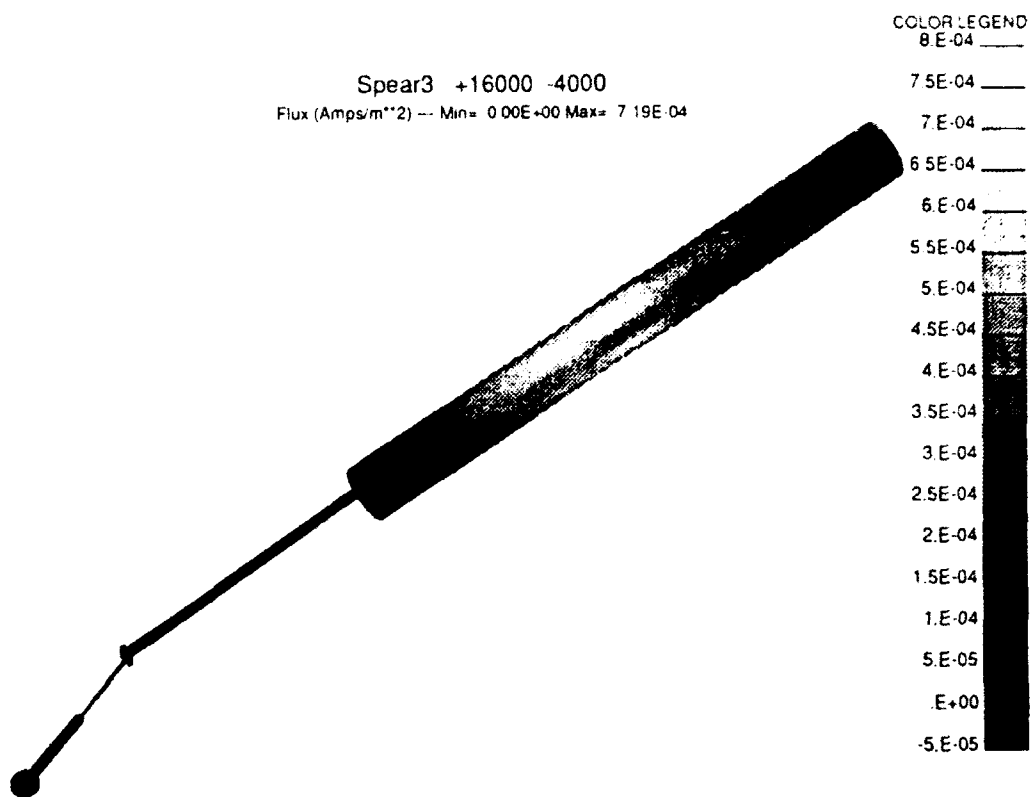


Figure 9.4 Sheath ion trajectories in potential of figure 9.2(c).



(a)

Figure 9.5 ObjPot1 surface ion current plots for case of figure 9.4 and 9.2(c):
(a) surface cell currents; (b) surface current densities.



(b)

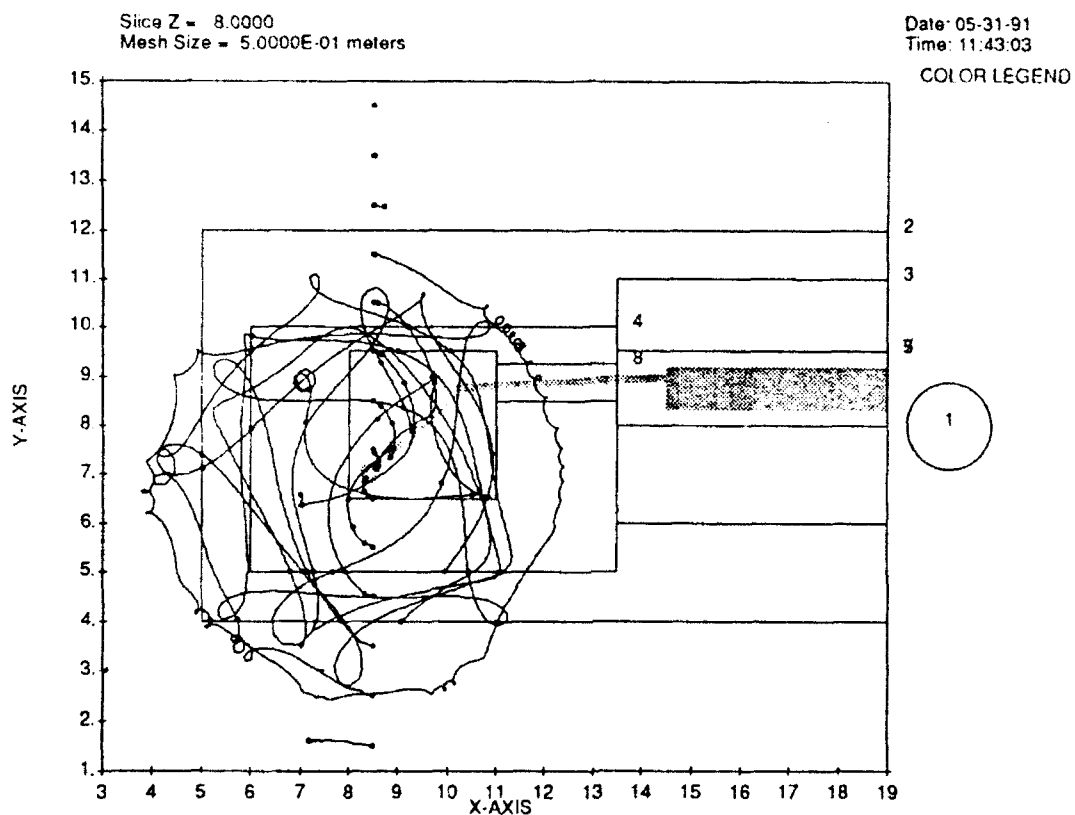


Figure 9.6 Electron trajectories for potential of figure 9.2(c) and magnetic field of 0.4 gauss along Z axis. Electrons are emitted along field lines from computational boundary at Z=1, X=8.5.

10. SPEAR-3 CALCULATIONS FOR PARTICLE DETECTOR PLACEMENT

This work appeared in the Quarterly Report for 1 April through 30 June 1991.

10. SPEAR III CALCULATIONS FOR PARTICLE DETECTOR PLACEMENT

Following the SPEAR III PDR, we were requested to do calculations to assist in determining the placement, view angle, and angular aperture of the ion detectors. As the strawman configuration had changed to a right-angle boom, a new model was generated and gridding was improved to be suitable for any bias in the range of interest.

We performed calculations for the angular distribution of incident ions for three representative sheath configurations. We recommended that if the ion detector(s) are located on Science-1, that they be located on the side away from the sphere and be aimed upward to a degree depending on their precise location.

The three potential conditions were:

1. 16 kV bias, body at -4 kV.
2. 16 kV bias, body at -500 volts.
3. 5 kV bias, body at -2500 volts.

The plasma density and temperature were $2 \times 10^{11} \text{ m}^{-3}$ and 0.1 eV, respectively. A packet of plots was generated for each condition. Figures 10.1 refer to condition 1, figures 10.2 to condition 2, and figures 10.3 to condition 3.

The calculations were done in three ways:

1. The rocket was taken to be a cylinder with the boom and sphere ignored. The Gilbert code was used to make 2-dimensional (R-Z) potential and trajectory calculations. Results are included as line plots (angle vs. inches) in the figures for conditions (1) and (2).

2. Particles were tracked inward from the sheath to the rocket using DynaPAC. These calculations were done in the plane of the potential plots. Each packet contains a particle trajectory plot and an angle vs. inches plot with circles and (barely visible) crosses. The circles are results for the side of the rocket opposite the sphere and the crosses for the side toward the sphere. This method is particularly useful in determining which regions of the rocket receive no incident ions.

3. Particles were tracked outward from proposed detector locations 12 inches from either end of Science-1. The results are summarized in table 10.1. Each set of figures contains two trajectory plots for each of the two locations. Trajectories that escape the sheath represent possible incident ion trajectories; trajectories that reimpact the rocket do not. The trajectory plot in the plane of the potentials shows incident ions arriving at a narrow range of angles. The central trajectory was rotated about a line through the detector parallel to the rocket axis, showing that the range of azimuthal angles is relatively large.

Table 10.1

DynaPAC reverse tracking results for ion detector angle. Detector locations are on Science-1, on side of rocket opposite right-angle boom, with location in inches as indicated in distributed drawings. Locations are 12 inches above bottom of Science-1 and 12 inches below top of Science-1. Angle θ is angle from normal to rocket toward nose. Angle ϕ is rotation from normal to rocket about a line on surface parallel to rocket axis. The \pm angles are not errors but are our computational estimates of the angular spread of the beam. They are in reasonable agreement with our analytic estimates.

Sphere Bias	Body Potential	Detector Location	θ (deg.)	ϕ (deg.)
16 kV	-4 kV	136	11 ± 2	0 ± 13
16 kV	-4 kV	160	2 ± 1	0 ± 15
16 kV	-500 V	136	5 ± 2	0 ± 25
16 kV	-500 V	160	2 ± 1	0 ± 30
5 kV	-2500 V	136	8 ± 1	0 ± 8
5 kV	-2500 V	160	3 ± 1	0 ± 8

The three computational methods are in good agreement. Detectors on Science-1 should be located on the side of the rocket away from the sphere. The incident angle increases with distance from the rocket center (roughly the bottom of Science 1). The rate of increase is about 0.1 degrees per inch with the rocket at -500 volts and about 0.3 degrees per inch with the rocket at -4000 volts. An additional Gilbert calculation (figure 10.4) indicates that the angle does not increase too much further for a very negative (-12 kV) rocket. A detector on the sphere side will have data dropout when the sphere is at high potential, and a 90 degree location has a high risk of data dropout. A 15° aperture detector near the bottom of Science-1 should cover the range -5° to +10° upwards. Near the top it should cover +5° to +20°. Azimuthally, the detector should be aimed straight outward. We would expect such a detector to receive essentially the entire incident ion flux to its active area.

It is interesting that the azimuthal angle range for the 16 kV bias, -500 volt rocket case appears anomalously large. A contour plot (included in figure 10.2) normal to the rocket axis at the level where incident ions enter the sheath shows that the influence of the positive sphere makes the ion collecting sheath more nearly concentric with the detector location than with the rocket axis, explaining the large range of azimuthal angles.

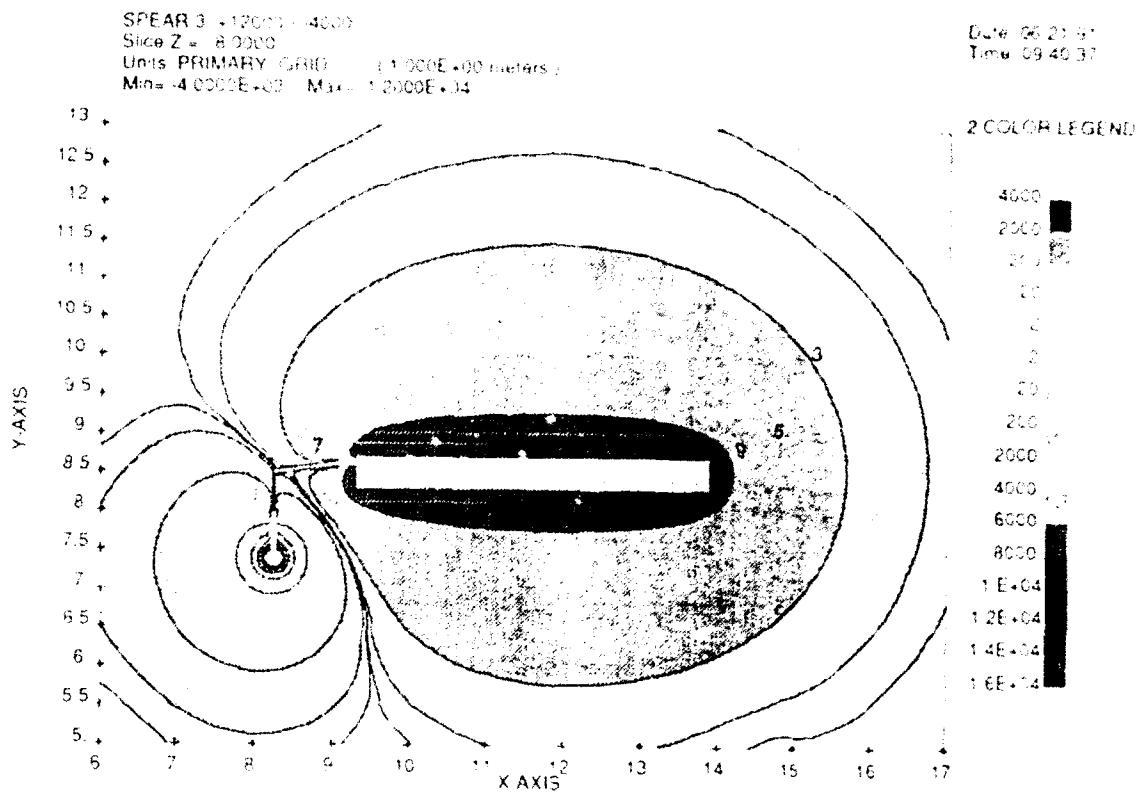


Figure 10.1(a) SPEAR III potentials for right-angle boom, 20 kilovolt bias, -4 kilovolt rocket.

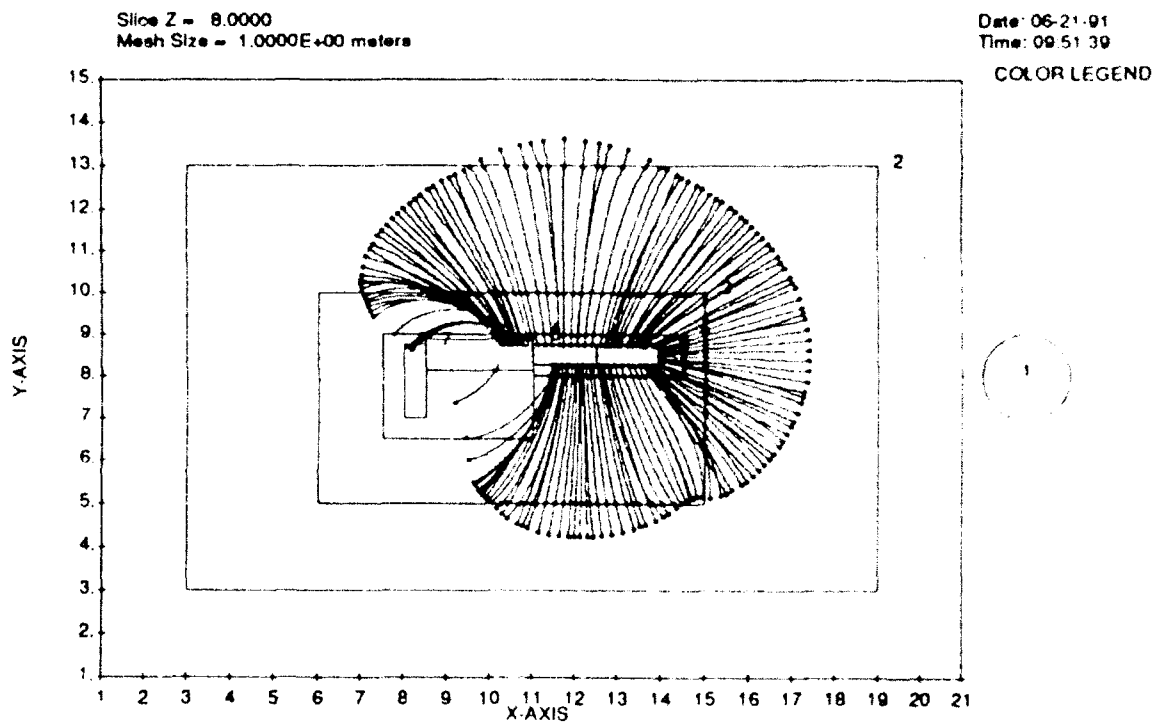


Figure 10.1(b) Ion trajectories in the potentials of figure 10.1(a).

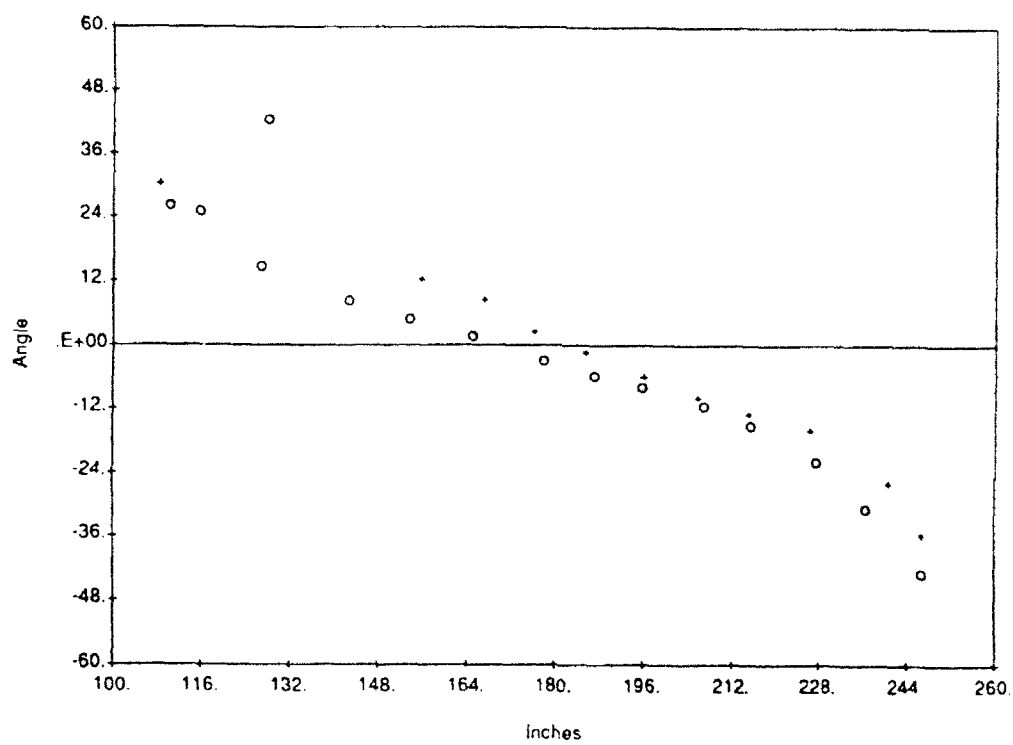


Figure 10.1(c) Incident angle for ions vs. detector position. Circles are for side opposite sphere, crosses for side toward sphere.

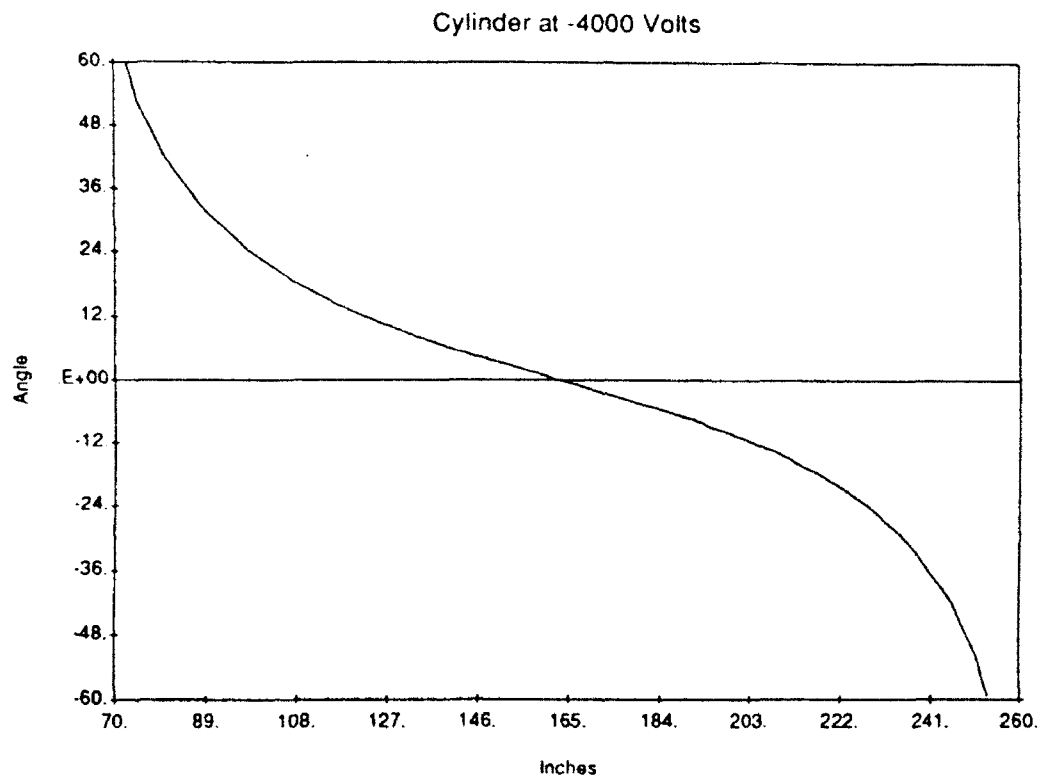


Figure 10.1(d) Gilbert results (for biased cylinder) corresponding to figure 10.1(c).

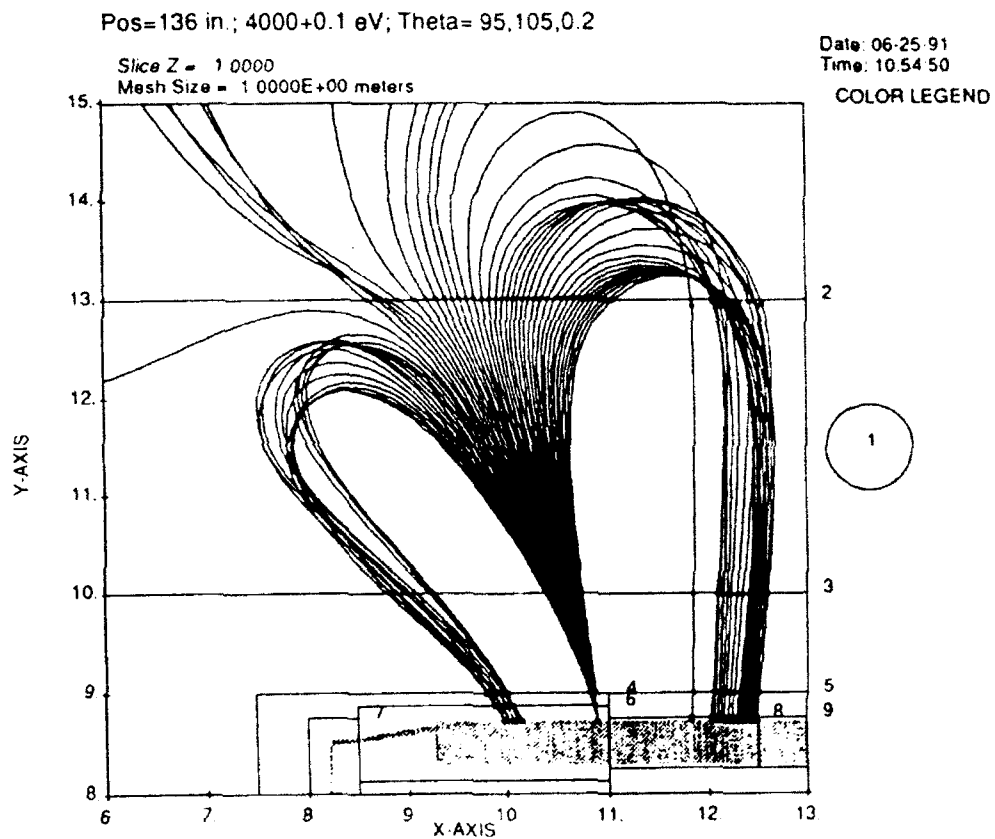


Figure 10.1(e) DynaPAC reverse trajectory calculation for ion detector near top of Science-1.

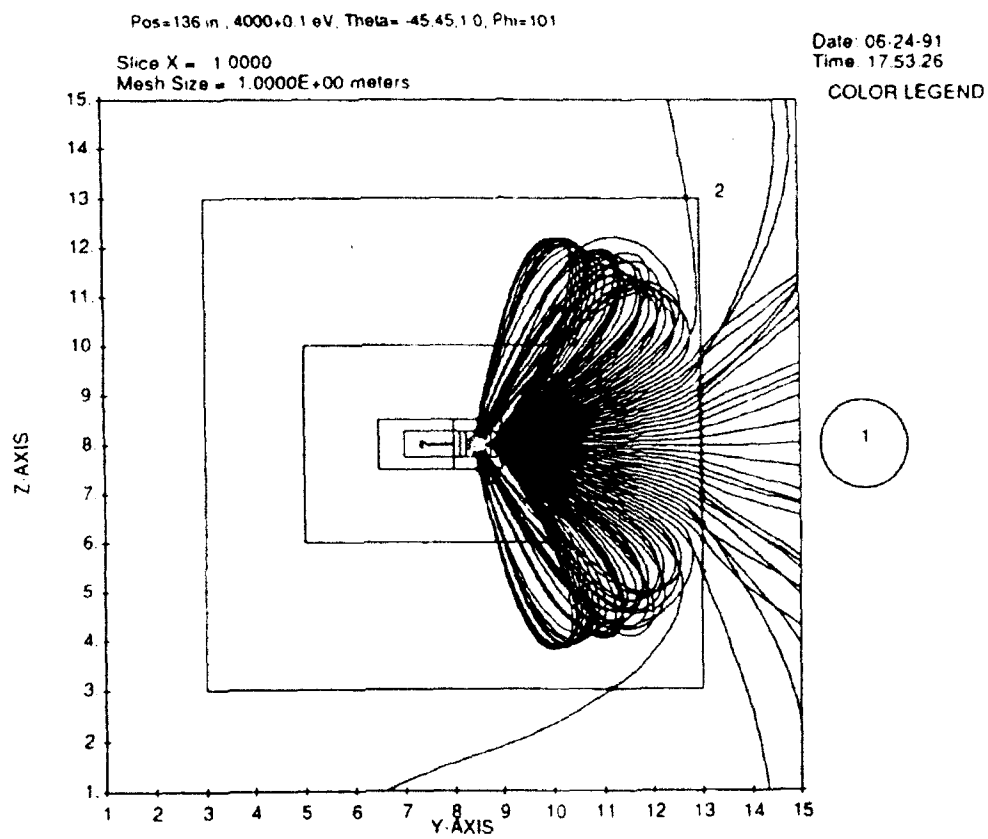


Figure 10.1(f) DynaPAC reverse trajectory calculation for azimuthal angle range corresponding to figure 10.1(e).

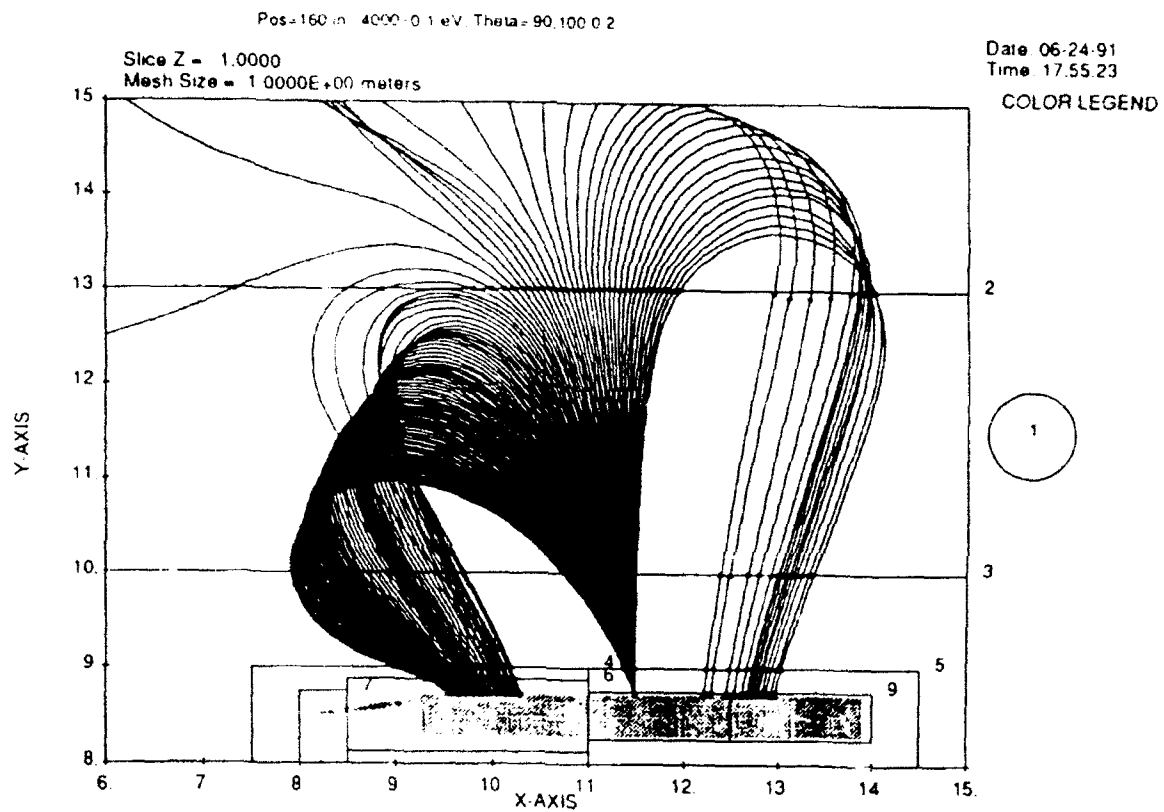


Figure 10.1(g) DynaPAC reverse trajectory calculation for ion detector near bottom of Science-1.

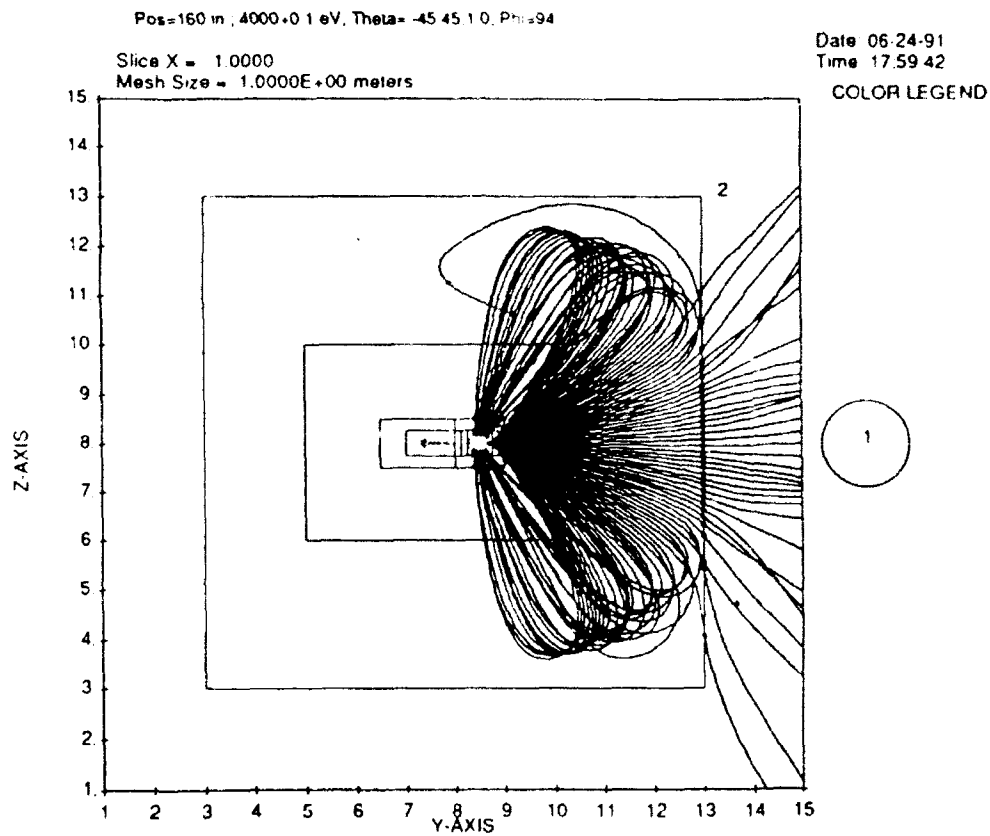


Figure 10.1(h) DynaPAC reverse trajectory calculation for azimuthal angle range corresponding to figure 10.1(g).

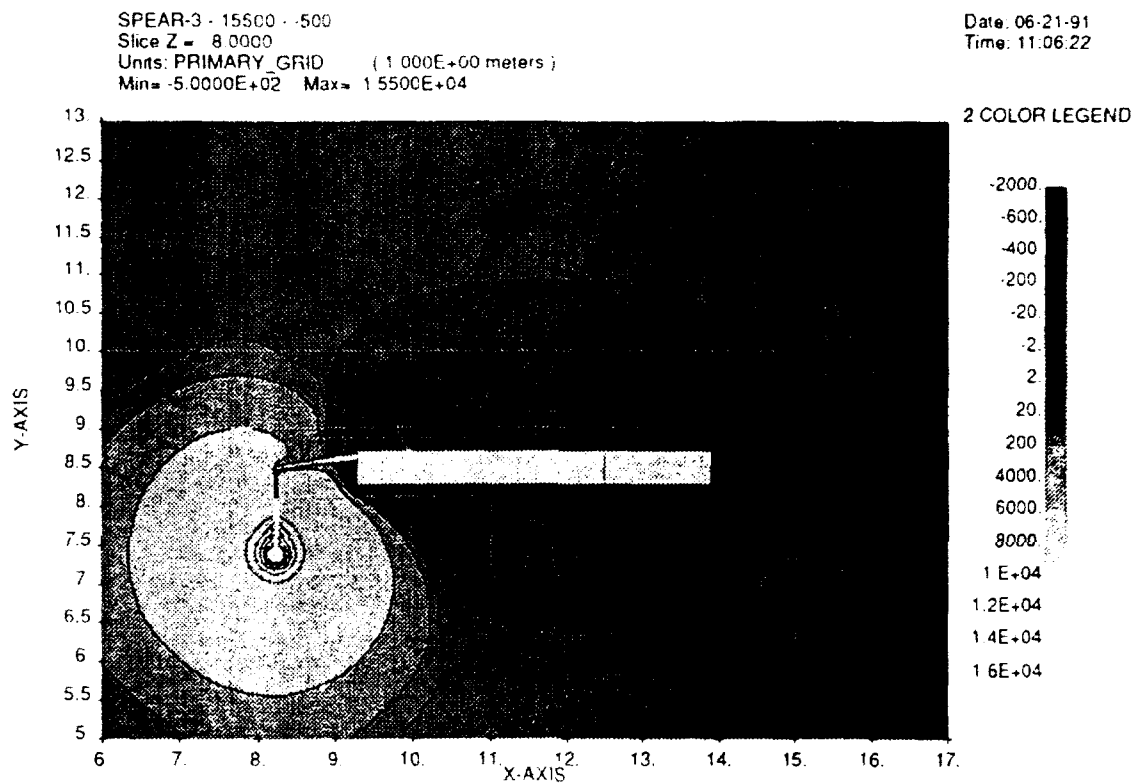


Figure 10.2(a) SPEAR III potentials for right-angle boom, 20 kilovolt bias, -500 volt rocket.

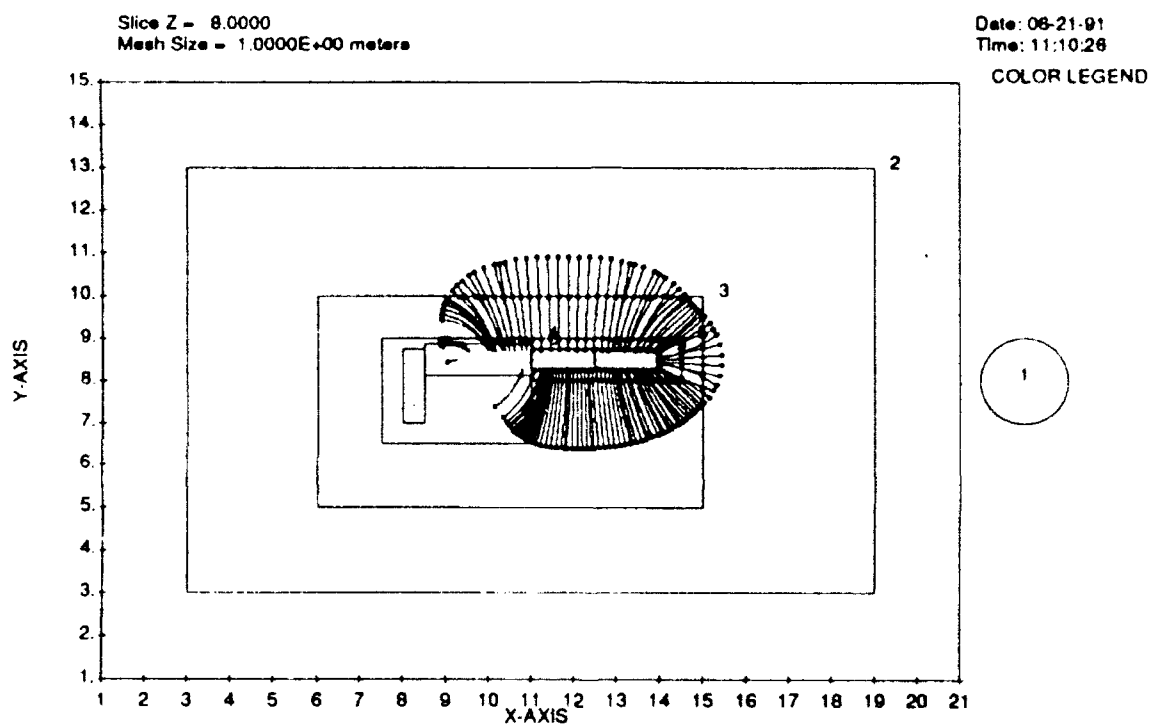


Figure 10.2(b) Ion trajectories in the potentials of figure 10.2(a).

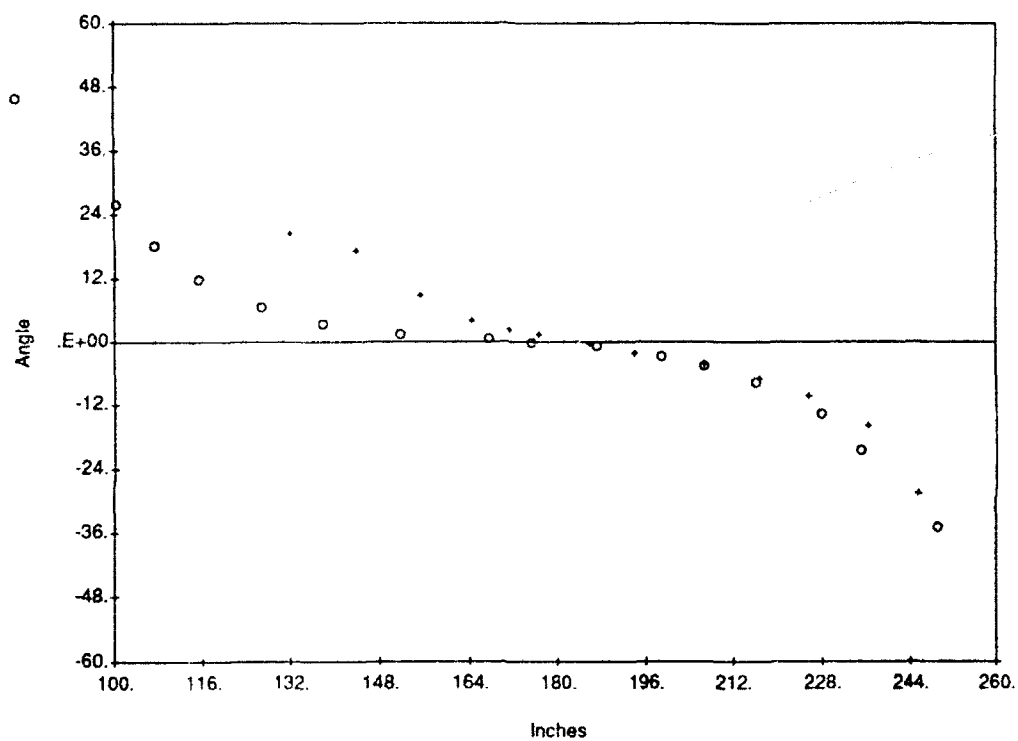


Figure 10.2(c) Incident angle for ions vs. detector position. Circles are for side opposite sphere, crosses for side toward sphere.

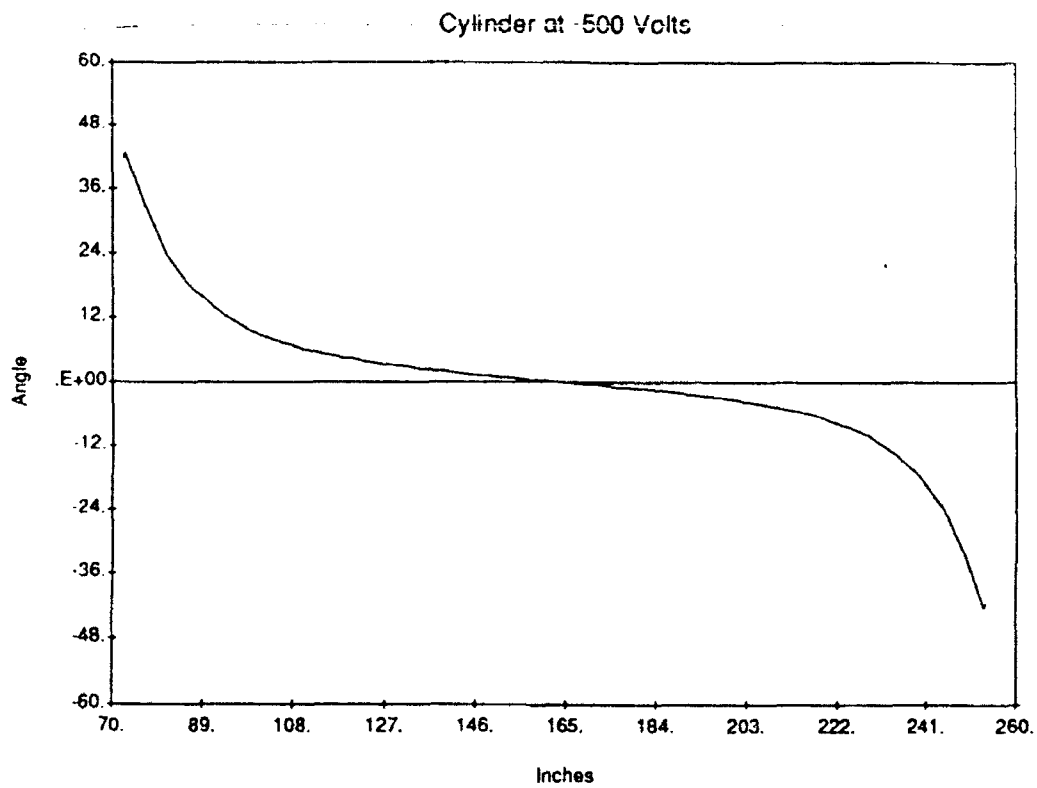


Figure 10.2(d) Gilbert results (for biased cylinder) corresponding to figure 10.2(c).

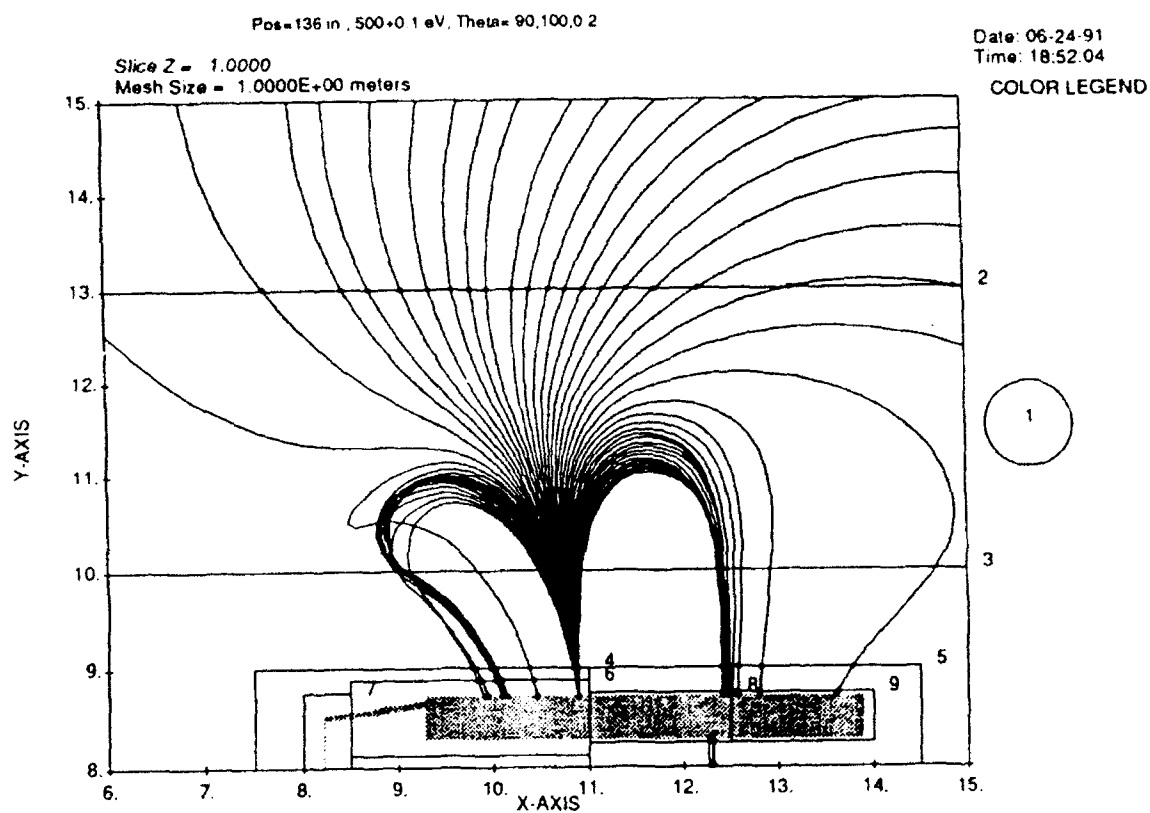


Figure 10.2(e) DynaPAC reverse trajectory calculation for ion detector near top of Science-1.

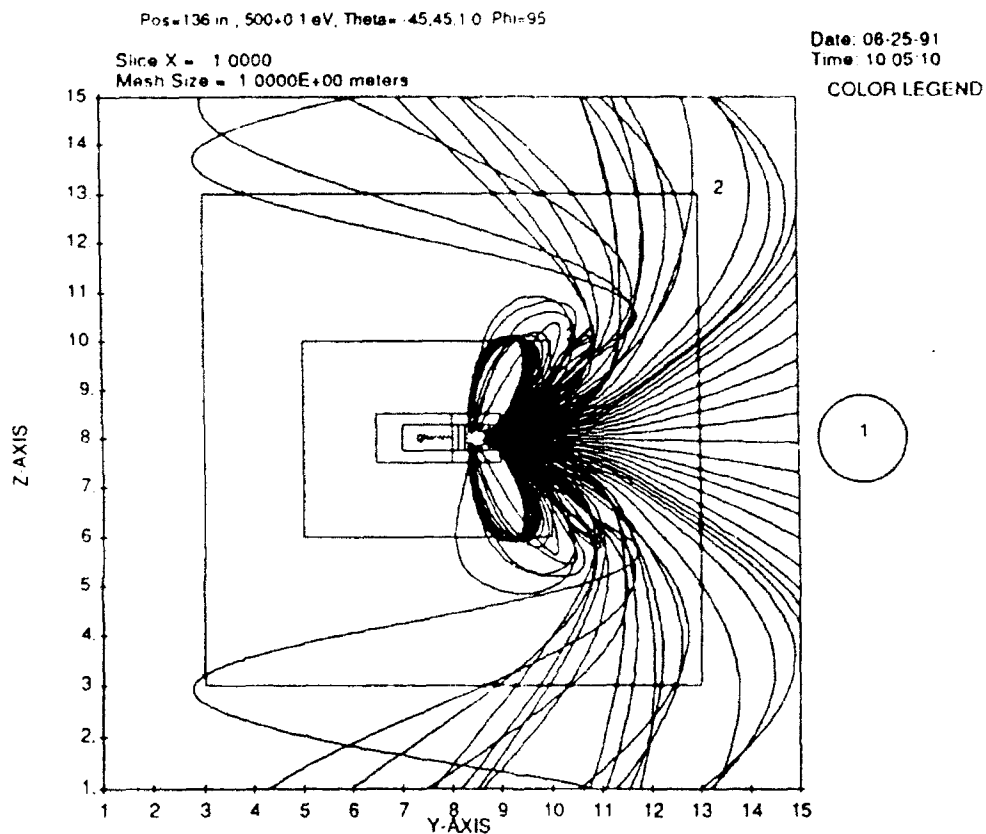


Figure 10.2(f) DynaPAC reverse trajectory calculation for azimuthal angle range corresponding to figure 10.2(e).

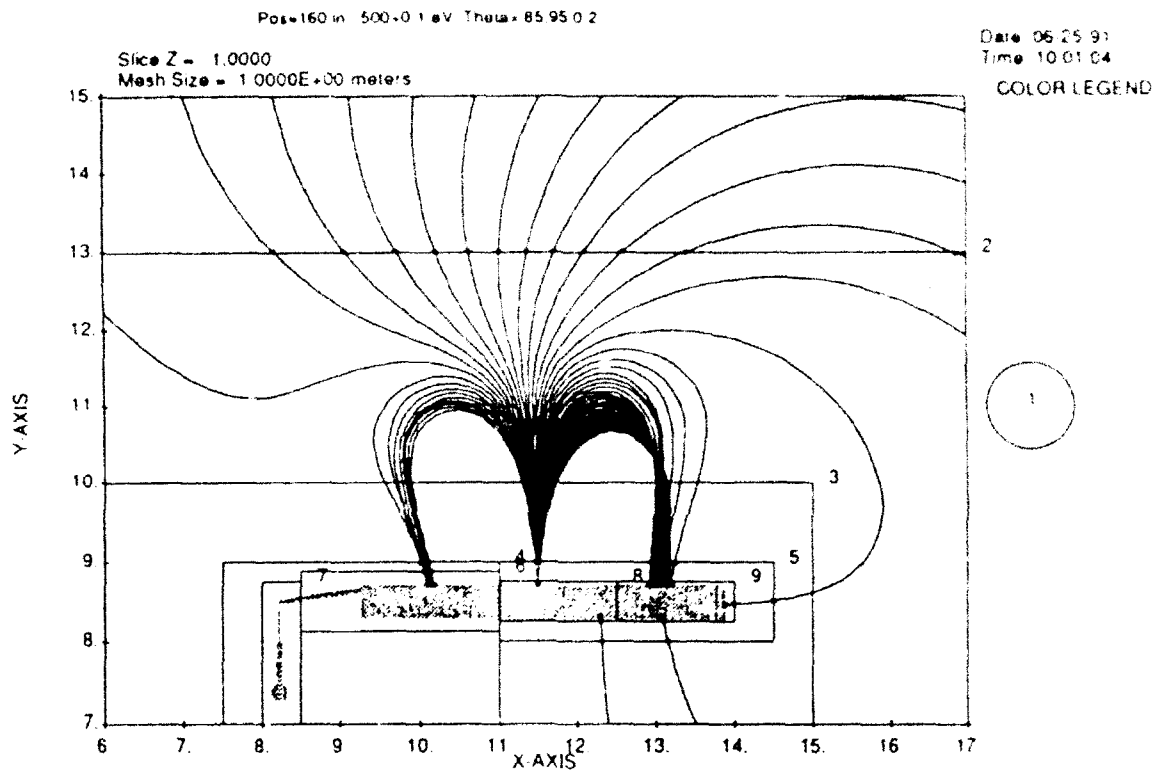


Figure 10.2(g) DynaPAC reverse trajectory calculation for ion detector near bottom of Science-1.

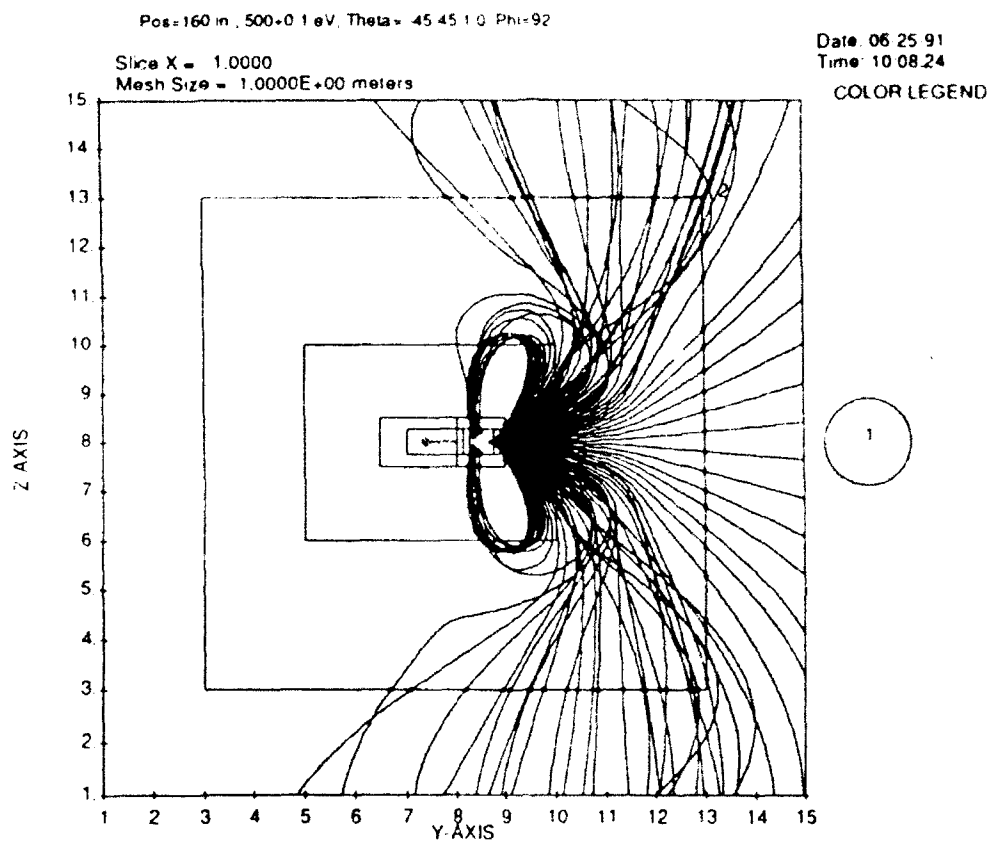


Figure 10.2(h) DynaPAC reverse trajectory calculation for azimuthal angle range corresponding to figure 10.2(g).

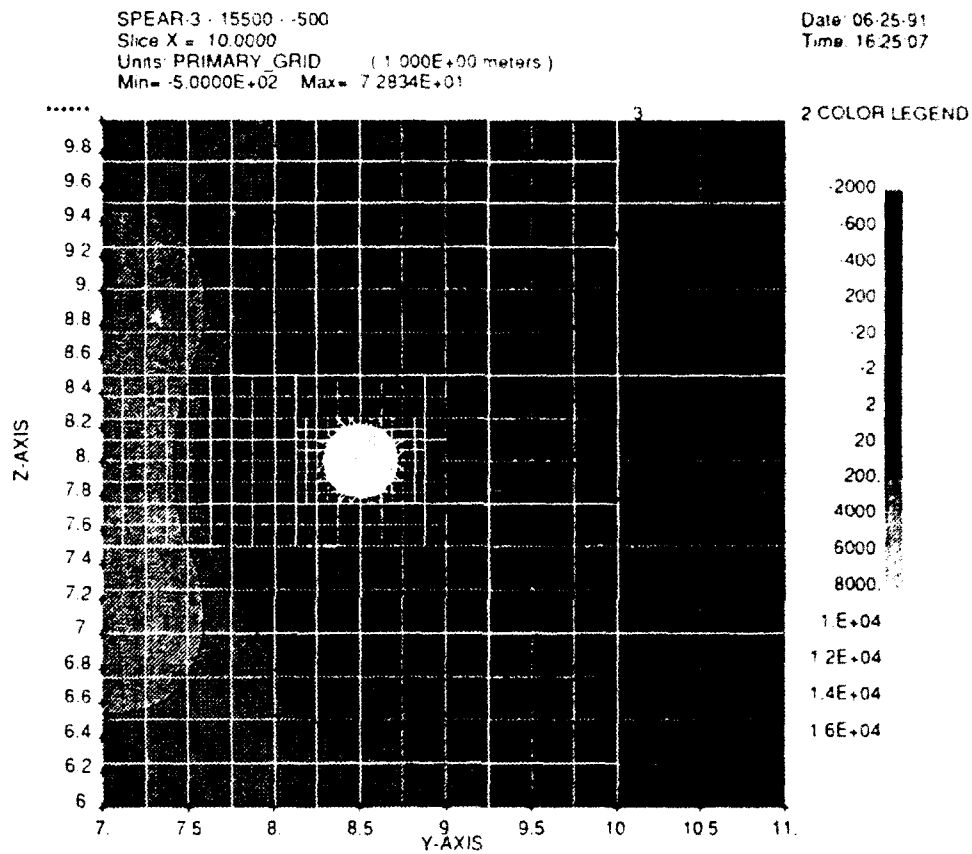


Figure 10.2(i) Potential contours in a cut normal to the rocket axis, showing non-concentric sheath which leads to a wide range of azimuthal angles.

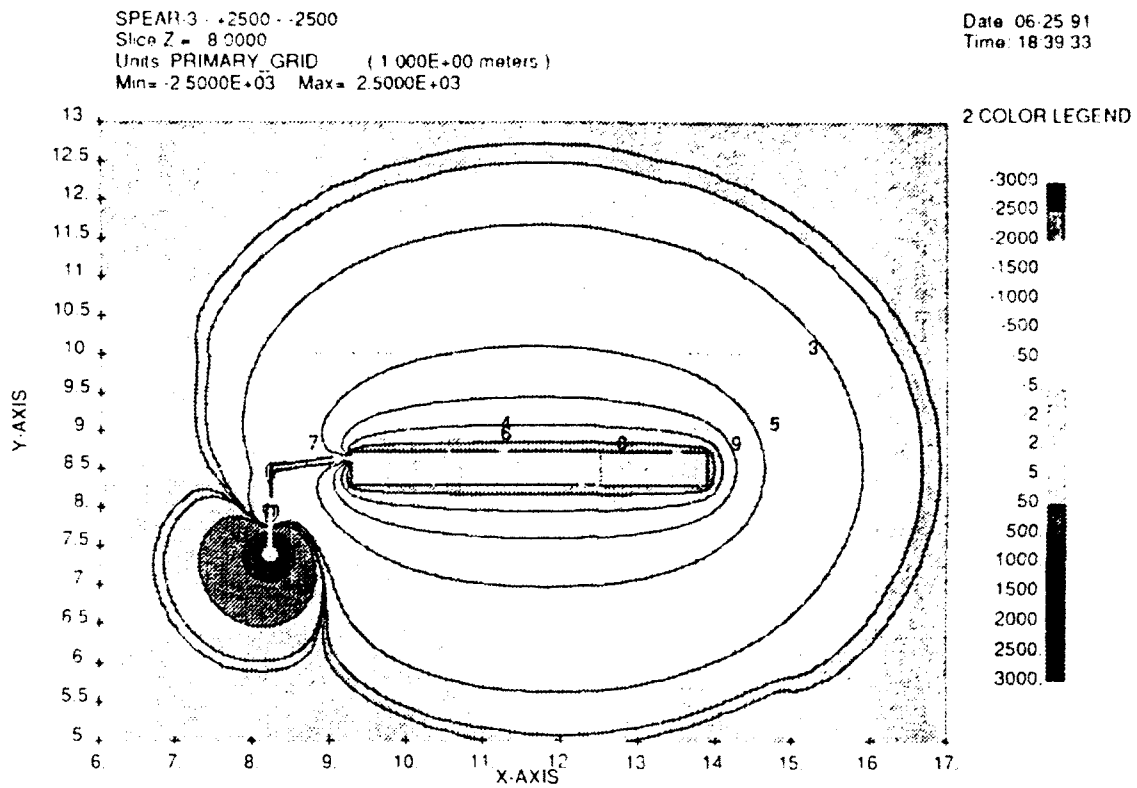


Figure 10.3(a) SPEAR III potentials for right-angle boom, 5 kilovolt bias, -2500 volt rocket.

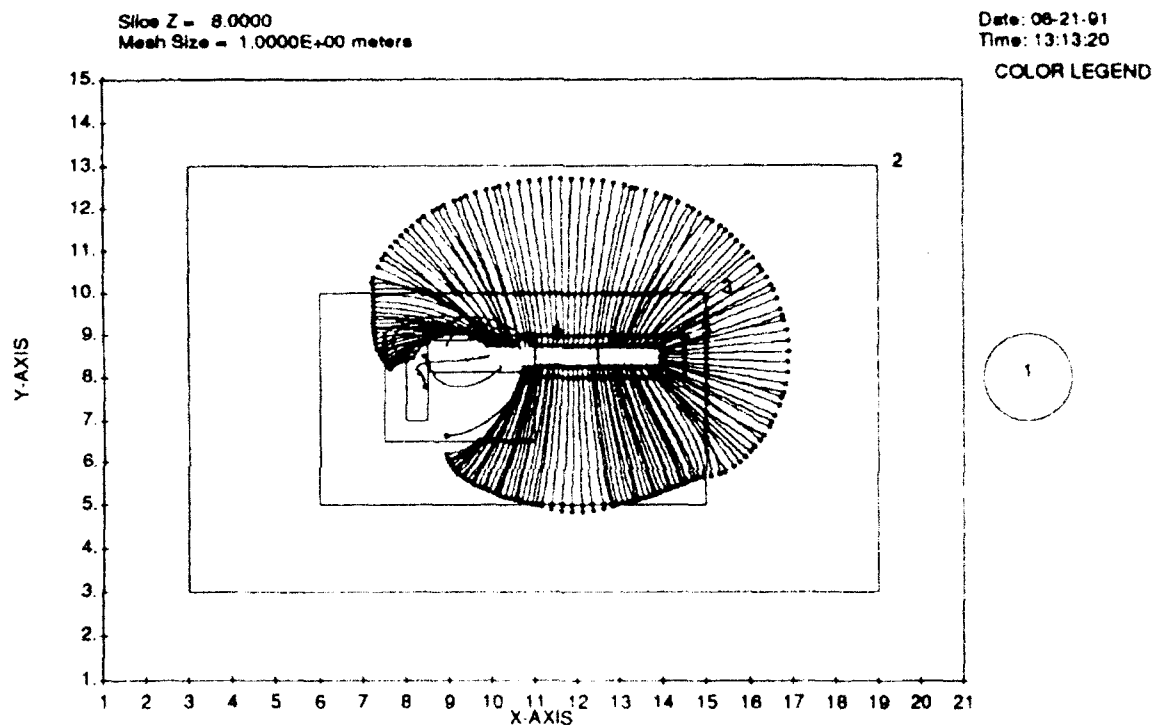


Figure 10.3(b) Ion trajectories in the potentials of figure 10.3(a).

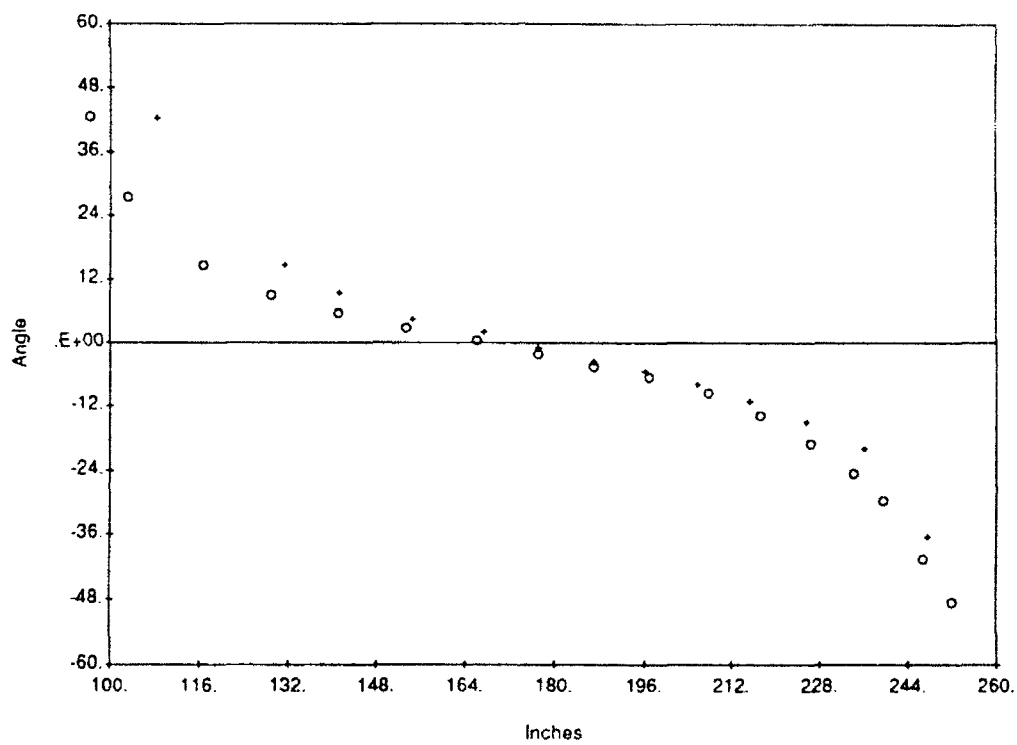


Figure 10.3(c) Incident angle for ions vs. detector position. Circles are for side opposite sphere, crosses for side toward sphere.

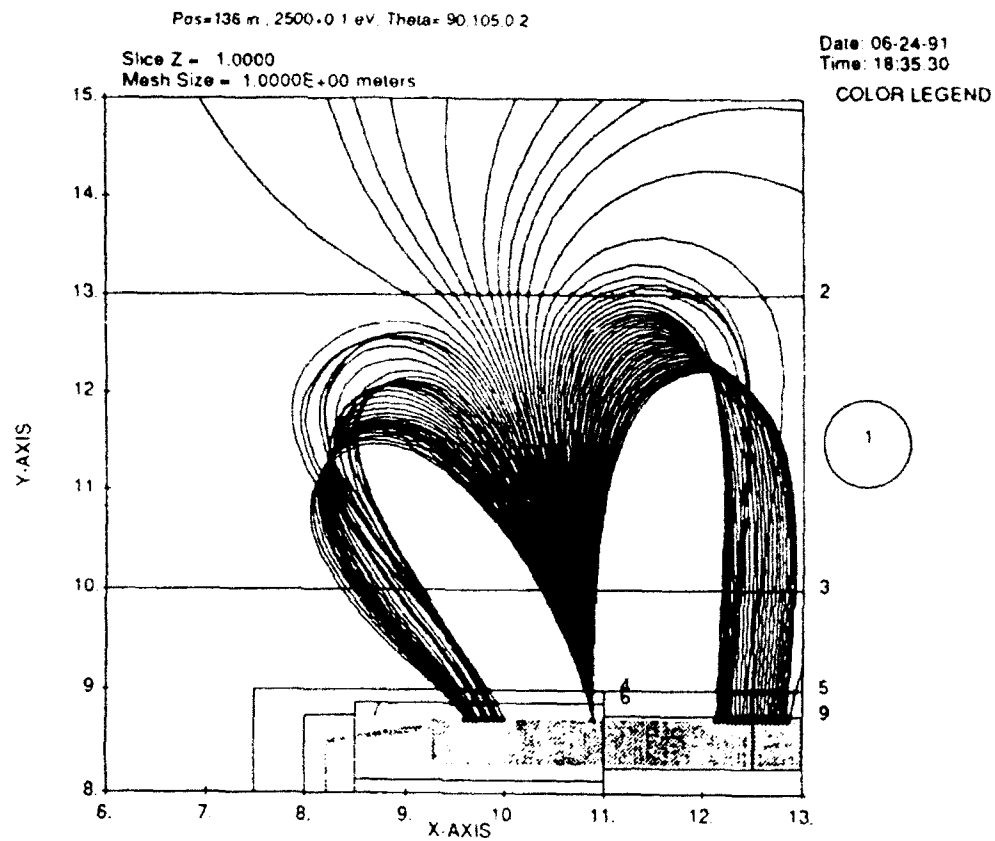


Figure 10.3(d) DynaPAC reverse trajectory calculation for ion detector near top of Science-1.

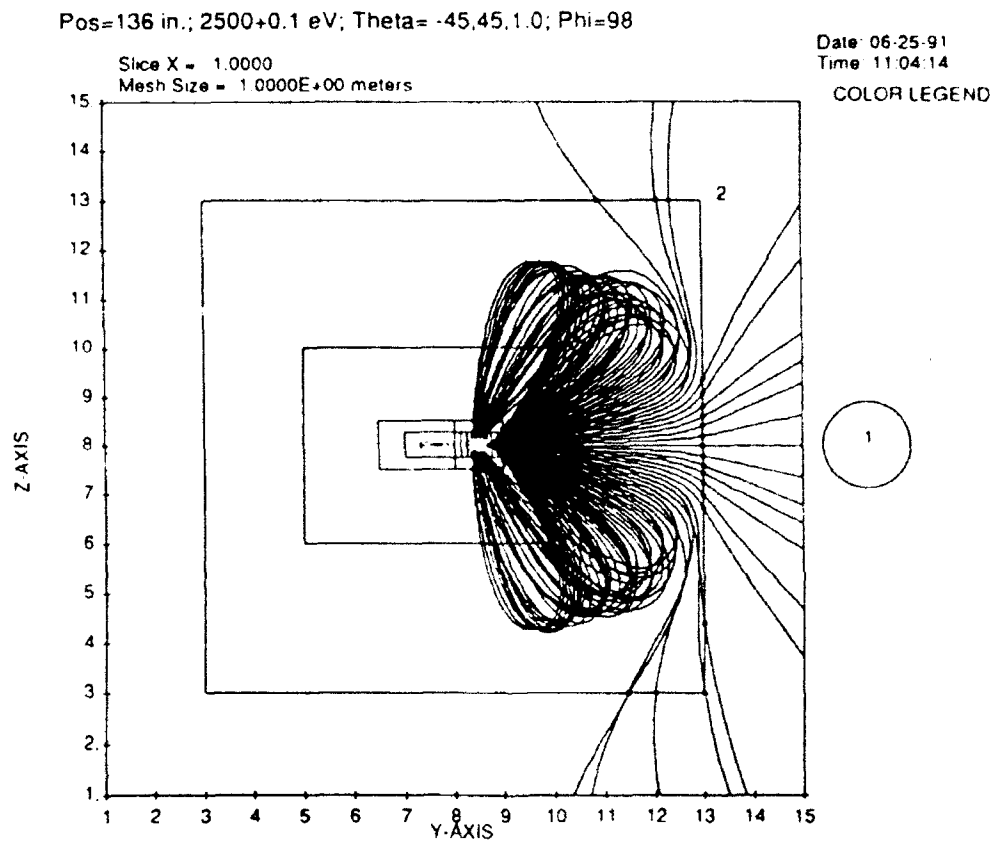


Figure 10.3(e) DynaPAC reverse trajectory calculation for azimuthal angle range corresponding to figure 10.3(d).

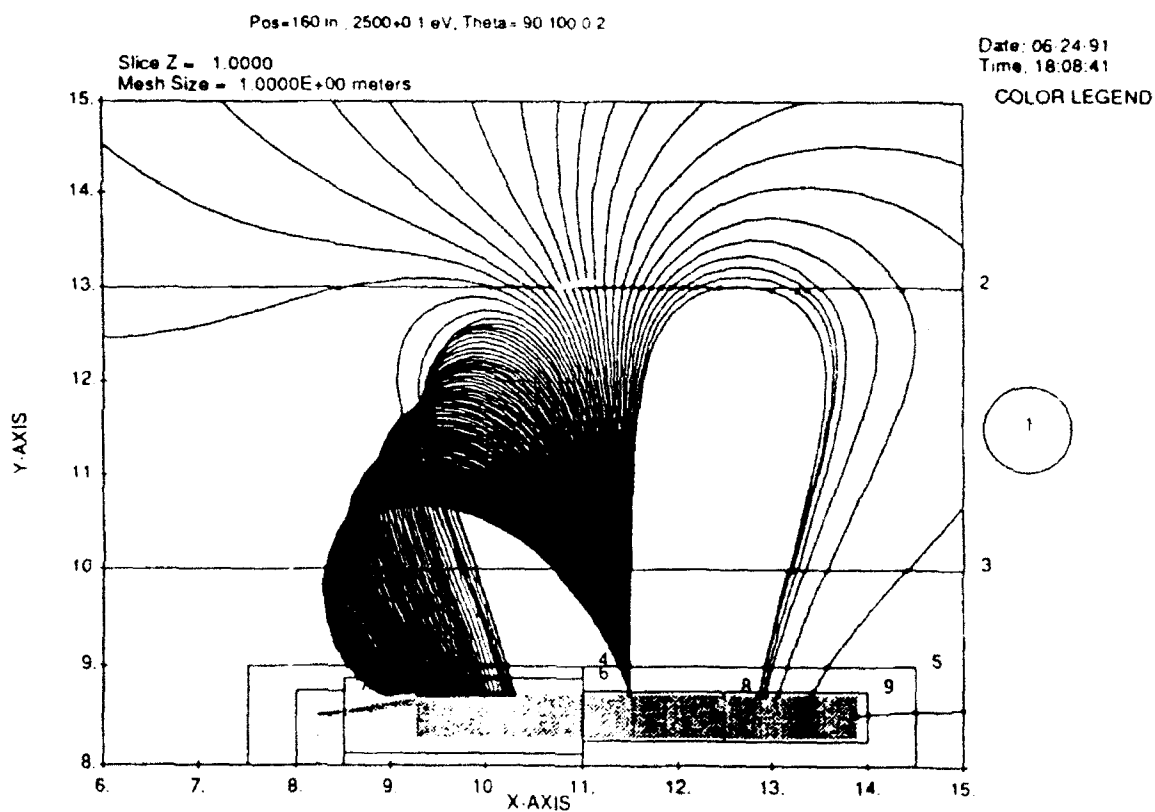


Figure 10.3(f) DynaPAC reverse trajectory calculation for ion detector near bottom of Science-1.

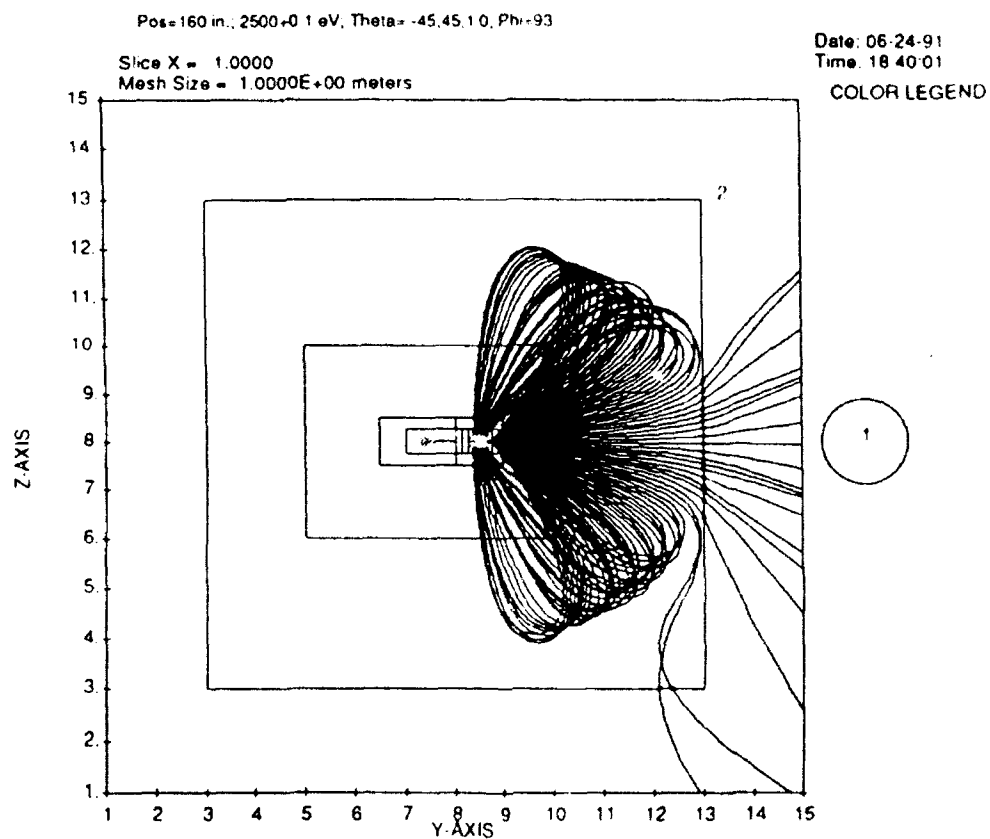


Figure 10.3(g) DynaPAC reverse trajectory calculation for azimuthal angle range corresponding to figure 10.2(f).

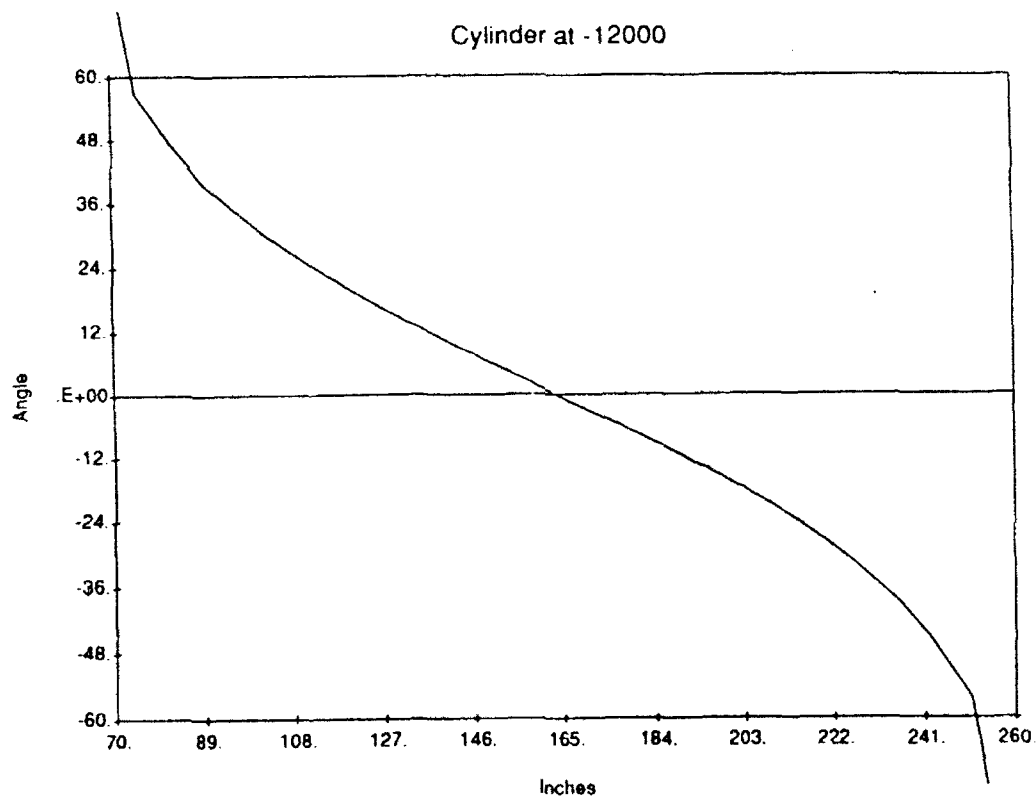


Figure 10.4 Gilbert calculation of incident ion angles for a cylinder at -12 kilovolts.

11. THREE-DIMENSIONAL MAGNETIC SHEATH CALCULATIONS

We used the DynaPAC computer code to perform 3-dimensional calculations of a 0.8 m radius, 1000 V sphere moving through a plasma with a magnetic field. The orbital motion was taken as 7500 m/sec in the x direction, and the magnetic field was 0.4 gauss in the y direction. The plasma density was 10^{12} m^{-3} , and the plasma temperature was 0.1 eV. The ion species was taken to be O^+ .

Figure 11.1 shows the wake of the uncharged object. The calculation uses a shadowing algorithm (originally developed for the POLAR code) to obtain the “neutral approximation” results, then applies an electric field correction.

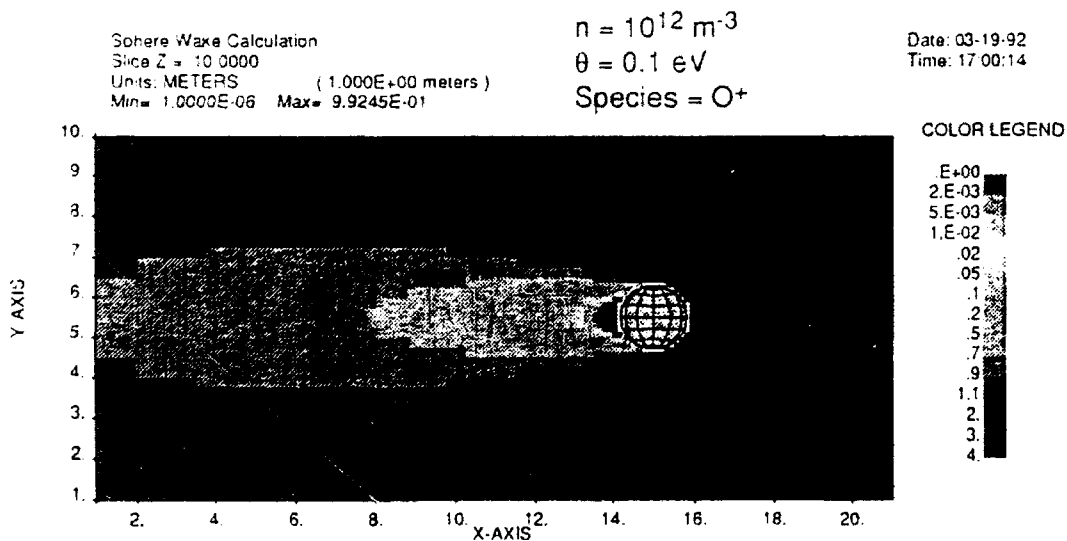


Figure 11.1 Plasma wake densities for an uncharged, 0.8 m radius sphere.

Figure 11.2 shows the electrostatic potential calculated using the object-wake ion densities. The calculation takes account of reduced screening due to low ion density in the wake as well as reduced wake-side electron currents. Thus, the high positive potential extends into the wake.

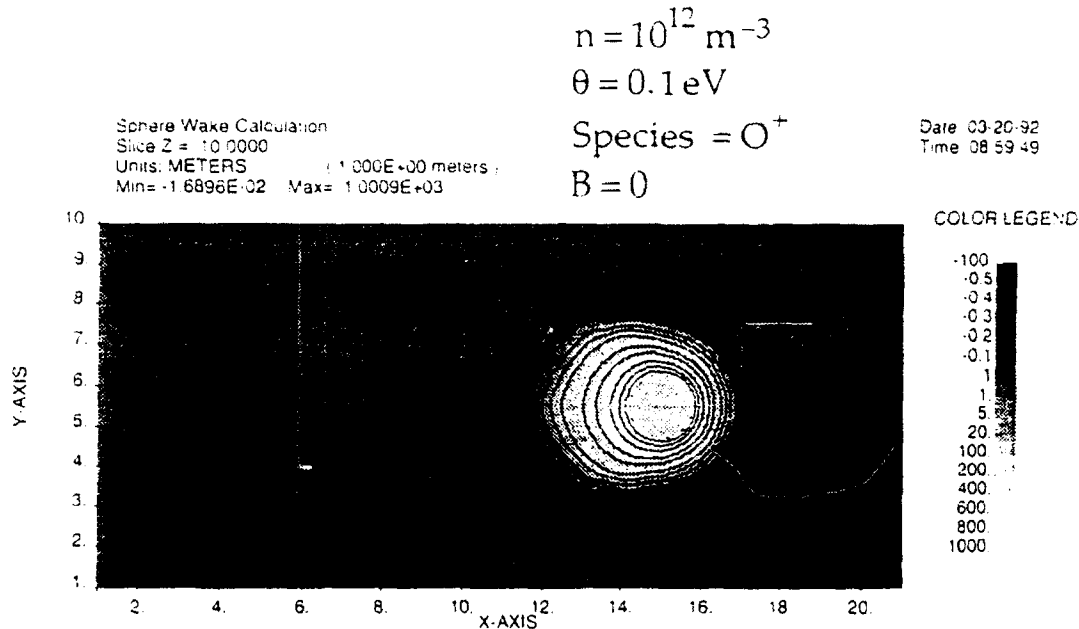


Figure 11.2 Electrostatic potentials calculated with the sphere at 1000 volts and the ion densities of Figure 11.1.

It is apparent from Figure 11.2 that the initial wake calculation is wrong. The wake of a positive object is formed not by the object surface, but by the much larger ion stagnation surface. The ion stagnation surface coincides with the 5 V contour level in the ram direction and drops to lower potential values on the sides of the sheath since the electric field is oblique to the ram velocity. Figure 11.3 shows wake ion densities calculated as in Figure 11.1 but now using the ion stagnation surface as the shadowing surface.

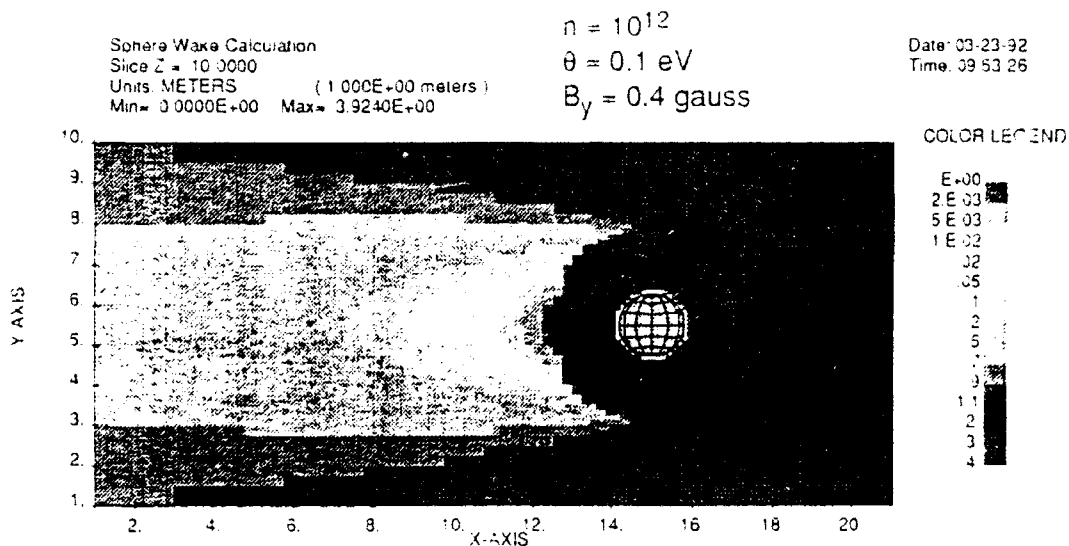


Figure 11.3 Ion densities calculated using the ion stagnation surface as a shadowing surface.

Figure 11.4 shows potentials calculated using the wake ion densities of Figure 11.3. Also, the calculation uses a new space-charge formulation that allows the wake region to be electron rich. We see the positive potentials extending further into the wake, and negative potentials down to about a half volt negative.

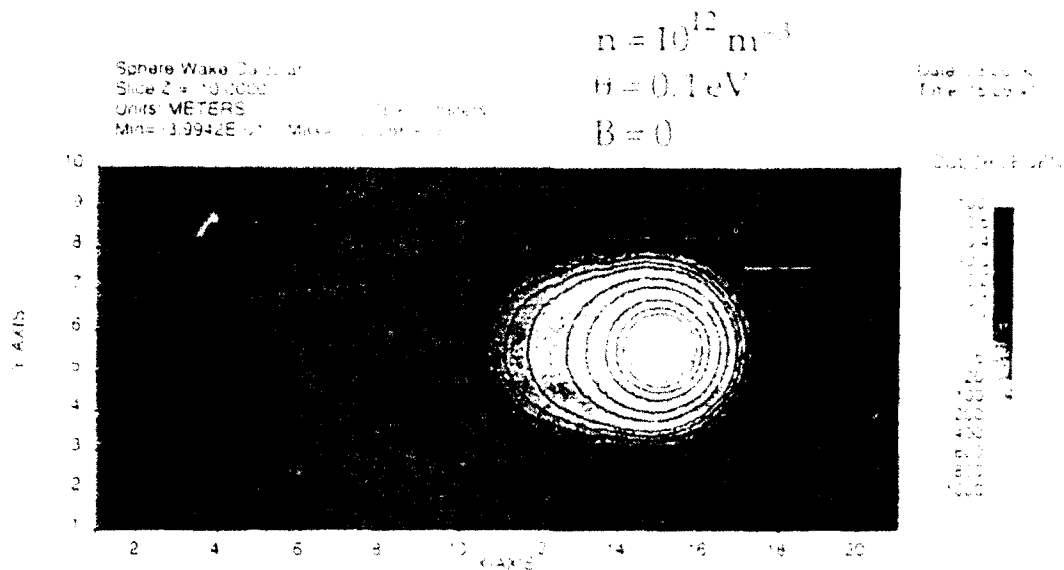


Figure 11.4 Electrostatic potentials calculated using ion densities similar to Figure 32, and a space charge formulation allowing the wake to be electron rich

Finally, we add a magnetic field along the Y axis. To determine self-consistent potentials in a magnetic field requires generating electrons at a "sheath surface" and tracking them to determine self-consistent electron densities within the sheath. Figures 11.5(abc) show the resultant electron densities, and Figures 11.6(abc) show the potentials. The three electron density plots show low electron densities near the $\pm Y$ sides of the sphere but relatively higher densities in the other directions. This indicates that a belt of electrons is now orbiting the sphere in the X-Z plane. This belt of electrons has little effect on the ram side (where its charge is neutralized by the ions), but on the wake side (where there were previously no ions or electrons) it squeezes the sheath boundary close to the object, as is seen by comparing Figures 11.6(abc) with Figure 11.4. It also reduces the Z sheath dimension relative to the Y sheath dimension, although for these parameters the asymmetry only becomes apparent wakeward of the sphere. (Rough calculations for other parameters show far more apparent asymmetry.)

Sphere Electron Charge
 Slice Z = 10.0000
 Units: METERS (1.000E+00 meters)
 Min= -3.2418E+03 Max= 0.0000E+00

Date: 03-24-92
 Time: 14:11:50

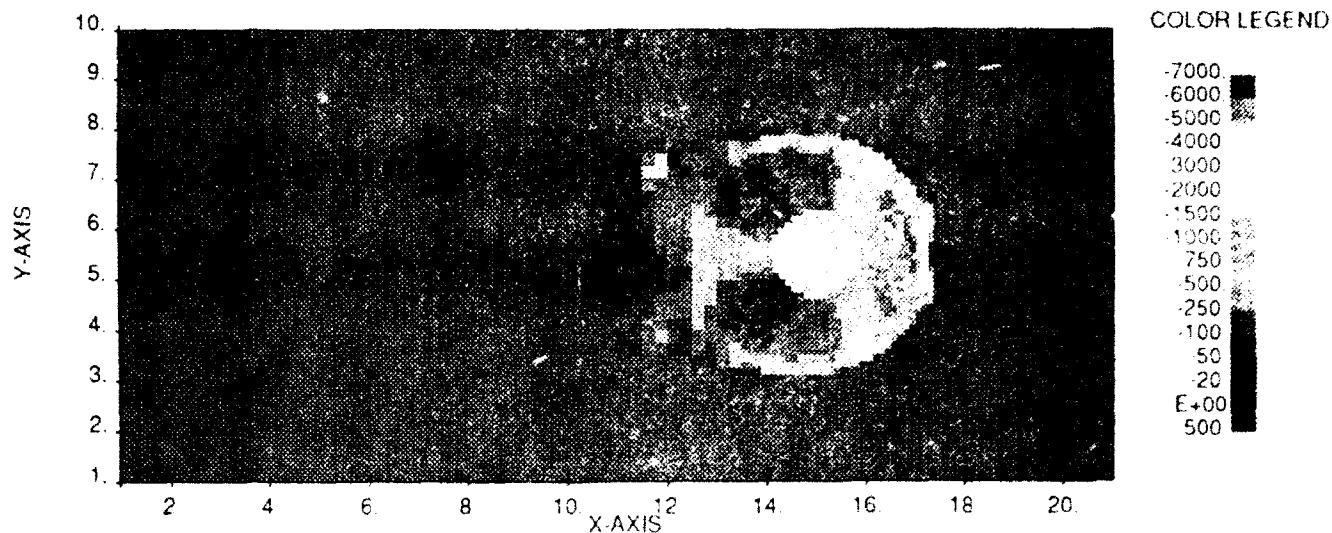


Figure 11.5(a) Tracked electron densities in the sheath region, with a magnetic field of 0.4 gauss in the y direction: (a) X-Y plane.

Sphere Electron Charge
 Slice Y = 10.0000
 Units: METERS (1.000E+00 meters)
 Min= -3.7300E+03 Max= 0.0000E+00

Date: 03-24-92
 Time: 14:12:15

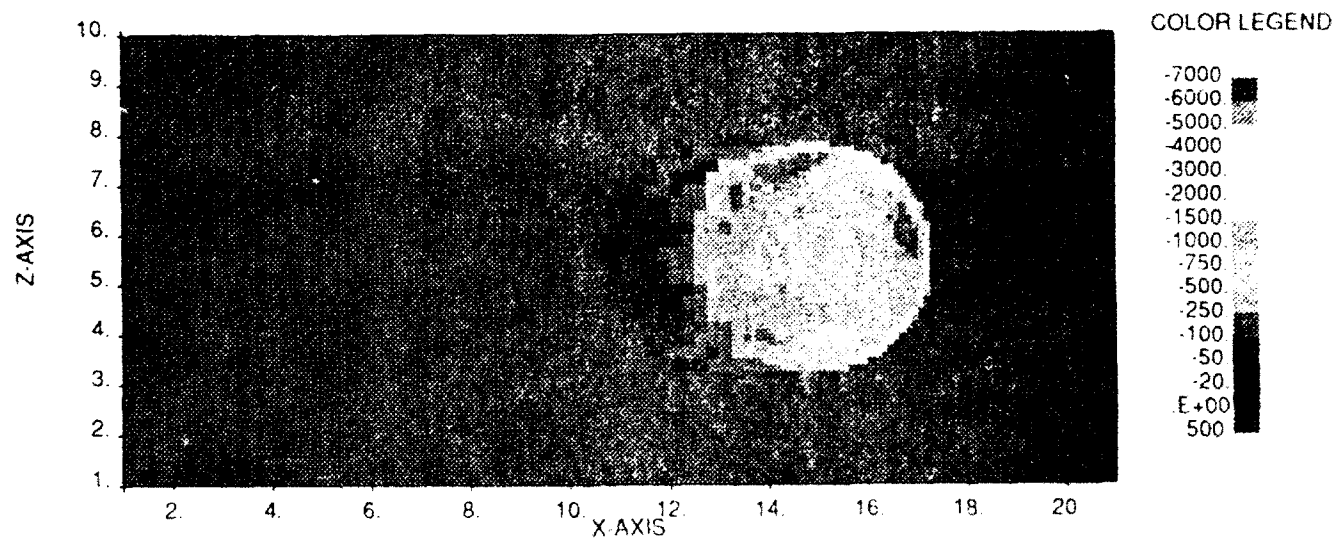


Figure 11.5(b) Tracked electron densities in the sheath region, with a magnetic field of 0.4 gauss in the y direction: (b) X-Z plane.

Sphere Electron Charge
Slice X = 29.0000
Units: METERS
Min = -1.7876E+05 Max = 3.0000E+00

Date: 03-24-92
Time: 14:12:42

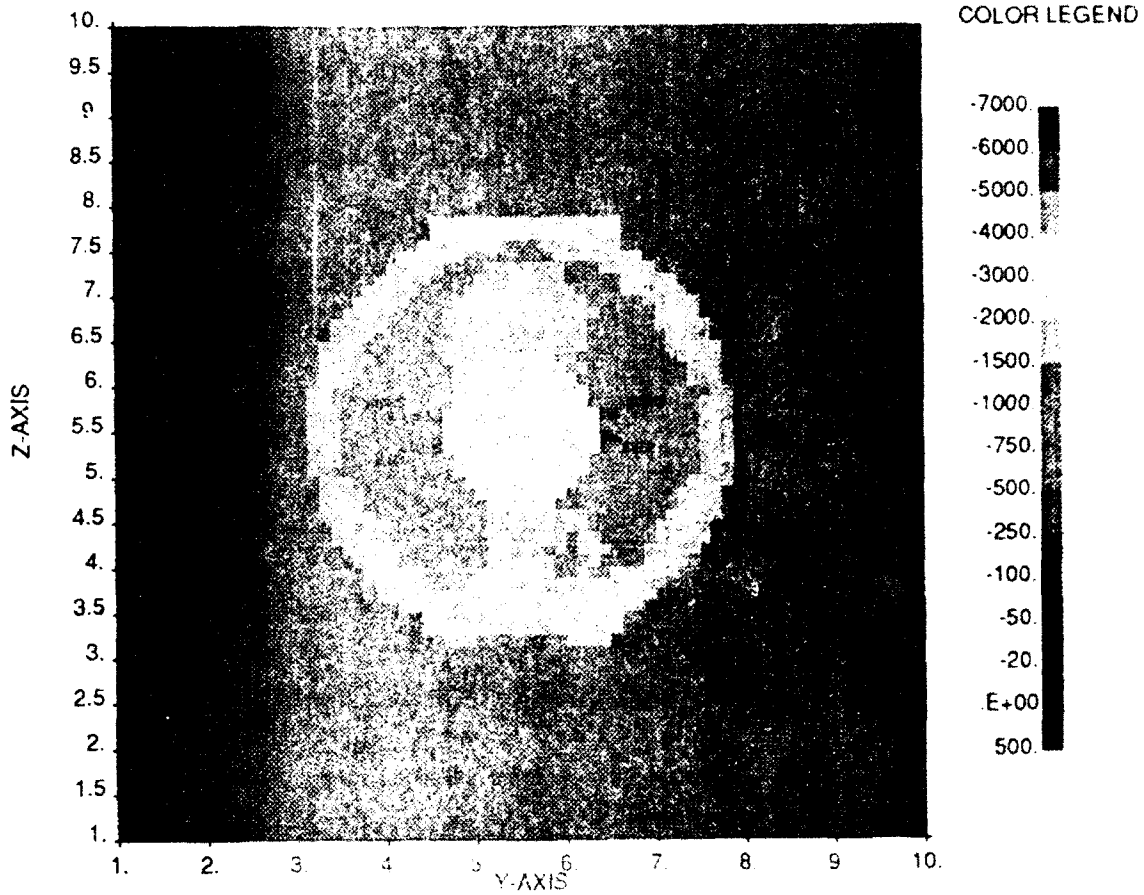


Figure 11.5(c) Tracked electron densities in the sheath region, with a magnetic field of 0.4 gauss in the y direction: (c) Y-Z plane.

Sphere Wake Calculation
 Slice Z = 10.0000
 Units: METERS (1.000E+00 meters)
 Min= -6.0849E-01 Max= 1.0007E+03

Date: 03-24-92
 Time 16:56:39

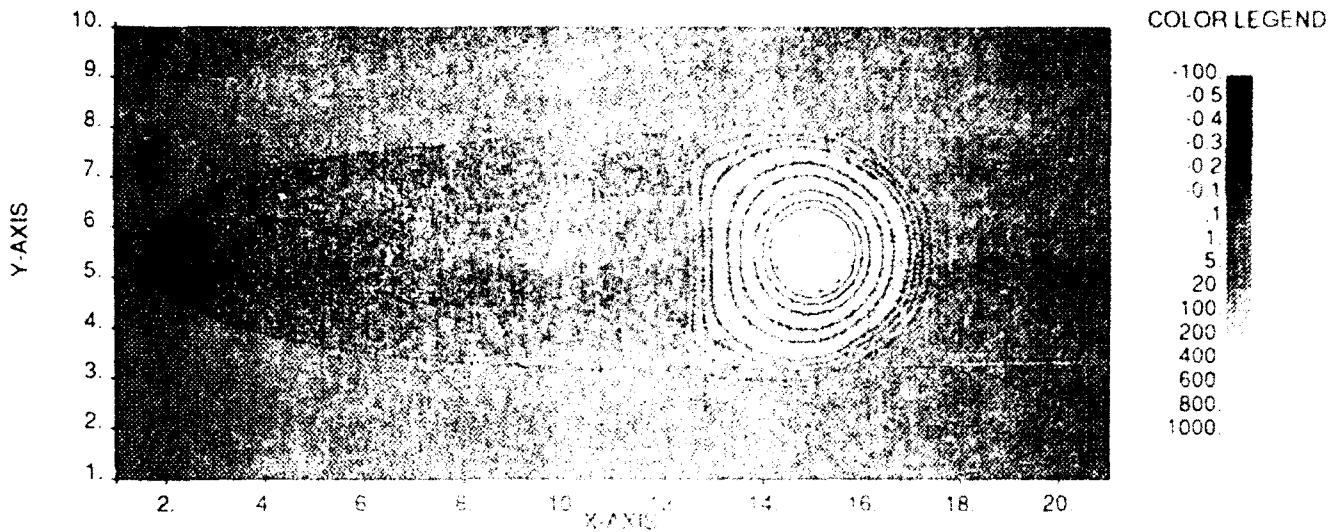


Figure 11.6(a) Electrostatic potentials calculated using the tracked electron densities in the sheath region: (a) X-Y plane

Sphere Wake Calculation
 Slice Y = 10.0000
 Units: METERS (1.000E+00 meters)
 Min= -6.0849E-01 Max= 1.0000E+03

Date: 03-24-92
 Time: 16:57:51

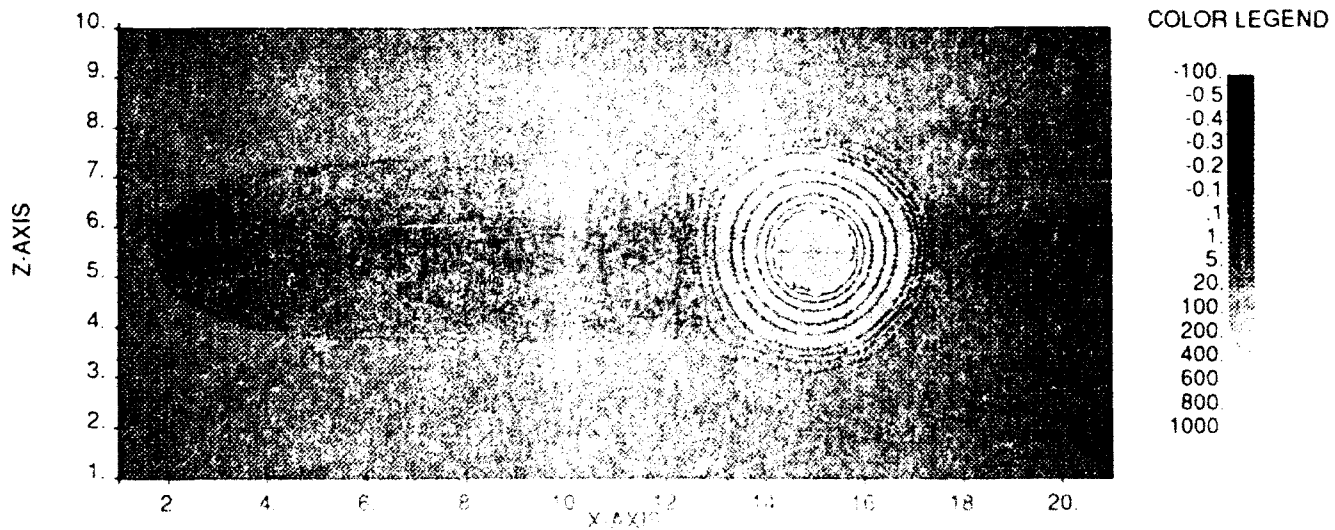


Figure 11.6(b) Electrostatic potentials calculated using the tracked electron densities in the sheath region: (b) X-Z plane

Sphere Wake Calculation
Slice X = 29.0000
Units: METERS
Min = -8.4814E-03 Max = 1.0801E+03

Date: 03-24-92
Time: 16:58:24

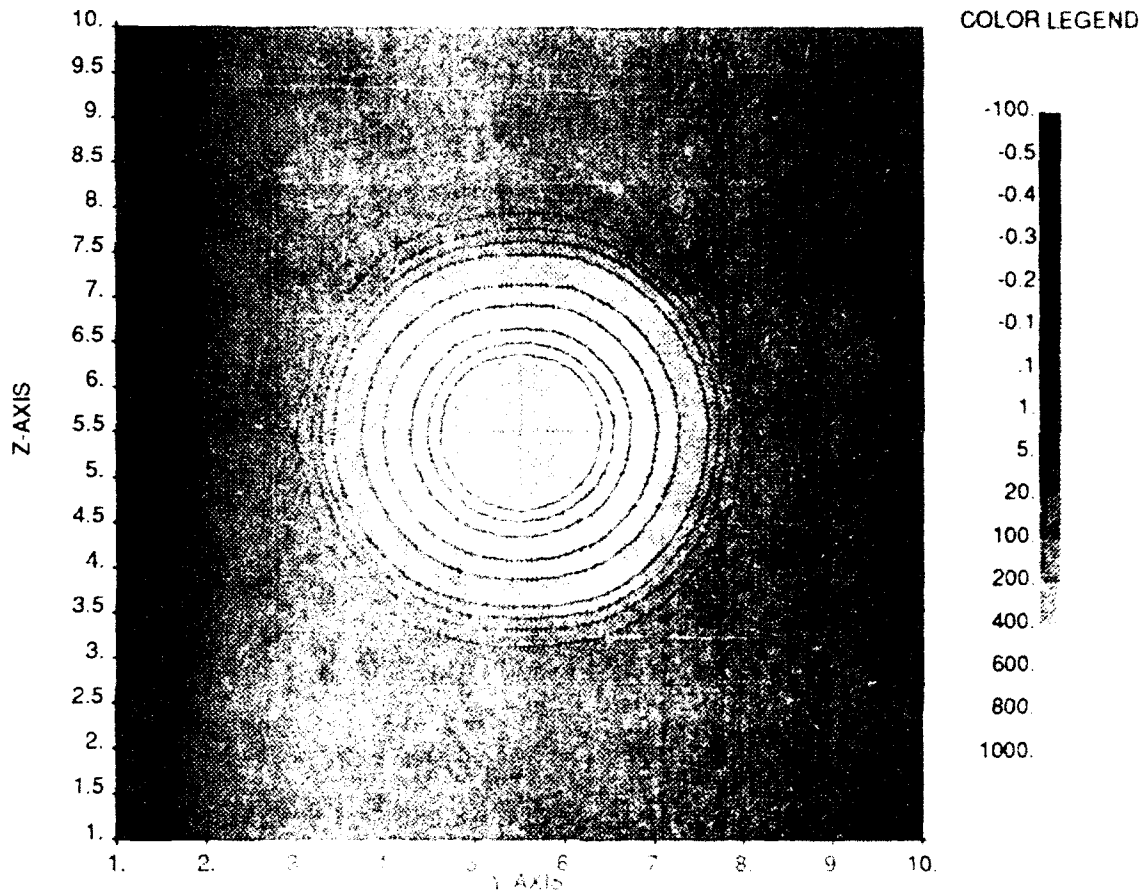


Figure 11.6(c) Electrostatic potentials calculated using the tracked electron densities in the sheath region: (c) Y-Z plane.